The Role of Surface-Energy of Carbon-based Nano-Particles in Polymer-Filler Interaction and Reinforcement of Elastomer Nano-Composites

Von der Naturwissenschaftlichen Fakultät der
Gottfried Wilhelm Leibniz Universität Hannover

zur Erlangung des akademischen Grades
Doktor der Naturwissenschaften (Dr. rer. nat.)

genehmigte Dissertation
von
Frank Fleck, Dipl.-Phys.

2021

Referent:	Hon.-Prof. Dr. rer. nat. habil. Manfred Klüppel
Korreferent:	Prof. Dr. rer. nat. Jörg August Becker
Tag der Promotion:	08.10.2021

1. Abstract

In this work, the role of carbon black (CB) as reinforcing material for elastomer composites was studied on various length-scales. The technique of static, volumetric gas adsorption was utilized to elucidate the energetic- and morphological characteristics of the surface of CB on the smallest length-scale. Therefore, the surface of CB was modified with the ionic liquid 1-allyl-3-methyl-imidazolium chloride (AMIC). A clear drop in energetic heterogeneity, i.e. a reduced number of highly active sites on the surface of the modified CB was found.
For the purpose of a holistic multi-scale approach, rheological measurements simultaneously measuring the mechanical- as well as the dielectric response of the sample, have been conducted. A strong focus was shedding light on the nature of the polymer-filler interaction. Thus, the build-up process- as well as the break-down of a filler network structure was analysed. The first was achieved via isothermal flocculation experiments at small dynamic strains, which showed an interrelation between the mechanical stiffness and the electric conductivity. Similarly the observed drop in mechanical stiffness (Payne-Effect) if rubber is exposed to increasing strain amplitudes is also found in the electric conductivity. This naturally proves, that the break-down of the filler network can explain the Pane-effect in filled elastomer. Moreover, by using different polymer types with varying polarity and double-bond saturation level, evidence of an interphase affected by the characteristics of the CB-interface as well as the polymer-chain was found.
Furthermore, a structurally modified CB was used to analyse the influence of the CB-aggregate structure on a small- to medium length-scales. These samples were analysed using a transmission-electron-microscope (TEM). The relation between the structural findings from the TEM image analysis to the mechanical stress-strain characteristics of a multi-hysteresis test was obtained by utilizing the dynamic flocculation model (DFM). It could be concluded, that the mixing process might have a strong influence on highly structured CB-types by decreasing its structure due to high shear forces when a certain critical filler level is exceeded. This finding is contradicting the generally accepted picture of primary aggregates as the smallest, non-breakable unit inside (CB) filled elastomer-composites.

Keywords: *Rubber, Polymer-filler-interaction, Filled elastomers, Reinforcement,Gas adsorption, Rheology*

2. Kurzfassung

In dieser Arbeit wurde die Rolle von Ruß als Füllstoff in Elastomer-Kompositen auf verschiedenen Längen-Skalen untersucht. Die Methode der statischen, volumetrischen Gasadsorption wurde dabei verwendet um die Oberfläche des Rußes auf ihre energetische- und morphologische Beschaffenheit hin - auf der kleinsten Skala - zu untersuchen. Zu diesem Zweck wurde die Oberfläche des Rußes mittels der ionischen Flüssigkeit 1-Allyl-3-Methyl-Imidazol Chlorid (AMIC) modifiziert. Es wurde ein signifikanter Abfall der energetischen Heterogenität - also der Anzahl an hochenergetischen Plätzen auf der modifizierten Ruß-Oberfläche festgestellt.
Mit dem Ziel einer kompletten Betrachtung auf verschiedene Skalen, wurden rheologische Experimente durchgeführt bei denen gleichzeitig die mechanischen- als auch die dielektrischen Eigenschaften des Materials aufgezeichnet wurden. Der Fokus lag dabei auf einem besseren Verständnis der Polymer-Füllstoff Wechselwirkung. Daher wurde sowohl der Aufbau- als auch der Zusammenbruch des Füllstoff-Netzwerkes genauer betrachtet. Der Aufbau des Netzwerks wurde über isotherme Flokkulations-Messungen bei kleinen Dehnungen beobachtet, welche einen Zusammenhang zwischen der mechanischen Steifigkeit und der elektrischen Leitfähigkeit lieferte. Beim Einbruch der mechanischen Steifigkeit durch sukzessive Erhöhung der dynamischen Amplitude (Payne-Effekt) zeigte auch die elektrische Leitfähigkeit einen ähnlich abnehmenden Verlauf. Dies zeigt auf natürliche Weise, dass der Payne-Effekt in jedem Fall über strukturelle Änderungen im Füllstoff-Netzwerk zu erklären ist. Durch den Einsatz verschiedener Polymer Typen mit variierender Polarität und Anzahl der Doppelbindungen konnten Hinweise auf die Existenz einer charakteristischen Grenzschicht zwischen Polymer und Füllstoff erhärtet werden.
Weiterhin wurde ein Ruß mit erhöhter Struktur untersucht um auf etwas größerer Skala den Einfluss der Primär-Aggregate zu untersuchen. Zu diesem Zweck wurden die Proben mittels Transmissionselektronenmikroskop (TEM) analysiert. Ein Zusammenhang zwischen den strukturellen Besonderheiten, die mit Hilfe der TEM-Bilder gewonnen wurden und den mechanischen Eigenschaften in einem Mutihysterese-Zugversuch, konnte mit dem dynamischen Flokkulations Modell (DFM) gefunden werden. Eine Schlussfolgerung aus diesen Untersuchungen ist die Abnahme der Struktur von Primär-Aggregaten bei hoch-strukturierten Rußen auf Grund von erhöhten Scherkräften beim Mischen im Falle von sehr hohen Füllgraden. Diese Beobachtung widerspricht der allgemeinen Annahme, dass Primär-Aggregate die kleinsten, nicht-aufbrechbaren Strukturen von Ruß gefüllten Elastomer-Mischungen sind.

Stichwörter: *Polymere, Polymer-Füllstoff-Wechselwirkung, gefüllte Elastomere, Verstärkung, Gas Adsorbtion, Rheologie*

3. Acknowledgement

Firstly, I would like to express my gratitude to my supervisor at the DIK Prof. Dr. rer. nat. habil. Manfred Klüppel. His scientific creativity and the ability to share his deep knowledge made me learn to love polymer physics. Secondly, a special thanks to Prof. Dr. rer. nat. Jörg August Becker who volunteered to be my co-supervisor. Furthermore, I would like to thank Prof. Dr. rer. nat. Ulrich Giese, who accompanied me the whole way during my time at the DIK as head of the institute as well as beyond via various cooperations.

I am especially grateful for all the helping hands in the DIK, who taught me everything I know about rubber: From mixing, over vulcanizing to the experiments to understand its properties. Here, I particularly would like to mention Joachim Heier and Jürgen Hamann, whose valuable experience made it easier to learn the art of rubber. Moreover, I want to thank all of my fellow PhD-students in DIK, who made the experience of learning scientific work such a joy and special time.

Last but not least I have to thank my family in particular my parents, who supported me all the way and made everything I am today possible in the first place. Also my loved girlfriend Ina deserves special thanks, since she was always patient with my lack of speed finishing this work but at the same time constantly keeping some pressure alive to ensure some - albeit slow - progress.

Contents

1. Introduction

In today's technological- and scientific environment, one of the most important class of materials are polymers. Those, showing a very high degree of elasticity and flexibility, are often referred to as elastomers or sometimes just rubber. However, the term rubber is usually used when referring to cross-linked elastomers, i.e. polymers, which are linked via permanent chemical bonds.[1] Generally, elastomers are characterized by weak intermolecular forces, a low Young's modulus and a high stretchability, i.e. a large strain at break.[2]
Every elastomer shows a characteristic time dependency, which was empirically described by Wiliams, Landel and Ferry. They could show, that a time dependency is equivalent to a characteristic temperature dependency, which is often referred to as time-temperature superposition principle.[3] At short time-scales or at low temperatures, elastomers show a glass transition, i.e. a gradual and reversible change from hard and brittle ("glassy") into a rubbery elastic state. This time-scale or temperature is essentially determined by the chemical details of the monomers. Typical types of polymers are for example natural rubber (NR), which is chemically identical to cis-1,4-poly-isoprene (IR), styrene butadiene rubber (SBR), ethylene propylene diene rubber (EPDM) or nitrile butadiene rubber (NBR) (see figure 1.1 for some examples with their respective typical ranges of glass transition temperatures[1] or [4, 5] for more details).
On larger time-scales and at higher temperatures, certain polymer-characteristics on a bigger length-scale than the monomer become important. Since polymers consist of long chains, they are entangled to each other and thus form a physical network due to the resulting topological constraints.[6, 7] During the past 50 years, various theoretical descriptions of entangled polymer melts have been developed. Based on these findings, a single polymer chain is confined inside a tube-like structure, which is formed due to the presence of adjacent polymer chains, which hinder the chain to move freely in all directions, i.e. can hence only reptate within the tube. The diameter of the tube is therefore proportional to the entanglement density of the polymer. [8–22] This temperature range (and respectively the characteristic times) is often referred to as the rubber elastic plateau, which defines the corresponding experimentally determined[2] plateau modulus G_N.[3] For time-scales (and temperatures) beyond this entanglement dominated regime, i.e. where chains have enough time to reptate out of their respective tubes, every elastomer shows viscous flow behaviour.[25] Thus, a typical elastomer is in essence characterized by two main states: (i) The glass transition – separating the glassy- from the rubbery state; and (ii) the rubber elastic plateau – defined by the entanglement density and molecular weight of the

[1] Depending on the corresponding ratio of respective blocks inside the monomer - e.g. the styrene content in SBR or the nitrile content in NBR (see the indices x, y and z in figure 1.1).
[2] Usually via rheological experiments of oscillatory shear deformations at varying temperature and frequency.
[3] The stiffness of the material, which is coupled to the entanglement modulus G_e with a semi-empirical prefactor of $4/5$: $G_N = 4/5 G_e$ according to Doi-Edwards theory.[23, 24]

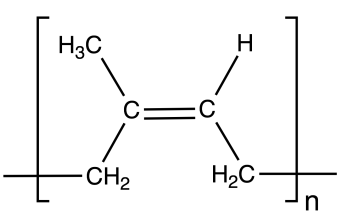

(a) Cis-1,4-polyisoprene (NR); $T_g = -60$ °C

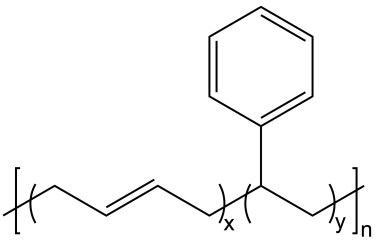

(b) Styrene butadiene rubber (SBR); $T_g = -65 \cdots -10$ °C

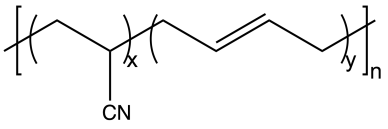

(c) Nitrile butadiene rubber (NBR); $T_g = -45 \cdots -5$°C

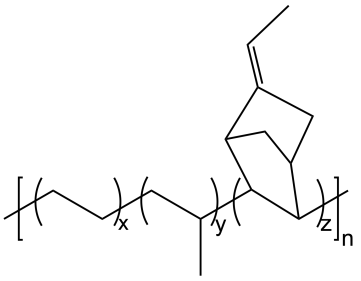

(d) Ethylene propylene diene rubber (EPDM); $T_g = -55 \cdots -10$ °C

Figure 1.1.: Chemical structure of selected polymer types.

polymer.[4]

Since every polymer shows a viscous flow behaviour beyond the rubber elastic plateau, it is not possible to create practically usable samples, which are dimensionally stable over time. Therefore, the polymer needs to be cross-linked, i.e. the polymer chains are interconnected via permanent covalent bonds. There are various ways to create these additional network junctions - the most commonly used cross-linking agents are either sulphur or peroxide. While the latter creates carbon-carbon (C-C) bonds between chains [27], sulphur is used as an intermolecular bridge of variable length (S_x with x usually between 1 and 8 [28]). This network formation-process is often referred to as vulcanization or curing-reaction (for more details see [29]). Consequently, cured elastomers show enhanced mechanical properties like an increased tensile strength, a large deformation at break and a lowered energy dissipation compared to non-cross-linked melts. Moreover, these properties depend on the amount and structure of the cross-links within the system.[30, 31]

However, cross-linking alone is usually not sufficient in most applications of elastomers like seals, tires or hoses. In most cases the mechanical stiffness and -strength needs to be increased even further. Therefore, various types of fillers are used to reinforce the elastomer, i.e. create an elastomer-composite.[32–35] The most commonly used types of fillers in case of rubber are carbon black (CB) and precipitated silica (Si). Recently, also nano-scaled fillers like carbon

[4]The former defines the height of the plateau, (the material stiffness or more precisely the modulus) whereas the latter is connected to the width of the plateau[26]

nanotubes (CNT) [36], graphenes [37] or carbon nanohorns (CNH) [38] have been extensively studied as reinforcement materials for elastomers.
The presence of fillers inside the polymer matrix has several effects on the overall behaviour of the composite. Apart from simple hydrodynamic reinforcement [39, 40], there are usually complex structure-formation processes, which form a random, self-similar filler network [41–44] additionally to the aforementioned physical- (entanglement-driven) and chemical network (from permanent cross-links). One crucial ingredient to the understanding of these reinforcing filler-structures is a fundamental insight into the polymer-filler interaction mechanisms. Apparently, the filler influences the polymer on various length-scales. On a molecular level, the surface of the filler strongly determines the way how interactions with polymer-segments can ultimately be formed. It is known for CB to have a unique surface characteristic due to the presence of graphitic crystals [45] with defects and cavities in their vicinity.[46, 47]
To characterize the surface of fillers, the technique of static gas adsorption is one of the most sensitive methods. Here, gas molecules are applied onto the filler-surface and the adsorbed volume is monitored as a function of pressure to measure the surface coverage. Its pressure-dependent value gives rise to certain – scale-dependent – characteristic features of the surface:

(i) On the smallest length-scale, the energetic profile via an energy distribution function is accessible.[5][48]

(ii) Close to, and slightly above the amount of gas, which covers the surface with one monolayer, the specific surface-area can be evaluated.[6][49]

(iii) Well above the mono-layer coverage, i.e. in the multi-layer regime, the surface roughness can be approximated via the surface fractal dimension.[7][50]

In section 2.2 more details about the theory of gas adsorption will be discussed. Following from point (iii) above, the concept of fractals becomes apparently important even on the scale of molecules that are covering the surface of the filler. Since Mandelbrot introduced fractals [51, 52], self-similarity was identified to be an important feature also in nano-filler reinforced elastomer composites (often referred to as elastomer nano-composites). Especially beyond only locally important features like the surface-inhomogeneity or -roughness, fillers additionally form structures on scales of several hundred nano-meters, i.e. aggregates and agglomerates (or clusters).[8] To characterize these structures in a quantitative way by applying the concepts of fractal objects, images are captured via a transmission electron microscope (TEM).[53] Consequently, this intermediate length-scale – between the molecular details of the filler-surface and the meso- to macroscopic effect of the three-dimensional filler network structure – serves as important bridge to understand certain characteristics of elastomer nano-composites (See section 2.3 for more details).
The filler network is therefore on the one hand determined by facets originating on small length-scales like the polymer-filler interaction; and on the other hand macroscopically effective by

[5] Here, the pressure is very low, and hence the amount of gas molecules is well below the amount of the monolayer coverage.

[6] The dominant length-scale here is the size of the primary particle - the smaller the primary particle the bigger the specific surface area.

[7] At pressures close to the saturation vapour pressure, the relevant length-scale for the surface roughness is the average curvature between the primary particles - see figure 2.6

[8] An agglomerate usually consists of several primary aggregates.

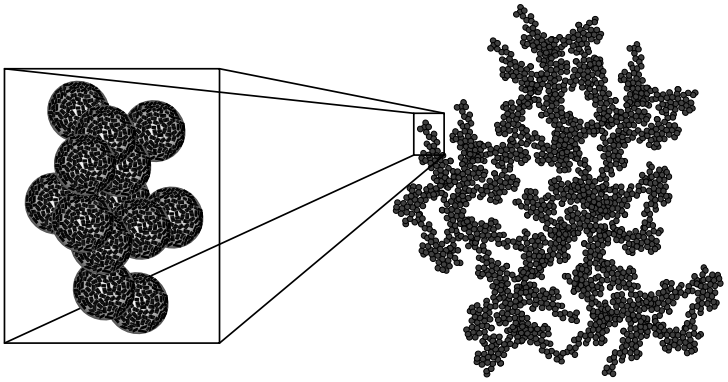

Figure 1.2.: Left hand side: Illustration of the CB structure including its surface features like graphitic crystallites and corresponding defects like edges and cavities. On the right hand side, there is a sketch of part from the 3-dimensional filler network structure on larger scale.

dominating the mechanical characteristics of a rubber sample (see figure 1.2). Obviously, there needs to be a sufficiently large amount of filler aggregates to form a continuous, 3-dimensional network. Below a certain critical amount of filler, there is just hydrodynamic reinforcement and thus above this threshold – described by percolation theory – there is a fractal network apparent.[54, 55] In figure 1.3 the effect of CB level is depicted exemplary for the uni-axial tensile test for two different types of polymer. In general, the overall stiffness of the material, i.e.

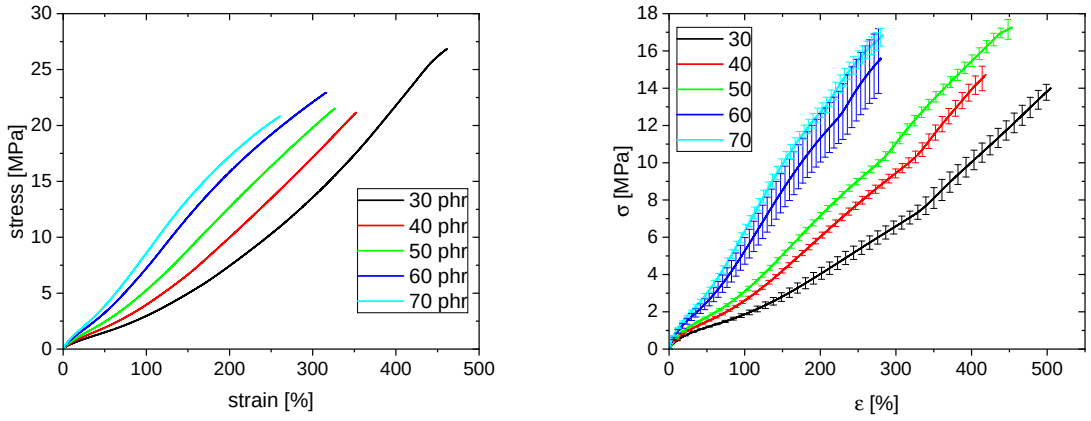

(a) NR (b) EPDM

Figure 1.3.: Tensile tests for NR and EPDM with varying filler level. The amounts are given in phr: per hundred rubber.

most obviously the stress at certain levels of strain[9] increases with the amount of CB. Furthermore, the ultimate properties change significantly as well. For both depicted types of polymer the ultimate strain at break decreases systematically with increasing filler level. Compared to

[9]These stress-values are often called moduli (e.g. modulus 100 - M100 for the stress at 100 % strain), however they must not be confused with a real modulus, which is defined via the ratio of the incremental changes of stress σ and strain ϵ: $G \propto \mathrm{d}\sigma/\mathrm{d}\epsilon$.

the unfilled polymers there is often first an increase of the elongation at break and at around the percolation threshold there is a maximum after which the value decreases accordingly.[56] However, the case of NR is special in this regard since the strain at break systematically decreases (at similar stress values) with filler level. This effect can be attributed to the NR specific feature of strain-induced crystallization (SIC), where due to local stretching of polymer strands a collective alignment is observable, which forms hard crystallites, reinforcing the NR matrix.[57–59] Although cross-linked rubber should be considered as a non-linear material, i.e. its characteristic properties like modulus show usually dependencies on various parameters like temperature, frequency or strain amplitude, there are certain conditions where it behaves linearly. For instance at small frequencies and temperatures far above the glass transition, the modulus shows almost no dependency on the dynamic strain amplitude until reaching ≈ 100 %.
However, introducing filler also enhances the non-linearity of the material significantly. Applying an oscillatory dynamic load leads to one of the most pronounced and important non-linear effects for filled rubbers: With continuously increasing strain amplitude the dynamical stiffness shows a pronounced drop after a critical strain value is reached. This effect is meanwhile widely known as Payne-effect.[32]

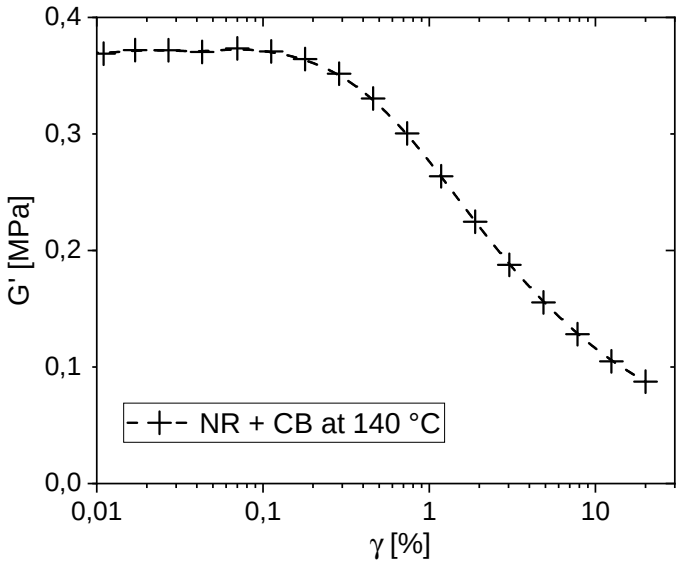

Figure 1.4.: Example of the drop of storage modulus (real part of the complex modulus) as a function of strain amplitude. Here, non-cross-linked NR filled with CB has been measured at 140 °C in a rheometer.

In figure 1.4 exemplary data is shown, which will be discussed later in section 4.3.2 in more detail. A first phenomenological description of this softening effect of rubber was found by Kraus in 1978.[60] Several works have been published since that time to find a physical interpretation i.e. a theoretical foundation of the Payne effect: [42, 43, 61–64] or recently [65]. Up to this point, there is no generally accepted model to fully describe the molecular processes governing the Payne-effect. Nevertheless, there is strong evidence that a break-down of the filler-network is the main cause for the observed softening effect.
Moreover, there is also a strain-induced decrease in stiffness observable in the limit of quasi-static deformations. This effect was first discussed and described by Mullins, which is why it is often referred to as Mullins-effect.[66] Also this characteristic behaviour of elastomers

was discussed intensively in literature e.g. [34, 67, 68], special focus in this work should be on a model developed by Klüppel and co-workers called the Dynamic-Flocculation Model (DFM)[19, 41, 42, 44, 69–73]. In section 2.4.3 an introduction into the basics of this model will be given.
To experimentally observe the Mullins-effect, a sample is usually stressed to a certain strain value and is afterwards unloaded to either a stress-free state or if possible to zero strain[10]. The maximum strain is then successively increased to a higher level. One example of a cyclic ten-

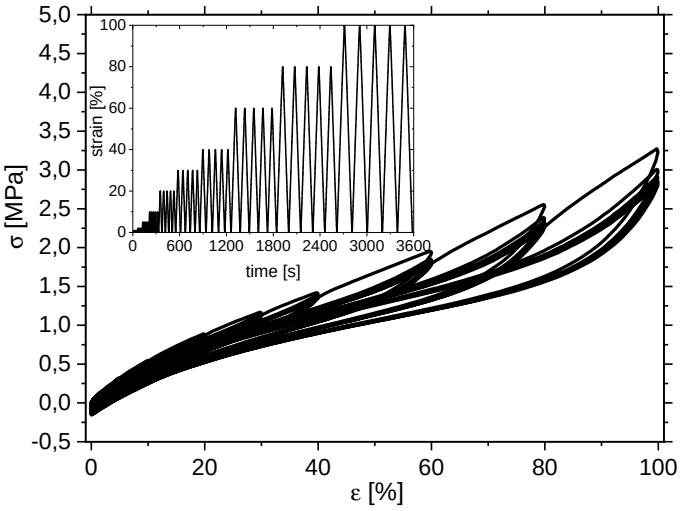

Figure 1.5.: Cyclic uniaxial tensile test to evaluate the Mullins-effect. The inset indicates the time sequence of the stress-strain cycles.

sile test is depicted in figure 1.5 and is often referred to as multi-hysteresis test since there is a significant difference between the loading- and de-loading curves. This effect is connected to an energy dissipation mechanism, which is attributed to a successive break-down and re-agglomeration process during the loading profile. While the Mullins-effect is usually only observable in cross-linked rubbers,[11] the Payne-effect occurs also in non-cross-linked melts. Therefore, analysing the material characteristics during a dynamic-mechanical strain sweep (to observe the Payne-effect) beyond just the mechanical analysis from rheological oscillatory shear experiments would be even more elucidative.
One technique to get additional insights into the material is the broadband dielectric spectroscopy (BDS). Here, in principle a capacitor is formed, where the sample is placed between two electrodes and is therefore used as the dielectric medium. By applying a varying weak electric field to the sample, the capacity of the system can be measured.[74] In general the impedance and the permittivity are evaluated as complex functions of the frequency. For non-conductive materials, i.e. unfilled- or silica-filled rubbers, the glass-transition as well as other characteristic time-scales of polymers are accessible from the loss-permittivity[12].[75] In case of

[10] Because of a permanent set of the sample this is only possible for dumbbell shaped specimen since they can be loaded under compression.
[11] Since for most elastomers, the time scale of the quasi-static experiment is too long compared to their reptation-time, thus the material would be dominated by its flow-behaviour rather than a filler induced strain softening.
[12] The imaginary part of the complex permittivity

conductive samples, the conductivity as a function of frequency will give important informations about processes inside the material.[76–79] Especially the percolation threshold can be analysed very precisely since the value of the conductivity changes significantly close to the critical volume fraction of filler.[13] Consequently, measuring the dielectric spectrum during a mechanical measurement, i.e. simultaneously monitoring the e.g. modulus and conductivity as a function of strain amplitude, can give rise to further knowledge about the nature of the filler-network structure. In figure 3.6 in section 3.4 one possible experimental set-up, which was used in this work, is sketched and in 4.3 a detailed discussion of combined dielectric-rheological measurements can be found.

Thus, the aim of this work is to elucidate the nature of the interaction between polymer chains and fillers.To achieve this goal, several length-scales need to be investigated. First, on a macroscopic scale, there are (i) the (physical) network of entangled polymer chains, (ii) in cross-linked rubbers there is the chemical network – creating a synergistic additional network-structure[14] – and (iii) in (sufficiently) filled elastomers there is the filler network formed inside the other networks.[15] However, all macroscopically active, characteristic properties of the different networks originate on the molecular-scale, i.e. the details of their respective building blocks like the monomers, the curing agents or the filler aggregates.
This work is therefore structured in the following way: After a theoretical introduction into the most important topics of this work (chapter 2), an experimental chapter will summarize the used experimental conditions for each test performed in this work (chapter 3). Finally, the main results are presented including a discussion with respect to the aforementioned aspects of the role of polymer-filler interactions in elastomer nano-composites (chapter 4). Therefore, at first, utilizing static gas adsorption measurements, the smallest relevant length-scale of the polymer-filler interaction – hence the surface of the filler – will be analysed (section 4.1). In particular, a surface modification, applying an ionic liquid onto the surface is used to modify the surface-activity in a characteristic way (Details can be found in section 3.3.2).[80] Consequently, these changes cause significant effects on the macroscopic length-scale observable in the rheological experiments performed on non-cross-linked melts (section 4.3). To understand the intermediate length-scale of the filler aggregates and agglomerates, cross-linked samples filled with a structure-modified CB were analysed using TEM images. Findings on this length-scale have been compared to various macroscopic tests (section 4.2). Finally, in chapter 5 a conclusive summary of all main results will be given.

[13] In a typical CB-filled elastomer it can vary over 10 orders of magnitude from being insulating to conductive.

[14] With an increasing number of chemical cross-links, the number of entanglements, which are trapped between (minimum) two cross-links is also increasing. These trapped entanglements are mechanically as effective as the permanent links.

[15] Obviously, there can also be the case of only the physical- and filler-network being present in non-cross-linked polymer melts.

2. Theoretical Background

In this chapter there will be a brief introduction into some important theoretical concepts for understanding the materials used in this work. The focus is first on polymers and their non-linear response to deformations, i.e. the theory of rubber elasticity. Following is an introduction to different methods how to characterize the surface of filler particles.
A brief introduction is given on how to extract structural properties of the filler particles from TEM images. Finally, the theory of rubber-reinforcement, i.e. how filler characteristics influence the polymer-filler interaction, is introduced.

2.1. Rubber elasticity – A brief theoretical introduction

Everyday experience suggests a fundamental difference in the response of materials like metals or ceramics to deformations compared to rubber-like materials. The former being rather stiff and not easy to deform, whereas the latter are softer and able to deform up to very large extensions. There are several theoretical approaches to explain this special characteristics and in the following sections the most import concepts will be briefly introduced.

2.1.1. Entropy elasticity

The fundamental difference in the mechanical properties of rubber-like materials and conventional materials such as steel is well known from our daily life. Scientifically it was first explained by Kuhn [81] who looked at the free energy F of different materials:

$$F = U - TS. \tag{2.1}$$

In the case of steel[1] the stress σ, equivalent to the change of the free energy $dF/d\lambda$ with respect to the elongation λ, is dominated by the change of free energy $dU/d\lambda$ resulting from atomic displacements within the crystal-lattice. However, for rubber the situation is very different since the material consists of long flexible polymer chains [81] which leads to a change in entropy $dS/d\lambda$ dominating the stress contribution. James and Guth [82] and [83] derived an analytical expression for this entropy elasticity of rubber.
One main assumption for the resulting entropy-driven force is a Gaussian distribution of chain end-to-end distances $\vec{R}$, showing all possible conformations Ω of chains with an average length

[1] or any other material with some crystalline structure

of N segments:

$$P(\vec{R}) = \frac{\Omega(N,\vec{R})}{\int \Omega(N,\vec{R})d\vec{R}} = \left(\frac{3}{2\pi\left\langle \vec{R}^2 \right\rangle}\right)^{3/2} \exp\left\{-\frac{\vec{R}^2}{2\left\langle \vec{R}^2 \right\rangle}\right\}. \tag{2.2}$$

With $< \vec{R}^2 >= Nl_s^2$ the mean square displacement of the chain-ends and l_s the length of a statistical chain segment. Taking into account all these possibilities, i.e. conformations Ω of arranging itself, the entropy $S = k_B ln(\Omega)$ for the chains can be defined. Neglecting the change of internal energy $dU = 0$ the Gibbs free energy (2.1), using (2.2), is:

$$F = C(T) + \frac{3k_BT}{2\left\langle \vec{R}^2 \right\rangle}\vec{R}^2. \tag{2.3}$$

Here, $C(T)$ is just a temperature dependent constant. For n chains, which are stretched, i.e. the end-to-end distance changes according to $\vec{R}_0 = (x,y,z) \rightarrow \vec{R} = (\lambda_x x, \lambda_y y, \lambda_z z)$, the change in free energy ΔF is given by:

$$\Delta F = \left(\frac{nk_BT}{2}\right)\left(\lambda_x^2 + \lambda_y^2 + \lambda_z^2 - 3\right). \tag{2.4}$$

For the special case of an uni-axial deformation assuming constant volume during deformation, i.e. $\lambda_x = \lambda$ and $\lambda_y = \lambda_z = 1/\sqrt{\lambda}$ the free energy becomes:

$$\Delta F = \left(\frac{nk_BT}{2}\right)\left(\lambda^2 + \frac{2}{\lambda} - 3\right). \tag{2.5}$$

To finally calculate the stress-strain relation, the definition of stress as ratio between force f and initial cross-sectional area A_0, i.e. $\sigma \equiv f/A_0$ is used:

$$\sigma = \frac{1}{V_0}\left(\frac{\partial \Delta F}{\partial \lambda}\right)_{T,V} = \nu k_B T\left(\lambda - \frac{1}{\lambda^2}\right), \tag{2.6}$$

with $\nu = n/V_0$ as the density of network chains per volume V_0. One important feature of equation (2.6) is the proportionality to the temperature T which leads to an increase of force with increasing temperature. For instance: Heating a rubber band leads to a contraction, resulting in a measurable force.[2] In contrast to a perfect elastic law like the Hook's law where there is just a linear relation between force and elongation $f \propto L$, for the simplest model of rubber elasticity an additional term $f \propto 1/\lambda^2$ in (2.6) is apparent, which is why it is also called the Neo-Hooke law of rubber elasticity.
Moreover, the Young's modulus E defined via $E = \left(\frac{d\sigma}{d\epsilon}\right)_{\epsilon=0}$ with $\epsilon = \lambda - 1$, yields the relation for the material stiffness following the Neo-Hookean law $E = 3\nu k_B T$ and accordingly the shear modulus for incompressible material is obtained:

$$G \approx E/3 = \nu k_B T = \nu_c RT = \frac{\rho RT}{M_c}. \tag{2.7}$$

[2]To observe this typical effect of rubber elasticity, the rubber band needs to be pre-stretched, otherwise there will be no contraction since the chains are all already in their preferred, coiled state.

Here, ν_c is the molar number of network chains, ρ is the mass density and M_c is the molar mass of the respective network chains, i.e. network-strands between cross-link junctions. However, this simple model of rubber elasticity is only valid for small deformations and it neglects the effect of entanglements between chains. Therefore, additionally to the physically based Neo-Hooke model, a diversity of various models have been developed within the last decades, which all try to describe the hyperelastic response of rubber.
To mention only a few, there are phenomenological models like the Mooney model [84], Mooney-Rivlin model [85], the Gent model [86] or the Yeoh model [87].[3] Finally, important improvement in the field of rubber elasticity was made, when the concept of topological constraints via different tube models was developed. First started by Edwards [8] and later further developed by Vilgis, Heinrich, Gaylord [9, 12, 13, 89] or Rubinstein, Panyukow [90] or Mergell and Everaers [20].

2.1.2. Tube model

Non-affine extended tube model

Essential to all tube model approaches is the idea of a polymer chain, topologically constrained inside a tube-shaped volume, caused by the presence of surrounding chains, which are entangled with each other. In figure 2.1 the basic principle is visualized. Due to the length of each chain, the chains hinder each other in their movement caused by thermal fluctuations. Therefore, a chain is only free to move within a specific volume, which is due to the rather linear character of a chain, shaped like a tube with diameter d_0.[4] Spatial areas, which are impeding a chain to move,

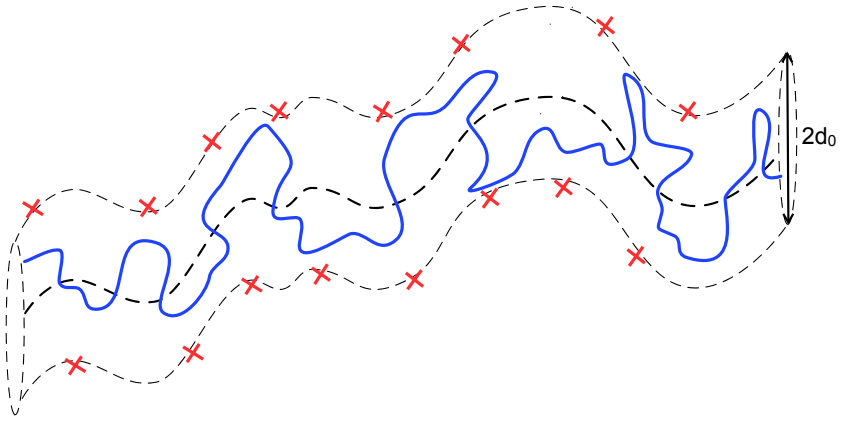

Figure 2.1.: Schematic picture of a tube (dashed lines as outer limits), i.e. topological constraints for a single chain (thick blue line), which is caused by localizations like entanglements or cross-links (red crosses) with other chains (not visible) in the vicinity of the chain

are called localizations. These localizations can be caused by either physical entanglements or

[3] For a review of different models see for example: [88]
[4] d_0 denotes the tube diameter, i.e. the average distance between entanglements for polymer chains in the melt.

chemical cross-links. Both contribute to the overall macroscopic stiffness i.e. the modulus of a sample. Note, that in the Neo-Hooke model (2.6) there is only the contribution of the chemical cross-links.
Heinrich et al. [10] first considered a non-affine deformation[5] for the tubes: $d_\mu = d_0\lambda_\mu^\nu$, with $\nu = 1/2$.[6] For the free energy density W of the material this leads to:

$$W = W_c + W_e = \frac{G_c}{2}\left(\sum_{\mu=1}^{3}\lambda_\mu^2 - 3\right) + 2G_e\left(\sum_{\mu=1}^{3}\lambda_\mu^{-1} - 3\right). \tag{2.8}$$

Here, G_c represents the cross-link modulus defined as:

$$G_c = A_c\nu_{mech}k_BT. \tag{2.9}$$

The pre-factor A_c takes into account constraints on fluctuations of network-junctions, hence is a function of the average range of junction-fluctuations d_c[7] and the average end-to-end distance between two junction points R [91].[8] $\nu_{mech} = \left(\nu_c - \frac{2}{f-2}n_P\right)$ is the mechanically effective network density including ν_c and n_P as the density of chains between cross-links and the total number of chains respectively.
The pre-factor G_e of the second addend in (2.8) is related to the entanglement contribution:

$$G_e = \frac{\rho N_A l_S^2 k_B T}{4\sqrt{6}M_S d_0^2}, \tag{2.10}$$

with ρ as the mass density, l_S and M_S is the length and molar mass of a statistical chain segment, d_0 denotes the tube diameter and N_A, k_B and T have their usual meaning. The essential difference between both contributions lies in the response of the system at different time scales. A localization due to a chemical cross-link is permanent and therefore stable at longer time scales, whereas physical entanglements can slide off i.e. the effect of the localization is decreasing with time. For a non cross-linked polymer melt, this effect is observable as the terminal viscous flow regime [25]. With increasing cross-link density more of these entanglement localizations will be trapped between neighbouring cross-links, hence cannot disentangle over longer time scales. Although the non-affine tube model was a big step forward, still it is not able to explain all features of the stress-strain response of a typical rubber i.e. the strong non-linear behaviour at large deformations due to finite chain extensibility. Therefore, it was crucial to add a finite extensibility term into equation (2.8) [12, 17]:

$$\begin{aligned} W = &\frac{G_c}{2}\left[\frac{\left(\sum_{\mu=1}^{3}\lambda_\mu^2 - 3\right)\left(1 - \frac{T_e}{n_e}\right)}{1 - \frac{T_e}{n_e}\left(\sum_{\mu=1}^{3}\lambda_\mu^2 - 3\right)} + \ln\left(1 - \frac{T_e}{n_e}\left(\sum_{\mu=1}^{3}\lambda_\mu^2 - 3\right)\right)\right] \\ &+ 2G_e\left(\sum_{\mu=1}^{3}\lambda_\mu^{-1} - 3\right). \end{aligned} \tag{2.11}$$

[5] Affine deformations are equivalent to linear transformations, i.e. deformations are equivalent on all length-scales.

[6] This result was later confirmed by small-angle neutron scattering (SANS) results [15].

[7] d_c is usually of a similar order of magnitude than the tube diameter d_0, hence assuming that chain segments and network junctions have a similar fluctuation range.

[8] $A_c = 1 - \frac{2}{f}\left(1 - \frac{2K\exp\{-K^2\}}{\sqrt{\pi}erf(K)}\right)$ with f as functionality and $K = \sqrt{\frac{3f}{2}}\frac{d_c}{R}$.

The additional term in the first addend includes n_e and T_e as number of segments between entanglements and the trapping factor respectively ($0 < T_e < 1$). Thus, the ratio n_e/T_e yields the number of chain segments between trapped entanglements, i.e. entanglements which can no longer slip off. In the limit of $T_e/n_e \to 0$, equation (2.8) is found again. This extended non-affine tube model is very well confirmed by several experimental studies [15, 88, 92, 93] and should be the model to choose in case of unfilled elastomers.[9]

2.2. Characterization of filler surfaces by static gas adsorption techniques

2.2.1. Essentials of physisorption

The fundamental thermodynamics of physical adsorption and theoretical models are discussed and presented e.g. in [48]. This section will thus only present the most important ideas of describing the process of gas adsorption empirically.
First attempts to characterize experimental adsorption isotherms have been carried out by Freundlich [95] and later by Langmuir [96]. In typical adsorption experiments the amount of gas is measured as a function of adsorptive pressure p. At low pressures the Freundlich isotherm equation

$$V(p) = Ap^{1/n} \tag{2.12}$$

is in most cases valid. The empirical parameters A and n can be derived from linear fits in double logarithmic plots of the isotherm (See section 4.1). From the parameter n some rough information about the energetic heterogeneity of the surface can be obtained. Perfectly homogeneous surfaces yield a parameter of $n = 1$.[10] Often the value of nRT is often more useful than n, because it takes into account the effect of temperature in a first approximation.[11]
At higher pressures, the Freundlich isotherm (2.12) will systematically deviate more from measurements. A better result can be achieved by using the Langmuir isotherm equation, which will be derived in the following under the assumptions of (i) a homogeneous surface, (ii) no interactions between gas molecules and (iii) no multilayer adsorption effects.

As depicted in figure 2.2 there is a total number of $N = N_0 + N_1$ sites on the surface, which are either occupied by gas molecules (N_1) or empty (N_0). Gas molecules move in the gas phase and can interact with the surface for a characteristic adsorption time τ and after this process are desorbed again from the surface.[12] The number of gas molecules per mole hitting the unit area per second is given by:[97]

$$\mu = \frac{p}{\sqrt{2\pi MRT}}. \tag{2.13}$$

[9] However, there are of course other tube models like the slip-tube model from Rubinstein and Panyukov [90] or the double tube model from Mergell and Everaers [20], which are as well able to describe all relevant features of rubber elasticity (see e.g. [94])
[10] Accordingly, more heterogeneities increase the value of n
[11] For more details see ref. [48] and references therein.
[12] A typical adsorption time τ is of the order 10^{-13} s to 10^{-12} s [48].

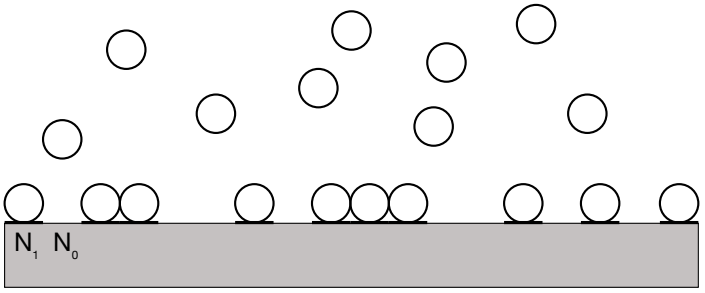

Figure 2.2.: Illustration of gas adsorption according to the Langmuir model. There are only two different types of sites: occupied (N_1) or empty (N_0). The surface is assumed to be homogeneous, there is no lateral interaction between the molecules and there is no multilayer adsorption.

With M the molar mass of the gas molecules, R the gas constant and T the respective temperature. Next step is the definition of rates of adsorption κ_{ads} and desorption κ_{des}, respectively. The rate of adsorption depends on the fraction of free sites on the surface $\theta_0 = N_0/N$ hence the more empty sites are present, the more likely it is for a molecule to be adsorbed. Furthermore, κ_{ads} will depend on the fraction of molecules, which actually condense on the surface after hitting it: $k_{ads}\mu$ with k_{ads} as an equilibrium constant. Consequently, the rate of desorption will be proportional to the portion of occupied sites on the surface $\theta_1 = N_1/N$ and an equilibrium constant on a completely covered surface k_{des}.
Following these assumptions both rates yield the expressions:

$$\kappa_{ads} = k_{ads}\mu\theta_0 \tag{2.14}$$

$$\kappa_{des} = k_{des}\theta_1. \tag{2.15}$$

First, no site will be covered i.e. the adsorption rate will dominate the process. After a certain time, the system will reach an equilibrium ($\kappa_{ads} = \kappa_{des}$) where adsorption and desorption will be equally probable:

$$k_{ads}\mu\theta_0 = k_{des}\theta_1. \tag{2.16}$$

Using furthermore,

$$\theta_0 + \theta_1 = 1 \tag{2.17}$$

this leads to

$$\theta_1 = \frac{k_{ads}\mu}{k_{des} + k_{ads}\mu}. \tag{2.18}$$

Introducing the equilibrium constant b_L equation (2.18) with $\Theta = \frac{n_1}{n}$ as the molar coverage becomes the well known Langmuir isotherm equation:

$$\Theta(p) = \frac{b_L p}{1 + b_L p} \tag{2.19}$$

with

$$b_L = \frac{k_{ads}}{k_{des}\sqrt{2\pi MRT}}. \tag{2.20}$$

The value of k_{ads} is always very close to unity (see ref. [96]) and the desorption parameter is inversely proportional to the adsorption time τ, $k_{des} = 1/\tau = (1/\tau_0)exp\{-Q/RT\}$ with the heat of adsorption Q. At low pressures p there is a linear increase in the Langmuir equation (2.19) with $b_L p$, which corresponds to the Freundlich isotherm (2.12) in the limit of $n = 1$. In contrast to the Freundlich isotherm, the Langmuir isotherm reaches a saturation level $\Theta = 1$ towards high pressure values, which reflects the filling of the surface as a mono-layer of gas molecules is formed.
There were numerous different approaches to describe an isotherm empirically. Only one important example should be mentioned in this section.[13] Bradley first considered a modified semi-empirical Freundlich isotherm equation, which fixed the weakness of not tending to a limiting coverage: [48]

$$\Theta(p) = \frac{(Ap)^{1/n}}{1 + (Ap)^{1/n}}. \tag{2.21}$$

All of these isotherms are not capable of describing the adsorption beyond a mono layer coverage. Actually, it was Langmuir who first described multilayer adsorption in his paper from 1918 (see Ref. [96]). But it is the work of Brunauer, Emmett and Teller from 1938 [49] that is most often cited with respect to multilayer adsorption.[14] The isotherm equation for the BET model has the following form:

$$\frac{V}{V_m} = \Theta(p) = \frac{1}{\left(\frac{p_0}{p} - 1\right)\left[\left(1 - \frac{1}{C}\right)\frac{p}{p_0} + \frac{1}{C}\right]}. \tag{2.22}$$

Here, V_m is the volume of one mono-layer of gas covering the surface. $C \propto \exp\left\{\frac{Q_m - Q_{ads}}{RT}\right\}$ is a constant proportional to the difference between the heat of adsorption of the gas molecules in the mono-layer Q_m and of those in the gas phase Q_{ads}. The BET model is most often used to calculate the mono-layer volume V_m from the measured isotherm $V(p)$. Knowing the cross-sectional area of the molecules σ

$$\sigma = 2\sqrt{3}\left[\frac{M}{4\sqrt{2}N_A\rho_L}\right]^{2/3} \tag{2.23}$$

and using

$$A_s = \frac{V_m \sigma N_A}{V_{mol}} \tag{2.24}$$

the specific surface area A_s can be obtained. M is the molar mass, N_A is the Avogadro number and ρ_L is the mass density of the gas molecules in the liquid, i.e. condensed state and finally

[13] More possible empirical isotherm equations are mentioned e.g. in [48]
[14] Hence, often referred to as BET model.

V_{mol} is the molar volume. To easily obtain the volume of a mono layer V_m, it is often more useful not to use the BET isotherm in the form of equation (2.22), but to plot it in the following form:

$$\frac{p}{V\,(p_0 - p)} = \frac{C-1}{C\,V_m}\frac{p}{p_0} + \frac{1}{C\,V_m}, \tag{2.25}$$

as function of p/p_0. Accordingly, one expects a linear function $y = Ax+B$ with slope $A = \frac{C-1}{CV_m}$ and intercept $B = \frac{1}{CV_m}$. This leads to the easy expressions for the mono layer volume $V_m = \frac{1}{A+B}$ and $C = \frac{A}{B} + 1$. With this, the isotherm $V(p)$ can be normalized, to obtain the surface coverage $\Theta(p) = \frac{V(p)}{V_m}$. A typically applicable range of the BET equation (2.25) to coincide with experimental data is regime II depicted in figure 2.3. In the following two sections, the

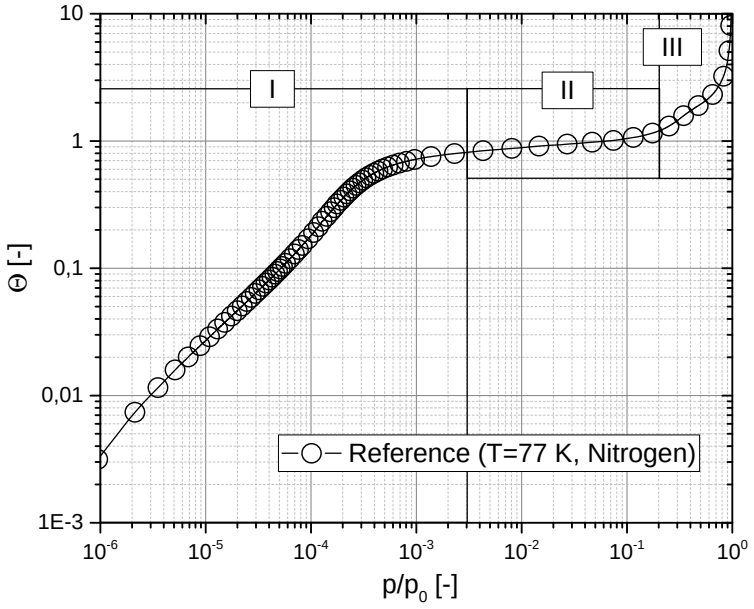

Figure 2.3.: Example adsorption data of a reference carbon black to illustrate the main regimes of adsorption. The coverage $\Theta = V/V_m$ is plotted versus the normalized pressure p/p_0 with p_0 as the saturation vapour pressure at the measured temperature. The indicated regimes are: (I) Dominated by energetic characteristics e.g. heterogeneity, (II) Coverage of the surface by one mono layer, i.e. BET regime to evaluate V_m and (III) Multi layer adsorption – dominated by surface roughness

remaining two regimes of figure 2.3 are discussed. First, the role of energetic heterogeneity will be explained, followed by an analysis of the surface roughness, which is responsible for the multi-layer adsorption characteristics.

2.2.2. Adsorption on heterogeneous surfaces: Evaluation of the surface energy distribution in the low pressure regime

In figure 2.3, the surface coverage of a typical homogeneous graphitized carbon black is depicted. In the first regime, the volume of adsorbed gas molecules increases linearly with increasing pressure, i.e. the volume is filled up with a behaviour well represented by the Freundlich isotherm (2.12) with $n \approx 1$. However, in most of the cases, the initial regime will not follow this simple law i.e. $n > 1$ is usually valid. Especially for typical carbon blacks used in rubber applications, the surfaces will have certain characteristic features.

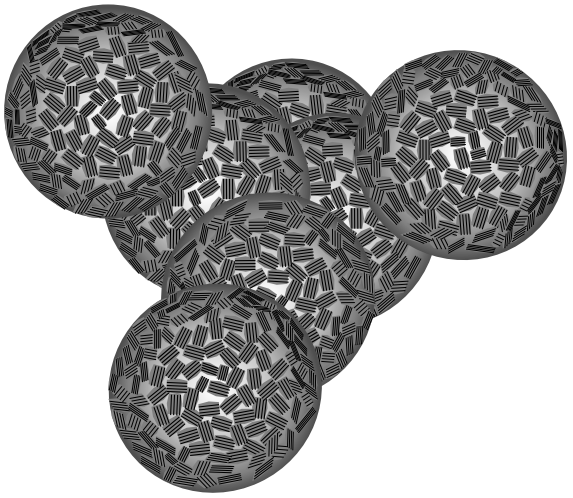

Figure 2.4.: Schematic view of the surface-structure of a typical carbon black primary aggregate.

Figure 2.4 shows a sketch of the structure of a typical primary aggregate. Every aggregate consists out of three to ten primary particles[15]. On the surface of each primary particle graphitic crystallites, with approximately a size of about 2 to 9 nm, are present [98, 99]. Therefore, for typical carbon black surfaces the level of heterogeneity will be a substantial feature. Although the Freundlich model of adsorption allows a rough qualitative estimation of the level of energetic heterogeneity, a more quantitative evaluation is necessary.
Experimental adsorption isotherms $\Theta(p)$ represent in general an average over all existing energies Q on the gas-solid interface. This averaging can mathematically be expressed in a well known Fredholm integral equation [48]

$$\Theta(p,T) = \int_0^\infty \theta(p,T,Q) f(Q) dQ. \tag{2.26}$$

With $\theta(p,T,Q)$ as the local adsorption isotherm, representing the local coverage at given pressure p, temperature T and constant energy Q. $f(Q)$ denotes the distribution of energy sites present on the surface. To obtain the distribution function $f(Q)$, several numerical methods have been developed.[16] In any case, the crucial step is the choice of a proper model isotherm

[15] Depending on the type and structure of the carbon black.
[16] A detailed overview can be found here: [48]

$\theta(p, T, Q)$. Gas molecules with a certain kinetic energy, thus representing a specific temperature T, lead to a defined level of surface coverage. More specifically, the temperature defines the adsorption- and desorption rates, hence their ratio $b_L \propto k_{ads}/k_{des}$.[17] This leads to less surface coverage Θ at the same number of molecules, i.e. equal pressure p, at higher temperatures T. However, under isothermal conditions, the energy Q determines the coverage at a given pressure p. At very low pressure $p < 10^2 Pa$ (see the linear regime I in figure 2.3) the amount of molecules is very low. Accordingly, the molecules will first occupy the sites most favourable for them, i.e. the sites with highest energy Q. The probability for a certain site to be covered, is therefore depending on its energy Q and the present pressure p. This probability function is essentially represented by the local surface coverage $\theta(p, T, Q)$ needed for solving the integral equation 2.26. In figure 2.5 this interrelation is illustrated as a three dimensional plot of the extended Langmuir isotherm (see equation 2.27).

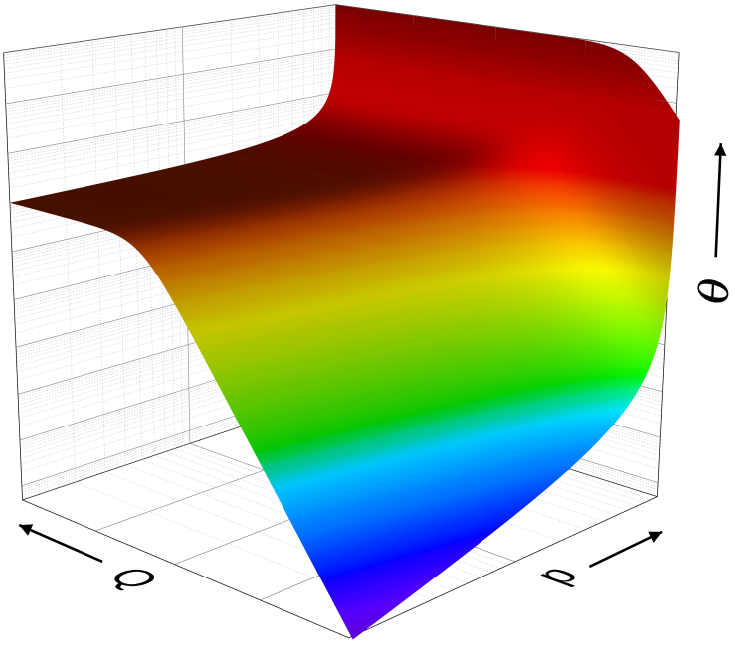

Figure 2.5.: Illustration of the model isotherm according to Langmuir. The local surface coverage θ, i.e. the probability a site is covered by a gas molecule, as function of the energy Q and the pressure p.

For better consistency, the simple Langmuir equation (2.19) is often modified. First, a multilayer correction according to the BET model is applied and secondly lateral interactions between the molecules are considered by a correction factor introduced by Fowler and Guggenheim (FG) [100]:

$$\theta(p, Q, T) = \frac{b_{BET}^2 b_{FG} b_L p}{1 + b_{BET} b_{FG} b_L p} \tag{2.27}$$

[17] Here, with the nomenclature of the Langmuir adsorption model (equation 2.20)

with

$$b_{BET} = \frac{1}{1 - \frac{p}{p_0}}, \tag{2.28}$$

$$b_{FG} = \exp\left\{\frac{z\omega\theta}{RT}\right\}. \tag{2.29}$$

Here, z is the number of neighbouring sites, ω is the lateral interaction energy and θ is the probability, that the neighbouring site is occupied by a molecule. There are two possible choices for the probability θ: (i) The local adsorption isotherm θ, hence assuming a patchwise distribution[18] or (ii) the global isotherm Θ, thus assuming a random distribution [47]. The surface of carbon black is considered to consist of graphite micro-crystallites [45], and therefore the choice of θ as probability function is more realistic.
With equation (2.27) to be used in (2.26) the energy distribution can be calculated by numerical algorithms. One of the most often used algorithm is the method of Adamson and co-workers [101–103].[19]

2.2.3. Adsorption on fractal surfaces: Evaluation of the fractal dimension of a surface

At low pressures, as was discussed above, the local structure of the surface dominates the adsorption behaviour. Consequently, the surface can be characterized on the sub-nm length-scale (see regime I in figure 2.3). At medium pressures, a mono layer is filled, thus one can get information about the specific surface area of the investigated sample (see equation (2.25) in section 2.2.1). Finally, regime III indicated at the high pressure side of figure 2.3 is dominated by the adsorption of gas molecules successively filling up multiple layers. Thus, the surface geometry will strongly influence the adsorption of further gas molecules.
There are different experimental approaches to obtain the surface roughness of carbon black particles. From more qualitative microscopic investigations using an atomic force microscope (AFM) [105, 106], to small-angle x-ray scattering (SAXS) [107] and gas adsorption techniques [46, 47, 104, 108], all investigating different length scales of the surface-structures. Therefore, the surface roughness obtained via these techniques lead to different results concerning the fractal dimension $2.0 \leq D_S \leq 2.6$ as characteristic value for the surface roughness.
Using gas molecules as yardstick is one of the simplest possibilities to probe the fractal nature of a surface. Here, the concept of fractals introduced by Mandelbrot [51, 52] is utilized by relating the mono layer coverage V_m with the cross-section σ (see equation (2.23)) of gas molecules of varying size:

$$V_m \propto \sigma^{D_S/2}. \tag{2.30}$$

Alternatively, the adsorption of a specific type of gas can be considered as a condensation process on the surface. A liquid film of thickness z will be formed and will grow with the number

[18] The sites of equal or similar energies are arranged in patches, i.e. areas of small size.
[19] Details can be found also here: [104]; In the appendix A.1.2 the python script for estimating the energy distribution in this work is given.

of molecules, hence the volume V will increase with the film thickness. Using again the relation from Mandelbrot for fractal surfaces:

$$\frac{V}{V_m} \propto \left(\frac{z}{z_m}\right)^{3-D_S} \tag{2.31}$$

with V_m and z_m as the Volume- and film thickness of one mono layer respectively. While the yardstick method is based on fundamental geometrical relationships on fractal surfaces, the method of relating the film thickness z with the volume V is based on the classical Frenkel-Hill-Halsey (FHH) theory of interaction of molecules on surfaces. The classical FHH theory was generalized for fractal surfaces by Pfeifer et al. [50, 109], taken not only the van-der-Waals (vdW) interaction into account, but also the capillary-condensation (CC) caused by the vapour-liquid surface tension.
In section 2.2.1 the basic principles of gas adsorption were discussed. One main assumption of a static gas adsorption measurement is thermal equilibrium, e.g. a balance between adsorption and desorption rate. Thus, it is reasonable to assume the same for the interaction between gas molecules and the surface. There will be attractive forces on one side and, based on the thermodynamic state of the system, a chemical potential μ, representing the energy needed to detach a molecule from the surface. In thermal equilibrium this leads to the following balance equation between the attractive interaction potential Φ and the chemical potential μ:

$$\Phi(z) = \frac{N_A \alpha}{z^3} + \frac{\gamma M}{\rho_L}\left(D_S - 2\right)\frac{1}{z} = RT \ln\left(\frac{p_0}{p}\right). \tag{2.32}$$

Here, the first addend is representing the attractive van-der-Waals potential with α as van-der-Waals interaction parameter and N_A the Avogadro constant. The second addend of (2.32) is the capillary-condensation term including the solid-liquid surface tension γ, the molar mass M, the density of the condensed gas ρ_L and the fractal dimension D_S of the surface. On the right side of equation (2.32) there is the negative chemical potential expressed via the logarithm of the ratio between saturation vapour pressure p_0 and pressure p multiplied by the molar gas constant R and the temperature T.
Considering the scaling relation (2.31) and $\ln(p_0/p)$ with z from equation (2.32), this leads to the following relation between the adsorbed volume V and the relative pressure p/p_0:

$$V \propto \left(\ln\frac{p_0}{p}\right)^{\kappa}. \tag{2.33}$$

Depending on the respective regime, κ will have different values:

$$\kappa = \frac{3 - D_S}{3} \text{ for the vdW regime} \tag{2.34}$$

or

$$\kappa = 3 - D_S \text{ for the CC regime.} \tag{2.35}$$

Hence, by plotting the surface coverage Θ versus $\ln(p_0/p)$, often referred to as fractal FHH-plot, one can easily find the fractal dimension D_S of a surface.
In section 4.1.1 some examples of classical FHH-plots will be shown. Additionally to this

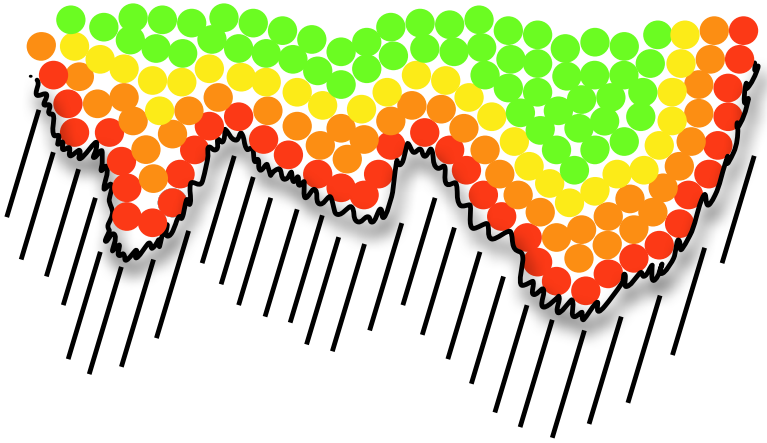

Figure 2.6.: Illustration of multi-layer adsorption on a randomly rough surface according to the fractal FHH-theory. For short range interaction, the van-der-Waals contribution is dominant (indicated by the molecules with red colour). For greater distances from the surface, there is a transition to the FHH regime (from orange over yellow to green molecules) dominated by capillary condensation.

classical approach, one can also try to plot directly the coverage Θ versus the film thickness z. For this purpose, equation (2.32) needs to be solved for z.[20] Assuming all other parameters are known, the film thickness z can be directly calculated from the pressure p. Note that the fractal dimension D_S needs to be known for this procedure. Hence, it is necessary to perform a classical FHH-plot and obtaining the scaling in the CC regime of the surface in a first step. After this, there are some benefits of this modified FHH approach. By calculating z from p and normalizing the film thickness with the thickness of one mono layer z_m, the point $1 = z/z_m = V/V_m$ must be found. At least for well defined surfaces, like graphite, this is a check for consistency, thus a proof of concept.
Furthermore, one can use this consistency check for unknown surfaces, to obtain their surface properties. One example is the van-der-Waals parameter α in equation (2.32):

$$\alpha = \frac{\pi}{6}\frac{\rho_s N_A}{M_s} I \alpha_g \alpha_s. \tag{2.36}$$

Here, ρ_s and M_s is the density and molar mass of the solid respectively, I is the potential for ionization of the gas molecules and α_g and α_s are the polarizabilities of the gas and the solid respectively [46]. Some values are known in the literature, e.g. adsorption for nitrogen an graphite, but in general there is a lack of knowledge in this parameter. Thus, the modified FHH method presented here is one way to get some estimations about how much the surface differs from a perfectly graphite-crystalline surface.
Using the assumption, that the point $(x, y) = (z/z_m, V/V_m) = (1, 1)$ must be found in the transformed FHH-plot for all surfaces, the van-der-Waals parameter α can be adjusted accordingly.[21] Figures 2.7 and 2.8 show the found values for nitrogen and 1-butene respectively. In

[20] The solution of this can be found in appendix A.1.1

[21] In principle the choice of the van-der-Waals parameter α as the free parameter is arbitrary. Only the lack of values especially in case of 1-butene and the found numbers in case of nitrogen on graphitic surfaces, which

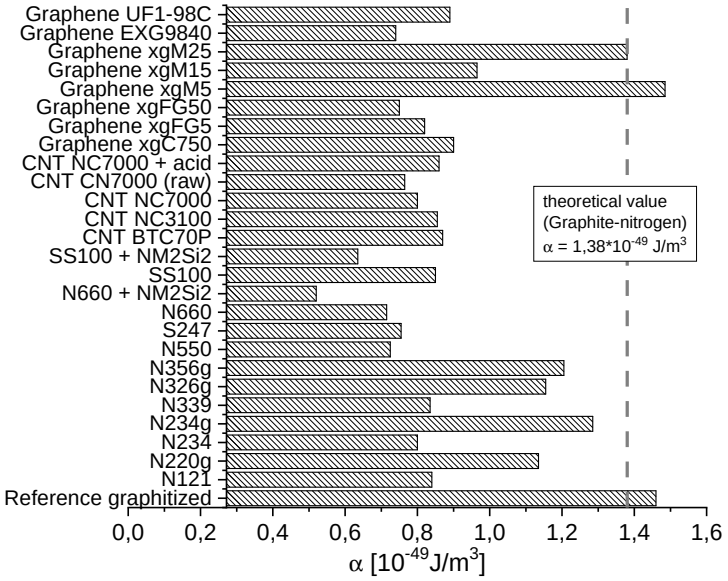

Figure 2.7.: Van-der-Waals interaction constants α for nitrogen (T=77 K) for various filler surfaces. The vertical dotted line represents the literature value of nitrogen on graphite.[110]

case of nitrogen there is a literature value of $1.38 \cdot 10^{-48}\ J/m^3$ available, which is also very well reproduced via this parameter fitting. Apparently, all graphitic surfaces are close to this value whereas all non-graphitic surfaces show a reduced interaction constant. In general this observation is also true in case of 1-butene.

In essence: Using gas adsorption techniques, surface-structural characteristics of a filler aggregate can be obtained. Ranging from: (i) Sub-nm informations regarding different energy-profiles of sites on the surface, (ii) geometrical roughness, i.e. the surface-fractal dimension D_S probing several nm thick layers of gas, to (iii) the volume of a mono layer V_m, and hence the specific surface area of the filler. These multi-scale, structural informations strongly influence the interaction of the filler material with polymer chains. Therefore, it is often very useful to apply polymer-analogous gases like 1-butene, propylene or ethane in addition to the standard gas nitrogen.

are close to the literature value, make it reasonable.

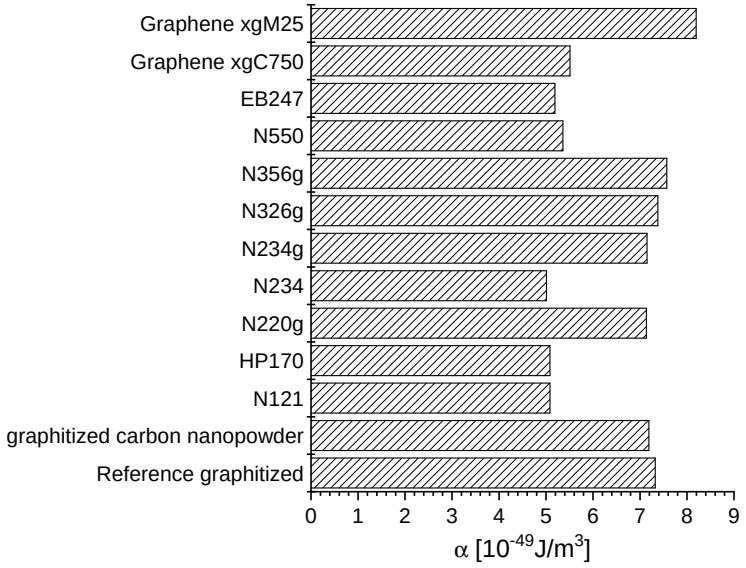

Figure 2.8.: Van-der-Waals interaction constants α for 1-butene (T=266.89 K) for various filler surfaces.

2.3. Determination of structural parameters of carbon black aggregates by TEM-image analysis

During the production process of carbon black, different processes determine the shape and structure of the final aggregates. In a carbon black reactor petroleum based products are partially combusted and from initial carbon-based seeds first particles are growing. These particles will grow in size and form the almost spherically shaped primary particles of the final carbon black. During this period of growth, they will also collide with different other primary particles and thus form small aggregates. Hence, until the final primary aggregate has reached its shape and size, always two processes occur: i) surface growth and ii) particle aggregation.[93]
With different process parameters like temperature and time, different shapes of the aggregates as well as the size of the particles can be tuned. In general, the size of these primary particles determines the specific surface area obtained via gas adsorption measurements.[22] The shape of the aggregates is often referred to as structure of the carbon black. For rubber applications the structure is a very important parameter to tune different mechanical properties of the compound.[23] Therefore, it is of importance to quantitatively characterize the structural parameters of the carbon black aggregates.

To characterize the structure of carbon black as raw powder the oil absorption number (OAN)[24] is stated. Essentially, this number measures the amount of oil, which can be absorbed by the carbon black. Thus, the DBP number as one typical structural parameter is connected to the volume of voids formed by the specific shape of the aggregates. Nevertheless, there is often not the best correlation between the DPB number and the properties of a rubber compound.[111]

[22]The smaller the diameter of the particle, the larger the specific surface area.
[23]One important example would be the energy dissipation.
[24]Or sometimes also referred to as DBP number for Dibutyl Phthalate (ASTM D2414)

One fundamental reason for this effect is the mixing process, where a lot of energy is needed to distribute the filler aggregates randomly within the polymer matrix. Additionally to this change in filler-structure caused by mechanical incorporation, the polymer-filler interaction causes different flocculation effects (see section 2.4.2). Thus, the filler structure after mixing as well as after curing might have very different characteristics as the original raw material.[64] In order to take these structural changes of the filler into account, it is needed to find an alternative method of characterization.

Since Mandelbrot first introduced the concept of fractals in the 70s [51] and applied it to natural phenomena [52], such a characterization method is available. The fundamental relation uses the scaling between the mass m of an object with its size ξ:

$$m \propto \xi^{D_f}. \tag{2.37}$$

This defines the mass fractal dimension D_f, which represents a fundamental structural parameter to compare differently shaped objects. Typical shapes like spheres or circles yield a fractal dimension of an integer value like $D_f = 3$ and $D_f = 2$ respectively. However, for so called self similar (i.e. fractal) objects, one often finds non-integer values for D_f. During typical aggregation processes, the particles can move on different paths inside the reactor chamber, which will lead to different structures of the clusters and therefore varying fractal dimensions. If the particles only move on a random-walk-trajectory, the resulting cluster has a fractal dimension of $D_f = 1.8$.[93] This regime is referred to as diffusion limited cluster aggregation (DLCA). A second typical regime is the ballistic cluster aggregation, where the particles are mainly moving on linear trajectories before hitting each other and form a cluster with a fractal dimension $D_f = 1.9-1.95$.[93] If chemical reactions occur between the particles, moving on random walk trajectories, the clusters will have typically a higher fractal exponent of $D_f = 2.1$.[112] Under the high temperature conditions in a carbon black reactor, the surface growth and aggregation process will mainly happen under ballistic conditions.[93]

One possible way to access the fractal structure of filler aggregates - in the dry as well as in the in-rubber state - is to use the transmission electron microscope (TEM) [53, 113, 114] or [44]. With this technique, a very high spatial resolution can be obtained.[25] Due to the principle of measuring only a transmission signal, the samples need to be very thin.[26] The complex 3-dimensional shape and structure of filler aggregates is therefore only visible as its 2-dimensional projection. To nevertheless be able to extract informations about the 3-d volume of the aggregate, two different methods are discussed in this work. In 1989 Meakin et al. carried out different computer simulations of aggregation processes and found the following relation between the number of particles $N_P \propto m$ in the 3-d cluster and the cross-sectional area A_S observed in 2-d TEM images:[117]

$$N_P = 1.51 \left(\frac{A_S}{A_P} \right)^{1.08}. \tag{2.38}$$

A_P is the area of a single particle[27] and the two numerical parameters are fitting parameters to

[25] From 0.5 Å up to several μm [115, 116]

[26] Typically in the range of 30 nm to 100 nm

[27] Since in log-scale this parameter would just cause a shift in the vertical direction, it is henceforth set to unity for simplicity.

simulation results.[28] From purely geometrical arguments one can find the relation:

$$V_A = \frac{8}{3}\frac{A_S^2}{P} \tag{2.39}$$

between the cross-sectional area A_S and the volume of the aggregate V_A, with P as the perimeter of the cross-section. This relation is exact for a sphere and was proposed by Herd et al. in 1993 to be used in the context of TEM image-based fractal analysis.[53] Consequently, the more the cluster differs from the perfectly spherical shape, the bigger the error of equation (2.39) gets.
Regardless of which method is used to estimate the mass of an aggregate, the fractal dimension is obtained by plotting the mass m versus the size ξ in a double logarithmic plot.[29] Additionally to this mass-size scaling-relation to obtain the fractal dimension, there is the possibility to evaluate the solid volume fraction Φ_A of the aggregates as a function of their respective size ξ. Φ_A is defined as the ratio between the estimated volume of a cluster and the volume of the sphere around this aggregate:

$$\Phi_A = \frac{V_A}{V_{sphere}(\xi)} = \frac{V_A}{\frac{4}{3}\pi\xi^3}. \tag{2.40}$$

From equations (2.37) and (2.40) it is obvious that the expected scaling of the volume fraction is $\Phi_A \propto D_f - 3$. This structural information becomes important when Φ_A deviates significantly from the spherical limit of $\Phi_A = 1$. In case these high structured aggregates are mixed into polymers, the structure leads to occluded rubber effects[30] and the volume fraction of filler Φ becomes an effective volume fraction:

$$\Phi_{eff} = \frac{\Phi}{\langle \Phi_A \rangle}, \tag{2.41}$$

with $\langle \Phi_A \rangle$ as the second moment of the distribution for Φ_A.[31]

2.4. Polymer-filler interaction: Reinforcement of elastomers by nano-fillers

In the first section of this chapter, some characteristics of polymers were discussed and subsequently the characterization of fillers was introduced on three different length-scales.[32] In the following section, the characteristics of connecting these different species, i.e. polymers and fillers, into a filled elastomer is discussed.[42, 44, 69, 93]

[28] Equation (2.38) is a simple power law valid within 10 % accuracy; It is representing an ideal gas approximation in the limit of perfectly spherical particles ($7 < N_P < 2500$) assuming only ballistic aggregation. More general simulations yield a more complex relation between N_P and A_S: $A_S = 0.278 N_P^{0.969} + 0.517 N_P^{0.833}$

[29] By applying eq. (2.37) with a linear fit.

[30] Polymer is concealed inside voids, formed by the structure and therefore it is mechanically not deformable as the rest of the polymer, hence is acting like additional filler.

[31] With the second moment a weighting of the number Φ_A with the cluster-size ξ is performed.

[32] (i) The smallest length-scale is dominated by the energetic heterogeneity of the surface (sub-nm regime); (ii) Next is the $1 - 10$ nm scale observable in the surface roughness of the aggregates; and (iii) The largest length-scale of several $10 - 100$ nm was investigated via the TEM image-analysis and is connected to the structure of filler aggregates.

2.4.1. Hydrodynamic reinforcement of elastomers

Introducing hard (non-elastic), spherical particles into a soft matrix yields an elastic reinforcement. This effect was first observed by Einstein in 1906 [39] for the change in viscosity of different suspensions. In 1944 Smallwood showed, that the same concept is true for rubber by adding randomly dispersed filler particles. [40] The change in modulus G is expressed in the form

$$G = G_{matrix}\left(1 + 2.5\,\Phi\right), \tag{2.42}$$

often referred to as Einstein-Smallwood equation. There are three physical conditions for the validity of equation (2.42): (i) randomly, freely dispersed particles (therefore only at low volume fractions Φ), (ii) spherical shaped particles (hence the factor 2.5) and (iii) infinitely stiff filler particles (non-elastic).
Vilgis et al. discussed several other more physically realistic models to take into account the fractal nature of typical carbon black aggregates (see section 2.3). One result for fractal aggregates shall be mentioned here:

$$\frac{G - G_{matrix}}{G_{matrix}} \propto \begin{cases} R^{0.1}\,\Phi & \text{for } \Phi < \Phi_{crit} \quad \text{(a)} \\ R\,\Phi^{1.8} & \text{for } \Phi > \Phi_{crit} \quad \text{(b).} \end{cases} \tag{2.43}$$

With $\Phi_{crit} = (R/b)^{1.1}$ the critical overlap volume fraction of the structured filler aggregates.[33][93] Interestingly, equation (2.42) is still valid for small enough volume fractions. Nevertheless, in typical application in rubber-technology the used filler amount is usually higher than the percolation threshold Φ_C, which separates the regime of purely hydrodynamic reinforcement and the one where a thoroughgoing filler network is formed.

2.4.2. Filler network effect: Flocculation and non-linear dynamic strain response

In the previous sections filler aggregates were only acting as hydrodynamic reinforcement because either the filler volume fraction is lower than the gel point concentration $\Phi < \Phi^*$ [44] or the filler network already broke down due to high strain amplitudes. In this subsection, first the build-up of a filler network is briefly discussed, followed by the non-linear softening apparent at medium to high strain amplitudes.

Build-up of a filler network structure: Flocculation

Flocculation by definition of IUPAC (International Union of Pure and Applied Chemistry) is "a process of contact and adhesion whereby the particles of a dispersion form larger-size clusters."[118] Flocculation in filled elastomers though is not straight forward obeying this definition. That is due to the high viscosity of the surrounding polymer matrix, where a long-range cluster forming aggregation process is usually strongly suppressed. In fact, the filler aggregates

[33] R is th spatial size of an aggregate and b the primary particle size.

within a highly entangled polymer matrix will only fluctuate around their average position with a range of the order of the entanglement length.[34] [11]
With this assumption, it becomes reasonable to look only at high enough filled systems $\Phi > \Phi^+$ and $\Phi > \Phi^*$[35], where the mean cluster trajectory to aggregate with another cluster is smaller than the fluctuation range.[44] What is typically observed in time-dependent rheological experiments (often referred to as flocculation experiments) at elevated temperatures (see 4.3) is an increase in modulus with time.[119] This is indicating a structural change of the filler aggregates until a network is formed. In general, filler clusters will move randomly within a certain volume defined by their fluctuation range. However, in the vicinity of other clusters the movement becomes directed towards each other caused by entropic depletion forces.
Depletion forces are often observed in colloidal polymer systems [120] or fluids [121]. The underlying mechanism is explained easiest at a binary mixture of big and small spheres. If the two big spheres approach a critical distance to each other,[36] the big spheres feel an attractive force towards each other. This force is caused by an effective pressure due to small spheres hitting against the big sphere. Below the critical distance, the pressure from the volume between the big spheres becomes smaller than the pressure from all other directions, hence there is a resulting net force towards each other.[37] Although, in a filled elastomer the actual mechanism driving the flocculation will be more complicated, it is still more likely to find an depletion-force-related mechanism than any other forces between the particles.[38] Additionally to the depletion force, the interaction strength between the polymer chains and the filler surface influences the flocculation behaviour.
In section 2.2 it was shown, that there is a constant adsorption and desorption of gas molecules on the filler surface. It is very likely to expect the same behaviour for segments of polymer chains. Thus, there will be a layer of adsorbed polymer around the filler surface, which will only disappear at very high temperatures. The existence of this layer is heavily discussed in the literature because in simulations and some experiments there are indications, whereas in some other experiments there is no layer visible. Some examples of literature regarding the immobilized (sometimes also referred to as glassy or glassy-like) layer are for instance: [123–125] or [44] and references therein.
While the cluster is moving towards the nearest neighbour, the two polymer layers will overlap and a new filler-filler bond will be established. The strength of this polymer bridge is depending on several parameters: (i) Polymer-filler interaction, (ii) temperature and (iii) molecular weight and entanglement density of the polymer chains. A strong or weak polymer-filler interaction will lead to a different layer thickness around the particles. If there is only a weak interaction, there will be less polymer bound onto the surface, hence there will be a smaller resulting gap (i.e. bridge between the clusters) because it is easier to press the polymer away while approaching each other.[39] This results in an overall stiffer filler network structure, which is also observed

[34] Typical values are in the order of several nm
[35] Φ^+ is the aggregation limit filler concentration, where there is still no filler network, but single particles will start to flocculate to form bigger structures, which are still all separated; Φ^* is the gelation point of the filler network, where the mean trajectory is small and the cluster size is only governed by the empty space.
[36] In the order of the size of the small spheres.
[37] The basics of depletion interaction can be found here [122]
[38] All other forces between the particles are of too short interaction range.
[39] Whereas the opposite is true for strong polymer-filler interaction: There will be a thicker layer around the particles, hence there will be a wider gap due to more resistance of the polymer while approaching.

in experiments [44].
Therefore, flocculation experiments are often very helpful to elucidate the fundamental mechanisms of the polymer-filler interaction especially in comparing different (polymer- and/or filler-) systems. Nevertheless, it is often valuable to have, additionally, a complementary analysis for the respective systems. Since investigating the build-up of a filler network comprises valuable informations, it is worth evaluating the corresponding break-down of it as well.

Non-linear strain response under dynamic loading: Payne effect

In the famous work of Payne from 1962 [32] he investigated the softening of filled rubber with increasing dynamic strain amplitude, often referred to as Payne effect. A few years later Kraus [60] found an empirical relation to describe this softening with a simple phenomenological model.[40]
The work of Kraus [60] and later the one from Maier & Göritz [61] in particular show strong similarities in the phenomenological description of the Payne effect in their respective models. In this section there will be a brief derivation of these phenomenological models, because there are interesting similarities in the derivation of both models and the Langmuir model of adsorption [96] (see section 2.2.1).

Maier & Göritz model of variable network density: The main assumption of this model is that the softening is caused by a change in local cross-link density due to chain slippage from the filler surface as a response to strain and/or temperature changes. Accordingly, there are two possible states for a chain segment to be in. State 0: The chain is physically attached (adsorbed) to the surface, hence is strongly bound; and state 1: Due to slippage, the chain segment is only weakly coupled to the surface (desorbed).[41] Defining the (molar) fractions of segments in the two states to be θ_0 and θ_1 respectively, one can write

$$\theta_0 + \theta_1 = 1. \tag{2.44}$$

There is a certain probability $p_{0\to1}$, that chain segments get detached and with $p_{1\to0}$ get adsorbed again[42]. Assuming equilibrium conditions the following balance equation is valid

$$\frac{\theta_1}{\theta_0} = \frac{p_{0\to1}}{p_{1\to0}}. \tag{2.45}$$

Using the definition $\chi \equiv \frac{p_{0\to1}}{p_{1\to0}}$ together with (2.44) and (2.45) this leads to:

$$\theta_0 = \frac{1}{1+\chi}, \tag{2.46}$$

$$\theta_1 = \frac{\chi}{1+\chi} \tag{2.47}$$

[40] Often referred to as Kraus model
[41] The indices 0 and 1 are chosen according to the nomenclature in section 2.2.1
[42] In analogy to a rate of desorption and adsorption respectively

and finally

$$\theta_0\theta_1 = \frac{\chi}{(1+\chi)^2}. \tag{2.48}$$

The ratio between the two rates of adsorption and desorption χ is assumed to depend on the dynamic amplitude γ

$$\chi = \frac{\gamma}{\gamma_0} \tag{2.49}$$

with γ_0 as a material dependent, empirical parameter.[43] Equation (2.47), describing the number of chain segments, which get detached with increasing strain amplitude γ, does look like the Langmuir isotherm equation (2.19) with $b_L = 1/\gamma_0$.[44]
With respect to the storage- and loss modulus $G'(\gamma)$ and $G''(\gamma)$, there are two explicit assumptions in the model of Maier and Göritz. While the former is proportional to the number of still attached chain segments $\theta_0 \propto G'(\gamma) - G'(\infty)$ (see equation (2.46)), the latter is proportional to the product $\theta_0\theta_1 \propto G''(\gamma)$ of both numbers (see equation (2.48)). The term $G'(\infty)$ represents the modulus at the limiting case when all chain segments are detached.

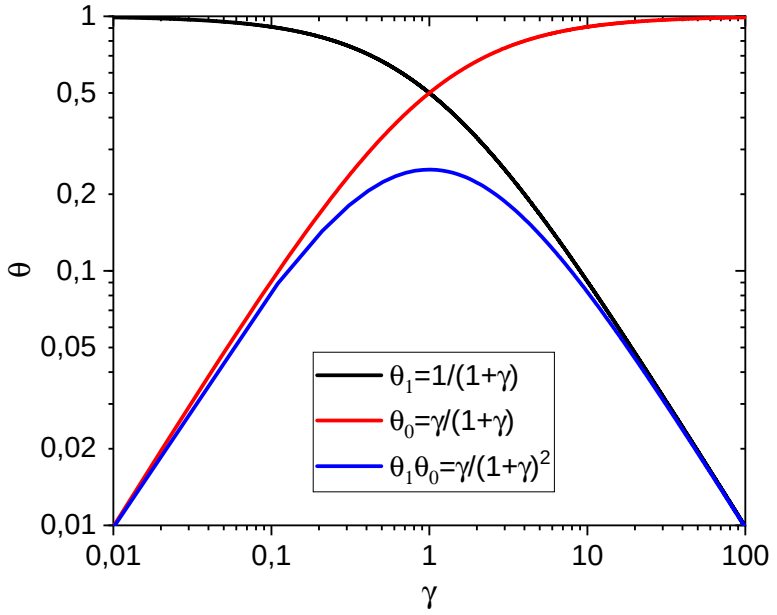

Figure 2.9.: Illustration of the trend for chain segments in different states as a function of strain amplitude γ. Note that θ_1 is essentially showing the same behaviour as the Langmuir model for a gas adsorption isotherm (Then γ has to be replaced by the pressure p; omitting any pre-factors).

$$G'(\gamma) - G'(\infty) = \frac{G'(0) - G'(\infty)}{1 + \frac{\gamma}{\gamma_0}} \tag{2.50}$$

[43] Which needs to be fitted to real test data to obtain a reasonable value.
[44] The number of gas molecules adsorbed to a surface increase with increasing pressure p in the same way as the number of detached chain segments θ_1 is increasing with higher strain amplitudes γ (see θ_1 in figure 2.9).

and

$$G''(\gamma) = \frac{\frac{1}{4} G''_{max} \frac{\gamma}{\gamma_0}}{\left(1 + \frac{\gamma}{\gamma_0}\right)^2}. \tag{2.51}$$

As interesting as the idea of a locally changing network density seems,[45] the fact that there is no consideration of a filler network at all, rules out the Maier & Göritz model as explanation for the Payne effect. This statement will be discussed and proven in chapter 4, where results of certain strain dependent measurements will be presented.

Kraus model: In contrast to the above discussed model from Maier and Göritz, the Kraus model takes into account the filler network as main contributor to the changes in the respective moduli under dynamic deformations. Mainly Kraus assumes two different processes happening during deformation: i) deagglomeration (breakdown) and ii) reagglomeration of filler clusters. Furthermore, there are $N = N_0 + N_1$ number of contacts in the filler network, with N_0 (still remaining) and N_1 (already) broken contacts.
Accordingly, there is a rate of deagglomeration k_b and reagglomeration k_a, which in equilibrium have to be equal. The process of breaking down the agglomerates is set to be proportional to the fraction of remaining contacts $\frac{N_0}{N} = n_0$ and to the deformation (to the power m) γ^m. For the reagglomeration process it is assumed that it depends on the portion of broken contacts $\frac{N_1}{N} = n_1 = 1 - n_0$ as well as inversely on the deformation γ^{-m}.[46] Putting these assumptions together this yields

$$k_b = \kappa_b n_0 \gamma^m, \tag{2.52}$$

$$k_a = \kappa_a n_1 \gamma^{-m} = \kappa_a \left(1 - n_0\right) \gamma^{-m} \tag{2.53}$$

now assuming equilibrium conditions $k_a = k_b$

$$n_0 = \frac{1}{1 + \left(\frac{\gamma}{\gamma_0}\right)^{2m}} \tag{2.54}$$

$$n_1 = 1 - n_0 = \frac{\left(\frac{\gamma}{\gamma_0}\right)^{2m}}{1 + \left(\frac{\gamma}{\gamma_0}\right)^{2m}} \tag{2.55}$$

using the characteristic ratio of rate constants $\gamma_0 = \left(\frac{\kappa_a}{\kappa_b}\right)^{1/2m}$. The obvious mathematical difference to the Maier & Göritz model is the power m. For the moduli the following assumptions

[45] In fact there is little knowledge about the local change in network density in the presence of filler particles.
[46] This assumption is completely arbitrary but even if there was a different scaling, the overall quality of the fit to experimental data would not significantly be increased.

are made:

$$G'(\gamma) - G'(\infty) \propto n_0 \tag{2.56}$$

$$\Rightarrow G'(\gamma) - G'(\infty) = \frac{G'(0) - G'(\infty)}{1 + \left(\frac{\gamma}{\gamma_0}\right)^{2m}}, \tag{2.57}$$

$$G''(\gamma) \propto k_b = \kappa_b n_0 \gamma^m = \kappa_b \frac{1}{1 + \left(\frac{\gamma}{\gamma_0}\right)^{2m}} \gamma^m \tag{2.58}$$

using $\kappa_b = \left(\frac{1}{\gamma_0}\right)^m \frac{\kappa_a}{\gamma_0^2}$ and the fact that G'' is has its maximum at $\gamma = \gamma_0$

$$\Rightarrow G''(\gamma_0) = G''_{max} = \frac{\kappa_a}{2\gamma_0^2} \tag{2.59}$$

$$G''(\gamma) = \frac{\left(\frac{\gamma}{\gamma_0}\right)^m 2G''_{max}}{1 + \left(\frac{\gamma}{\gamma_0}\right)^{2m}}. \tag{2.60}$$

Comparing the final equations for the moduli, there are differences between the two models observable. In figure 2.10 it is obvious, that the qualitative trend is very similar, but there are some deviations due to the choice of parameters ($m = 1$ as in Maier & Göritz) for the Kraus model. In general fitting the Kraus model to experimental data, usually yields values for the exponent $m \approx 0.6$ [93], which will shift the curves closer to the Maier & Göritz curves in figure 2.10. In the Kraus model the $G'(\infty)$ term has a physically more realistic meaning: Here, the filler network broke down completely and the remaining modulus is only determined by the polymer network (G_e from entanglements and G_c from cross-links) plus hydrodynamic reinforcement ($G = G(\Phi_{filler})$) effects. In chapter 4 some experimental data will show quite good agreement with these two model curves.[47] It shall be mentioned, that the parameters γ_0 and m are purely empirical and there is no deeper physical meaning behind them in these models.
Vilgis et al. tried to develop a physical model to explain the Payne effect with a more realistic assumption: Clusters, which form the filler network, have a fractal structure. Finally the resulting formulas look very much like the aforementioned of Maier & Göritz or Kraus model. An important difference is the explanation of the universality of the parameter m, which is here related to the fractal dimension d_f of the cluster and their minimum path dimension C ($m = \frac{1}{C - d_f + 2}$).[48] Putting in typical values of $d_f \approx 1.8$ and $C \approx 1.3$ one obtains $m \approx 0.66$, which is often very close to the observed value.[93]

2.4.3. Stress-softening and hysteresis for quasi-static deformations up to large strains

In the previous section the softening of filler reinforced elastomers, i.e. the Payne effect was discussed. Responsible for this effect is the breakdown of the fractal filler network into smaller

[47] Often a simultaneous fit of both datasets is recommended, because there are two common parameters γ_0 and m.
[48] C is the scaling exponent relating the geometrical distance between two points on a cluster R with the minimum path length L on it: $L \propto R^C$

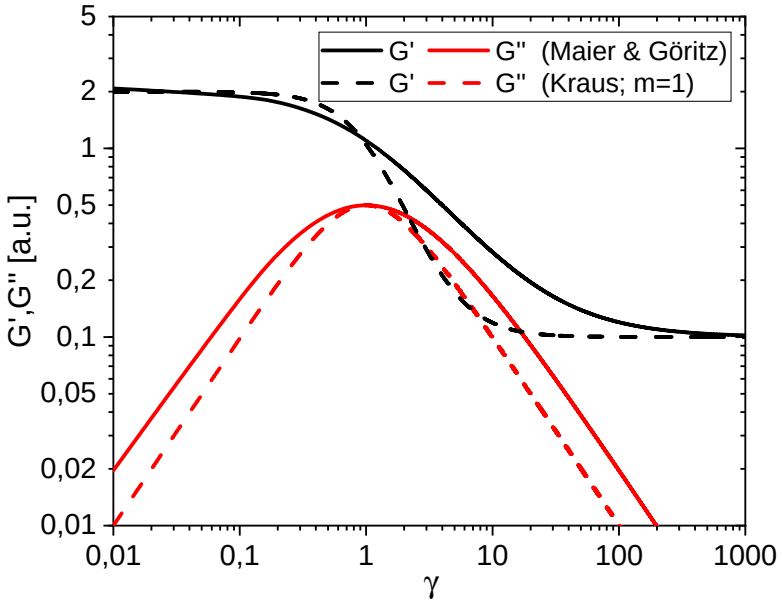

Figure 2.10.: Illustration of the trend for $G'(\gamma)$ and $G''(\gamma)$ as a function of strain amplitude γ for Kraus and Maier & Göritz model. The chosen parameters are just exemplary to show the qualitative differences between (2.50), (2.51) and (2.57), (2.60) respectively.

sub-clusters. While this effect is showing a certain dependency on frequency, which is typical for rubber-viscoelasticity, a similar effect can be observed in the limit of quasi-static deformations. For filled elastomers, often a stress-, i.e. strain- induced-softening, during cyclic deformations, often also referred to as Mullins effect, is observed.[34, 66, 67].[49]

Klüppel and coworkers [19, 41, 42, 44, 69–73] developed a micro-mechanically based model, referred to as Dynamic Flocculation Model (DFM), capable of modelling the strain induced softening and hysteresis loops of filled elastomers. The DFM combines well established concepts of rubber elasticity with a micro-mechanical approach of dynamic filler flocculation in strained rubbers at different elongations.

In section 2.4 it was discussed that in filler reinforced elastomers the fractal filler clusters are bonded by immobilized polymer bridges. Hence, it is reasonable to connect macroscopic softening with a successive breakdown of these clusters with increasing strain amplitude. Therefore, one distinguishes between the virgin sample with non-broken, virgin filler-filler bonds and pre-strained samples with a certain amount of softer bonds.

The process of cluster breakdown begins with the largest filler clusters and continues up to a certain minimum cluster size. Upon decreasing the strain, complete re-aggregation of the filler aggregates is assumed. However, the filler-filler bonds, which are formed again after once being broken, are significantly weaker than in the virgin sample. At subsequent stress-strain cycles of a pre-strained sample, two micro-mechanical mechanisms can be distinguished. (i) Hydrodynamic reinforcement of the rubber matrix by a fraction of rigid filler aggregates with strong virgin filler-filler bonds, which have not been broken during previous deformations. (ii) Cyclic

[49] A review of the Mullins effect can be found here: [68]

breakdown and re-aggregation of the remaining fraction of softer filler clusters with damaged and thus weaker filler-filler bonds.
The fraction of rigid (unbroken), i.e. still virgin, filler clusters decreases with increasing strain, while the fraction of soft filler-agglomerates increases. The mechanical action of the soft filler clusters refers primarily to a viscoelastic effect, since any type of cluster that is stretched in the stress field of the rubber stores energy that is dissipated when the cluster breaks. This mechanism leads to a filler-induced viscoelastic hysteresis contribution to the total stress, which significantly affects the internal friction of the filled rubber samples. Accordingly, the apparent stress resulting in the DFM consists of two contributions: (i) the stress of the rubber matrix including hydrodynamic reinforcement, and (ii) the stress of the strained and broken filler clusters. The free energy density of filler reinforced rubber is given by:

$$W\left(\epsilon_\mu\right) = \left(1 - \Phi_{eff}\right) W_R\left(\epsilon_\mu\right) + \Phi_{\mathbf{eff}} W_A\left(\epsilon_\mu\right) \tag{2.61}$$

with Φ_{eff} being the effective filler volume fraction of the structured filler particles, e. g. primary carbon black aggregates (see section 2.3). The first addend considers the equilibrium energy density stored in the strained rubber matrix, which includes hydrodynamic strain amplification effects varying with the fraction of relatively stiff filler clusters with strong virgin filler-filler bonds. The second addend considers the energy stored in the residual fraction of more soft filler clusters with damaged bonds that are deformed in the stress field of the rubber matrix. The free energy density of the strained rubber matrix W_R is described by the extended non-affine tube model of rubber elasticity (2.11). The second addend takes into account the energy stored in strongly strained soft filler clusters:

$$W_A(\epsilon) = \sum_{\mu}^{\dot{\epsilon}_\mu<0} \frac{1}{2d} \int_{\xi_{\mu,min}}^{\xi_\mu(\epsilon_\mu)} G_A(\xi_\mu^{'}) \epsilon_{A,\mu}^2(\xi_\mu^{'}, \epsilon_\mu) \Phi(\xi_\mu^{'}) \mathrm{d}\xi_\mu^{'}. \tag{2.62}$$

Here, d is the particle size and ξ_μ denotes the cluster size in the spatial direction μ. The cluster size distribution $\Phi(\xi_\mu)$ is considered to be isotropic.[50] Accordingly, for the soft filler clusters, ϵ_μ and G_A denote the strain and the elastic modulus. The upper limit of the sum in (2.62) takes into account that breaking of clusters will only take place in the direction of stretching, hence healing of them will only occur in the perpendicular direction. The integration is performed over the fraction of soft clusters of size $\xi_{\mu,min} < \xi_{mu} < \xi_\mu(\epsilon_\mu)$, which are not broken at the actual cycle.
There is no contribution of the rigid filler clusters to the stored energy W_A. Mechanically they act via local over-stretching of the rubber matrix, which is quantified by a strain amplification factor X, relating internal and external strains λ_μ and ϵ_μ respectively:

$$\lambda_\mu = 1 + X\epsilon_\mu. \tag{2.63}$$

For pre-strained samples the value of X depends on the maximal strain $\epsilon_{\mu,max}$. Huber and Vilgis [126, 127] tried to derive an expression for the amplification factor in the case of overlapping fractal clusters:

$$X(\epsilon_{\mu,max}) = 1 + c\Phi_{eff}^{\frac{2}{3-d_f}} \sum_{\mu=1}^{3} \frac{1}{d} \left\{ \int_0^{\xi_{\mu,min}} \left(\frac{\xi_\mu^{'}}{d}\right)^{d_w - d_f} \Phi(\xi_\mu^{'}) \mathrm{d}\xi_\mu^{'} + \int_{\xi_{\mu,min}}^{\infty} \Phi(\xi_\mu^{'}) \mathrm{d}\xi_\mu^{'} \right\}. \tag{2.64}$$

[50] Hence: $\Phi(\xi_1) = \Phi(\xi_2) = \Phi(\xi_3)$

Here, c is a constant of order one, d_f is the fractal dimension and $d_w = 2d_f/D$ is the anomalous diffusion exponent on fractal clusters. Essentially all parameters of the model, needed to describe experimental results, have been mentioned until now. First there are 3 fit-parameters describing the polymer network: G_e, G_c and $n = n_e/T_e$, then there is the effective filler volume fraction Φ_{eff} and the average cluster size x_0.[51] Furthermore, there are two additional unknown factors, namely the two integration limits of (2.62) and (2.64) respectively. A detailed derivation will not be shown here (see e.g. [44]), but as a result one obtains two different ultimate yield-stresses for the bonds of soft clusters s_d and the virgin clusters s_v.[52]

In essence: Understanding the behaviour of nano-filler-reinforced elastomer composites essentially is about getting insights of the polymer-filler interaction. Hence, it is crucial to characterize on the one hand the interface, viz., the filler-surface (see section 2.2). On the other hand, the inter-phase, i.e. the volume in the vicinity of the interface, is important to analyse. In the previous section, the most important models and basic concepts were briefly discussed. This leads to the mesoscopic picture of polymer-mediated filler-filler bonds, responsible for connecting filler clusters to form a reinforcing fractal network, which undergoes structural changes in the course of deformations.

In the following chapters experimental techniques are explained and results are presented. The theoretical concepts elucidated in this chapter will help in understanding and explaining the results.

[51] As one unknown parameter of the cluster-size distribution $\Phi(\xi)$, hence it needs to be fitted to experimental data to get a value.

[52] The limit of the first integral in (2.62) is related to s_d via: $\xi_\mu(\epsilon_\mu) = \frac{s_d}{\hat{\sigma}_{R,\mu(\epsilon_\mu)}}$ and to s_v via: $\xi_{\mu,min} = \frac{s_v}{\hat{\sigma}_{R,\mu(\epsilon_\mu)}}$ with $\hat{\sigma}_{R,\mu(\epsilon_\mu)} \equiv \sigma_{R,\mu}(\epsilon) - \sigma_{R,\mu}(\epsilon_{min})$ as the relative stress.

3. Experimental

In the following chapter experimental details of this work will be described. Beginning with some material related particularities, there will be a brief description of every experiment used in this work, each with the respective sample preparation and measuring principle.

3.1. Materials

Polymers of different type and characteristics have been used to investigate the influence of their chemical details on the interaction with different filler materials. The chemical structures of all polymers used in this work are shown in figure 3.1. Natural rubber (NR) is one of the most

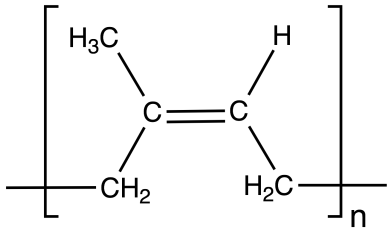

(a) Cis-1,4-polyisoprene (NR)

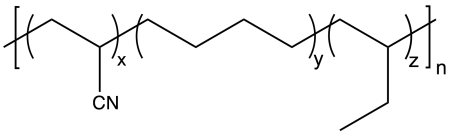

(b) Hydrogenated acrylonitrile butadiene rubber (HNBR)

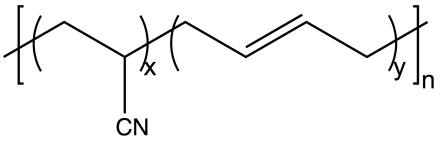

(c) Nitrile butadiene rubber (NBR)

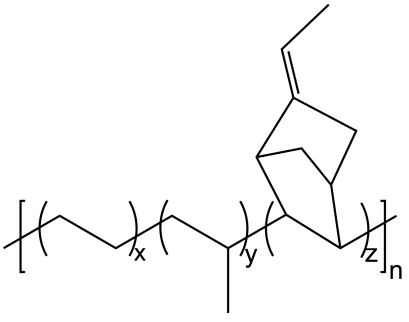

(d) Ethylene propylene diene rubber (EPDM)

Figure 3.1.: Chemical structure of all used polymer types.

widely used polymers in rubber industry. Especially in the tire industry, NR is still indispensable due to its high elastic strength at high deformations. The chemical structure is seen in 3.1a.

One of its most interesting characteristics of NR is the effect of strain-induced crystallization (SIC), which leads to a better resistance to failure and fatigue.[128]
High performance elastomers like hydrogenated acrylonitrile butadiene rubber (HNBR - figure 3.1b) and nitrile butadiene rubber (NBR - figure 3.1c) or ethylene propylene diene rubber (EPDM - figure 3.1d) are used mainly in special applications like transmission belts, seals, hoses or other parts used in the automotive industry, which require special properties like oil or heat resistance. By studying NBR and HNBR, the influence of double bonds inside the backbone of the polymer chain can be investigated. Usually the electrons of the double bond will be able to interact with the π-electrons of the graphite-crystals present on the surface of carbon black, often referred to as a π-π-stacking mechanism.
Consequently, the properties of compounds are not solely dominated by the polymer, rather they are influenced by the type of filler and the interaction between polymer and filler. In table 3.1 all used filler materials are listed, including the type of filler and the measured specific surface area, estimated using the BET method discussed in section 2.2.1. A first type of carbon-based fillers are graphites, which usually show a very homogeneous surface. Similarly the graphitized carbon blacks show the same feature. They are produced when carbon blacks are applied to a heat treatment of about $3000\,K$ under nitrogen atmosphere for several hours. Additionally to the usual carbon blacks, more recently investigated types of reinforcing fillers are graphenes and carbon nano-tubes (CNT). Their special structures and characteristics are a very recent topic in rubber technology (see for CNT studies e.g. [36, 129, 130] and for graphenes [131–134]).
All carbon blacks as well as the graphitized CB were produced by Orion Engineered Carbon GmbH. Graphenes, more specifically graphene-nano-platelets (GnP) were mainly provided from XG Science. Carbon nano tubes (CNT) have been provided by Nanocyl and Bayer AG respectively. The polymers used in this work were all distributed from Lanxess. For the filler modification the ionic liquid 1-allyl-3-methyl-imidazolium chloride (AMIC), purchased from Sigma Aldrich, was used (see figure 3.2 for the chemical structure). In section 4.3.1 there will be more details about why and how AMIC was used as surface modifying agent.

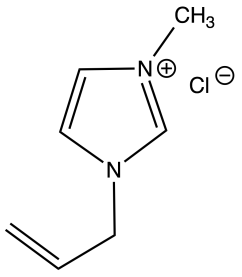

Figure 3.2.: Chemical structure of the ionic liquid 1-allyl-3-methyl-imidazolium chloride (AMIC).

Table 3.1.: List of all measured carbon black-based filler materials by name, type and measured specific BET-surface area for four different gases.

Material		**BET-surface area** $[m^2/g]$			
Name	**Type**	**Nitrogen**	**1-Butene**	**Propene**	**Ethane**
Reference	Graphite	53	50	-	60
UF 198C	Graphite	23	14	-	-
SGB10L	Graphite	11	-	-	-
SGA10M	Graphite	7	-	-	-
EDM	Graphite	8	-	-	-
Printex 60g	Graphitized CB	76	68	-	-
N220g	Graph. CB	84	72	-	-
N234g	Graph. CB	95	79	-	-
N326g	Graph. CB	77	57	-	-
N356g	Graph. CB	-	67	-	-
N121	Standard CB	118	89	-	-
N220	CB	108	-	-	-
N231	CB	-	86	-	-
N234	CB	113	87	92	-
N326	CB	75	65	-	-
N330	CB	73	-	-	-
N339	CB	83	65	67	67
N347	CB	81		-	-
N550	CB	38	29	32	33
N660	CB	36	-	-	-
N774	CB	27	-	-	-
N990	CB	8	-	-	-
Ecorax S247	CB	41	30	33	34
HP170S	CB	210	163	168	-
Printex XE2	CB	1024	-	-	-
xgC750	Graphene	803	519	-	-
xgM5	Graphene-nano-Platelet	166	101	-	-
xgM15	GnP	103	-	-	-
xgM25	GnP	227	132	-	-
NanoG	GnP	361	277	-	-
NC7000	Carbon-Nano-Tube	276	221	-	-
NC3100	CNT	252	-	-	-
BTC70P	CNT	140	-	-	-
BTC150	CNT	199	-	-	-
CNH	Carbon Nano Horns	295	239	-	-

3.2. Static gas adsorption measurements

All adsorption experiments have been carried out on a BELSorp max from BEL Japan, Inc. (now MicrotracBEL Corp.), purchased from Rubotherm GmbH (Depicted in figure 3.3). Additional to the device itself, there was a cooling unit Julabo F81-HL to set the temperature.

Figure 3.3.: Picture of the BELSorp max volumetric, static gas adsorption apparatus located in DIK Hannover.

Pretreatment:
Before the actual measurement, the sample needs to by pretreated at elevated temperatures. This is usually done at 305 °C for about 3 hours in a vacuum after flushing the samples with helium. This is needed to get rid of disturbing surface impurities like water or any other residual from the production process. However, for surface modified samples or non-carbon-based fillers such as silica, lower temperatures ~ 100°C are required to keep the actual structures on the surface. After this heating step, the samples are weighted and the measurement starts with several hours of evacuating the sample-tubes to reach a very low starting pressure ($p/p_0 < 10^{-6}$).[1]

Measuring principle:
First, gas is applied into a precisely defined volume inside the machine. Within the machine, the temperature is kept constant at 40 °C to avoid any unwanted condensation of gas molecules onto the inner surface of the apparatus. After closing the valve to the gas reservoir (see V2 in the top left part of figure 3.4), the pressure within the volume is measured. After this step, the valve to the sample tube (see V9 in the example depicted in figure 3.4) is opened, hence gas molecules will move into the sample tube. With measuring the increase in pressure while the gas is applied, the desired amount of gas is controlled. When the desired volume of gas has been applied, the valve is closed again. After closing the valve, a drop in pressure with time is apparent (see the white and red lines indicated at the lower part of figure 3.4) due to gas molecules being adsorbed onto the surface. After a certain time, the pressure reaches a constant value, thus the equilibrium between adsorption- and desorption-rate has been reached

[1] Usually this pre-measurement evacuation has been done for at least 12 hours of constant evacuation with leakage tests every 90 minutes until the desired leakage rate was reached ($\sim 10^{-3} Pa/min$)

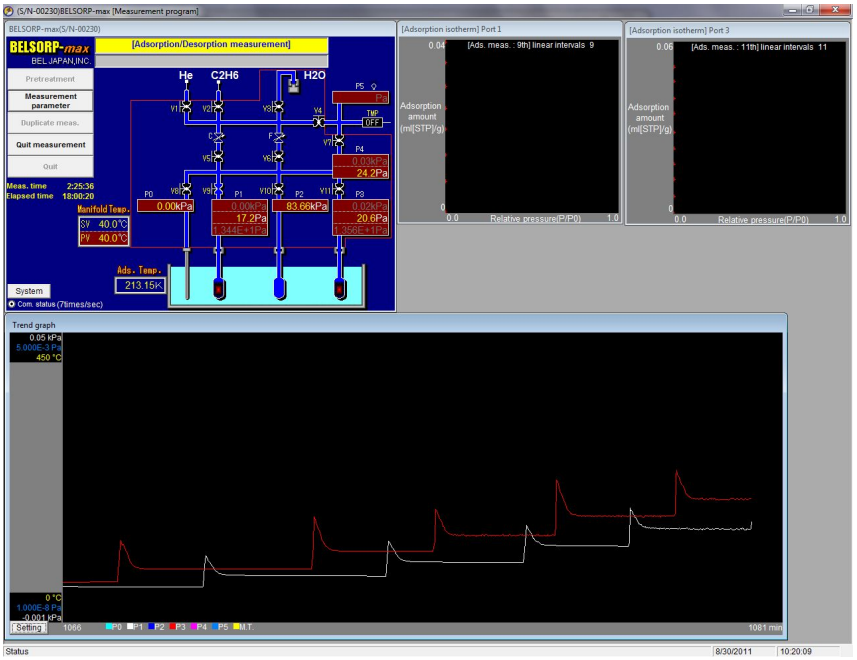

Figure 3.4.: Illustration of the measuring principle of the BELSorp max. In the top left corner, there is a schematic overview of the insights of the machine. On the bottom there is some information about the pressure measured as a function of time and on the top right corner the adsorption data points are shown.

(see subsection 2.2.1). From the corresponding drop in pressure, the amount of gas adsorbed on the surface, is estimated and the result is plotted at the corresponding pressure value in an adsorption isotherm (see upper right part of figure 3.4).

Temperature control:
In case of nitrogen adsorption the temperature is fixed at liquid nitrogen temperature $T = 77K$. For this purpose, a dewar was filled with liquid nitrogen and the samples were immersed into it. Due to evaporation of liquid nitrogen with time, the level will drop with time. To compensate for this effect, the amount of dead volume is measured at each time via the third measurement port (see the centred of three ports in the scheme on the upper left side in figure 3.4, where the samples are dipped in the temperature bath), which is always only filled with gas.[2] Another possibility to increase the reproducibility of the test data, is the measurement of the saturation vapour pressure p_0, rather than just use the literature value at the specific measurement temperature. Here, this opportunity was not used, due to minor influence on the quality of repeated measurements.
For other gases, the cooling unit has to be used. As cooling-medium inside the device, a silicon oil, which could cover a broad temperature range between -60°C and +60°C was used. Due to the pressure limit of the BELSorp max of 1300 mbar, the temperature was usually chosen, such that the saturation vapour pressure p_0 of the respective gas is approximately 1 bar. Consequently, the isotherm will not reach the point $p/p_0 = 1$ at higher temperatures, hence the multi layer adsorption is incomplete.

[2]Nitrogen will be flushed into the dead volume tube at the beginning of the measurement, the valve V10 will be closed and with the change in pressure, the drop in nitrogen is corrected.

Gas types:
Additionally to the aforementioned nitrogen, five other gases have been used: Ethane, ethene, propene, iso-butene and 1-butene. Nitrogen is one of the standard gases used for performing BET adsorption to obtain the specific surface area. However, to characterize filler materials, which are used in rubber applications, polymer analogous gases should be used to mimic the adsorption of monomers onto the surface of the filler. Apparently, all used gases are non-polar (see figure 3.5), hence only the dispersive part of the surface area can be investigated. To obtain the complete information, polar gases are additionally necessary, e.g. carbon dioxide.

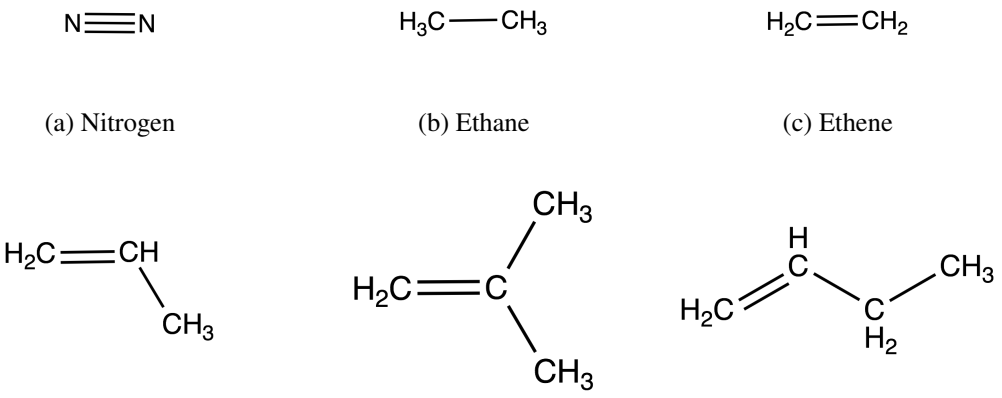

(a) Nitrogen (b) Ethane (c) Ethene

(d) Propene (e) Isobutene (f) 1-Butene

Figure 3.5.: Chemical structure of all used adsorption gases.

3.3. Sample preparation

3.3.1. Compounding

Mixing:
All master batches (compounds without curing system) were mixed on an internal laboratory mixer from Polylab with a chamber volume of 350 ml. The curing system was mixed on a laboratory two-roll mill from Berstorff with 150 mm roll diameter and 350 mm length in a second step. For higher filled compounds ($\phi_{filler} > 40phr$ with phr as per hundred rubber) the filler was incorporated in at least two (or more) steps to avoid reaching a torque limit and too high mixing temperatures.
Curing:
Before the curing of the samples can be performed, the vulcanization kinetics, i.e. the cuing time at 90 % of cross-linking needs to be obtained (often referred to as t_{90} time). This intermediate step was done either on a Moving Die Rheometer (MDR) 2000 or a Rubber Proces Analyzer (RPA) 2000 from Alpha Technologies. After the curing parameters have been obtained, the final mix was cured in a vulcanisation press from Wickert & Söhne or from Rucks Machinenbau KV 207.00. The specific conditions are shown in the respective recipe tables in the following paragraph.
Recipes:
All mixing recipes include a masterbatch, where only the polymer, the filler and typically some processing aids like zinc oxide and stearic acid have been used. The cross-linking system was usually mixed-in separately as a final step. Here, usually sulphur or peroxides were used (in case of NR and EPDM sulphur was used, for HNBR and NBR a peroxide was used). NBR and HNBR with similar acrylonitrile content (39 %) were chosen for better comparability. In the tables 3.2,3.3 and 3.4 the detailed recipes are reported.

Table 3.2.: Recipe of natural rubber compounds. N-Cyclohexyl-2-benzothiazole sulfenamide (CBS) was used as accelerator. The filler material N339 (see also table 3.1) was used with and without surface modification with AMIC (with a ratio of AMIC:Filler of 1:50; see figure 3.2).

NR compounds	
Step 1 – Internal mixer	
Ingredient	**per hundred rubber – phr**
NR - Pale Crepe	100
N339 (± AMIC)	20-70
Stearic acid	1
Zinc oxide	3
Step 2 – Two roll mill	
CBS	2.5
Sulphur	1.7
Curing @ 150 °C for t_{90} + 1 min. × sample thickness [mm]	

Table 3.3.: Recipe of EPDM compounds. Accelerators: 2-Mercaptobenzothiazole (MBT), tetrabenzylthiuram disulfide (TBzTD) and TP/S (Composition of 67 % zinc-dithionate and 33 % silica)

EPDM compounds	
Step 1 – Internal mixer	
Ingredient	**per hundred rubber – phr**
EPDM - Buna EP G 3440	100
N550/S247/N339 (± AMIC)	20-70
Stearic acid	2
Zinc oxide	5
Step 2 – Two roll mill	
MBT	1
Percacid TBzTD	1.2
Rhenocure TP/S	2
Sulphur	0.75
Curing @ 180 °C for t_{90} + 1 min. × sample thickness [mm]	

Table 3.4.: Recipe of HNBR and NBR compounds. Stabilizer: 4-(1-phenylethyl)-N-[4-(1-phenylethyl)phenyl]aniline (DDA) and 2-Mercapto 4 (5)-Methylbenzimidazole (ZMB-2); Cross-linking agent: Triallyl isocyanurate (Perkalink 301) and Di(tert-butylperoxyisopropyl)benzene (Perkadox 1440)

HNBR/NBR compounds	
Step 1 – Internal mixer	
Ingredient	**per hundred rubber – phr**
HNBR - Therban C3446 or NBR - Perbunan 3446	100
N550/S247/N339 ($\pm$ AMIC)	20-70
Magnesium oxide	2
Zinc oxide	2
Step 2 – Two roll mill	
Vulkanox DDA	1
ZMB2	0.4
Perkalink 301	2.5
Perkadox 1440	7
Curing @ 170 °C for t_{95} + 1 min. $\times$ sample thickness [mm]	

3.3.2. Surface modification of carbon black

The surface of carbon black is usually showing different heterogeneous structures, like defects or cavities (see figure 2.4). Hence, to see the influence of these heterogeneities a modification of the surface can be a valuable approach. In 2012 Kreyenschulte et al. investigated the effect of carbon black-surface modification by ionic liquids on the properties of filled elastomers [80]. This idea was taken up and analysed in more detail [135, 136].
Here, the modification was performed in three steps:

- First, the carbon black was mixed with ethanol, such that a suspension was obtained. The AMIC was used in the frozen state (stored in a freezer at -18°C) and therefore easy to add into the carbon black suspension in a ratio of 1 part AMIC onto 50 parts of carbon black. After this, the piston was mechanically shaken to obtain a reasonable (macroscopic) dispersion of the ionic liquid.
- To further disperse the sample and at the same time, get rid of the ethanol, the sample was put into a rotary evaporator. There, the piston was constantly rotating within a water bath of 40°C and inside the piston a pressure of ≈50 mbar was applied. After approximately 2 hours the ethanol was fully evaporated and the remaining carbon black looked already very dry.
- In the last step the carbon black was dried in an oven at 70°C and lowered pressure. After several hours the desired modified carbon black was obtained and analysed.

3.4. Combined rheological and dielectric measurements

Rheological measurements have been carried out on the rheometer Physica MCS 501S from Anton Paar using oscillatory shear deformations in a plate-plate geometry. Simultaneously to the mechanical measurement, the dielectric properties have been measured using the broadband analyser BDS 40 from Novocontrol GmbH. For non-cross-linked samples a preconditioning is required to establish a regular shape of the sample. For this purpose, the samples were pressed with medium pressure ($\sim$ 100 bar) at 70°C for about 3 hours. After this, in most cases the thickness was rather homogeneous and a disc-shaped sample could be punched out of it.
However, to be able to measure fairly well reproducible dielectric properties, the surface resistance needs to be reduced. Here, the surface was sputtered with a thin layer of gold (between 1 and 5 minutes of sputtering time was used). In figure 3.6 the schematic setup is depicted. Crucial to the quality and reliability of the experiment, is the contact between the dielectric analyser and the rotor of the rheometer. Therefore, several setups have been tested. The best results could be obtained, using a golden clip fixed on the rotor close to the sample, which was connected via a very thin silver wire with the Novocontrol analyser. It is assumed, that the influence of the wire, while performing shear deformations to the sample, is negligible.
Since various structures inside the sample act on a wide range of length-scales, the dielectric frequency was varied from 10 to 10^6 Hz. Each of this sweep took about 40 s of time, hence the mechanical tests have been adapted to this time scale to observe changes in both signals, simultaneously (the mechanical frequency of the shear deformations is set constant to 1 Hz for the whole experiment). The sample is placed within a chamber, where the temperature can be controlled between -40°Cand +200°C.

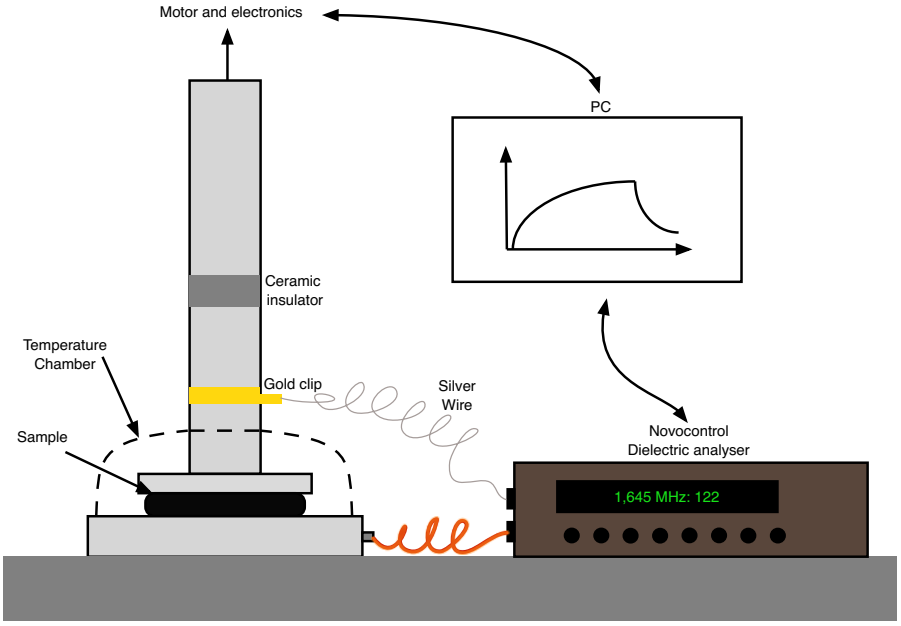

Figure 3.6.: Schematic visualization of the principle setup of the combined rheological and dielectric measurements on the Anton Paar rheometer.

3.5. Quasi-static measurements

3.5.1. Standard physical characterization

Usually all rubber compounds are characterized by standard physical properties like hardness, rebound resilience and quasi-static tensile tests. The hardness is usually measured in units of shore A [137] for typical elastomers. In a typical hardness tester, here a Zwick digitest, a metal rod with truncated 35° cone of 0.79 mm of diameter pushes with constant force into the rubber sample and after 3 seconds the penetration is reported in units of shore A.[3] Furthermore, the rebound of the samples are one important measure in rubber industry. While the hardness is correlated to the stiffness, i.e. the modulus, the rebound is connected to the energy dissipation in the material. The rebound resilience was measured with a Zwick 5109.01 device. Here, a weight is hitting the sample from a defined height and the angle after the hit is reported in relation to the starting height (usually in percent).
Another standard measurement is an uni-axial quasi-static tensile test, performed with a Zwick 1445 universal testing machine. Here, the sample is stretched with a standard speed of 200 mm/min until it breaks. From this test several important informations can be extracted, most important usually are the tensile stress and strain at break.

[3] The waiting time according to ISO is 15 s [138].

3.5.2. Cyclic Quasi-Static Uniaxial Stress-Strain Measurements

To experimentally observe the Mullins effect (see section 2.4.3) cyclic quasi-static stress strain measurements have to be performed. Here, again the Zwick 1445 was used with dumbbell-shaped samples. To see the stress softening effect, the strain needs to be increased successively. At each level of strain, 5 cycles are measured, to reach an equilibrium cycle. After the 5th cycle the strain is increased to the next higher level. In figure 3.7 a typical example of a cyclic uniaxial stress-strain plot is depicted. The testing speed is chosen at 50 mm/min, to suppress any strain-rate effects.

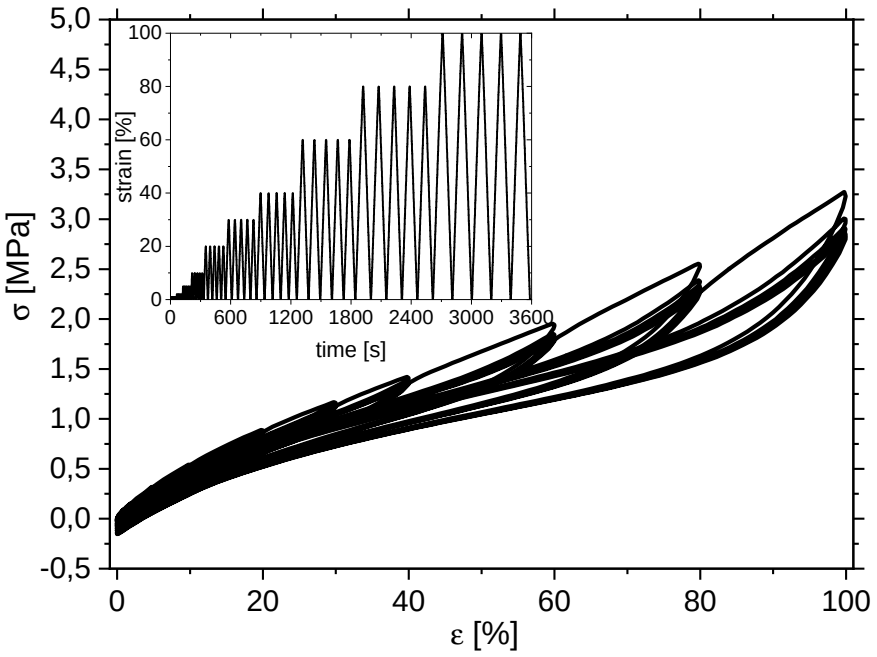

Figure 3.7.: Example of a cyclic stress-strain experiment (Data from HNBR + 50 phr N339). The inset shows the time-signal of the applied strain.

4. Results and Discussion

In the following sections, the results will be presented and discussed as a hierarchical multi-scale problem. Starting point will be the surface of filler materials as essential, fundamental cause for apparent reinforcement mechanisms in elastomer nano-composites. From sub-nm scales represented by energetically heterogeneous structures – to morphological roughness, scaling in the range of several nm, adsorption data will be utilized to elucidate the basics of all reinforcing mechanisms in nano-filler reinforced elastomer systems (see section 2.2 for the theoretical background).
Then, on larger scales, ranging from ten- to several hundred nm, the fractal nature of filler aggregates – as fundamental building-block for a 3-dimensional filler-network – will be analysed, using TEM image analysis (see section 2.3 for theoretical details). Following this, the build-up and breakdown of the filler-network is investigated by combined rheological and dielectric measurements on different non-cured elastomers. Finally, some mechanical experiments on cured samples will be analysed and discussed (see sections 2.1 and 2.4 for an introduction).

4.1. Characterization of Carbon-Based Filler Surfaces using Static Gas Adsorption Techniques

In this section there will be a detailed discussion of different surfaces and their characteristics based on static gas adsorption experiments. First, model surfaces without substantial inhomogeneity will be shown like graphite and graphitized carbon blacks. Then follows an investigation on the influence of surface modifications – via the example of an ionic liquid (here: AMIC, see section 4.3.1 on page 83 for more details) – on the surface features like the energy distribution or the roughness. The final subsection will focus on special surfaces like CNTs, Graphenes or specially treated carbon blacks. In all subsections there will always be a first part about the energetic structure and a second about the morphological roughness to take into account characteristics on different length-scales of the surface for filler materials.

4.1.1. Adsorption on Homogeneous Surfaces: Graphite and Graphitized Carbon Blacks

Graphite or graphitized surfaces are particularly useful for understanding the process of gas adsorption. Due to their very homogeneous surface structure, some theoretical concepts can be tested very easily on them. Especially for the quantitative evaluation of an energy distribution function these surfaces represent the starting point for all other carbon-based filler materials.

Adsorption at Low Pressures: Energetic Homogeneity

The simplest possible model for describing adsorption phenomena is the Freundlich isotherm equation (2.12) with n as a first parameter to characterise the energetic homogeneity of the surface. Hence, by plotting the adsorption data of graphite and graphitized carbon blacks in a double logarithmic plot, a corresponding scaling can be obtained at least at low pressures. Since there is no dependency in the model on temperature or the type of gas, the same scaling is expected for different types of gases. However, due to different cross-sectional areas and applied temperatures, other gases might yield a different scaling of the surface coverage with relative pressure. In figure 4.1a an example of pure graphite is shown. Here, the exponent $1/n$ is

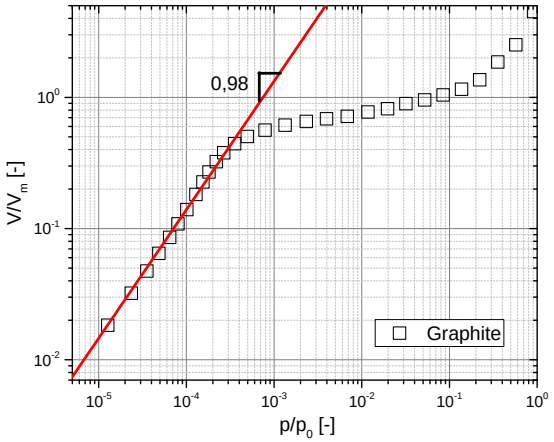

(a) Nitrogen (T=77 K) on graphite

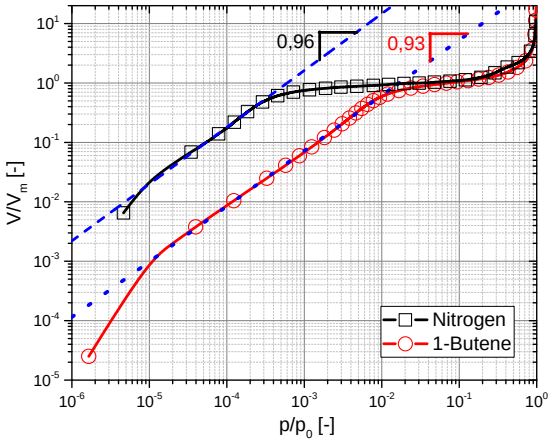

(b) Nitrogen (T=77 K) and 1-Butene (T=266.89 K) on graphitized CB

Figure 4.1.: Adsorption isotherms of graphitized surfaces with applied Freundlich isotherm. Scaling indicates the Freundlich exponent $1/n$.

found to be very close to unity, thus the surface is considered to be very homogeneous. Similar behaviour is depicted in figure 4.1b for graphitized carbon black using two different types of gases. Apparently, the exponent $1/n$ seems to correlate with the type of gas, hence the surface seems to be more homogeneous for Nitrogen molecules than in the case of 1-Butene adsorption. However, considering only two gases is not sufficient for any conclusions, therefore in figure 4.2a the carbon black N234g is investigated using four different types of gas. As depicted in figure 4.2a, the scaling is similar for Nitrogen, Propylene and 1-Butene but very homogeneous for Ethan. It is however often more sensible to compare the value of nRT, i.e. n multiplied with the thermal energy RT (where R and T are the universal gas constant and temperature respectively) rather than $1/n$ from the direct scaling – to take into account the different thermodynamic conditions of the experiments. Accordingly, in figure 4.2b the value of nRT is plotted versus the different cross-sectional areas σ (calculated with equation (2.23)). Obviously, there is a clear correlation between nRT and the size of the used molecules. Therefore, for the investigated graphitized carbon black N234g the level of homogeneity is depending on the molecules applied to the surface and the respective temperature of adsorption. At very low temperatures, i.e. for the adsorption of nitrogen at T=77 K the surface already shows some heterogeneous structures, whereas for Ethan, i.e. a small (saturated hydrocarbon) molecule but measured at higher temperature (T=210 K), the surface yields almost no heterogeneities.

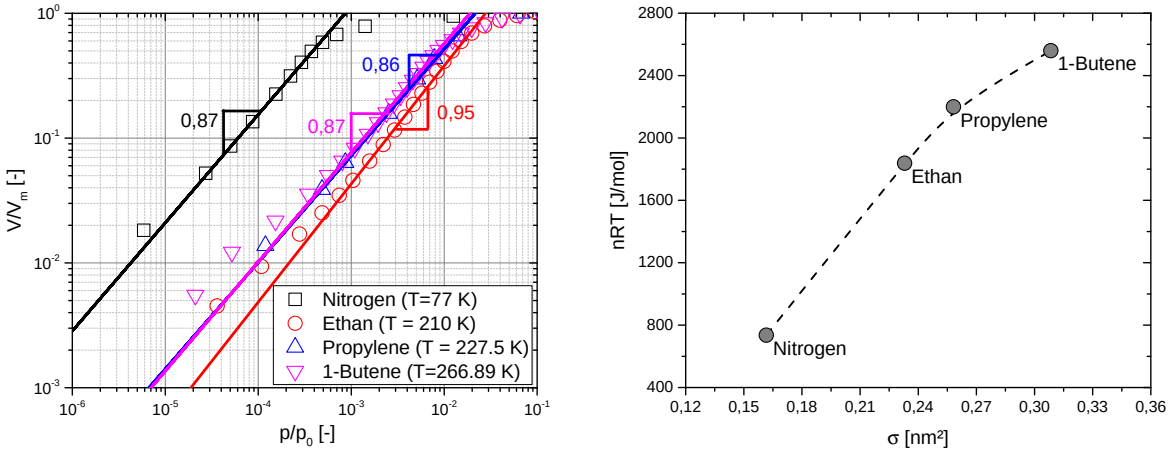

(a) Low pressure Freundlich isotherm with scaling exponent $1/n$

(b) Freundlich exponent nRT depending on cross-sectional area σ

Figure 4.2.: Adsorption isotherms of graphitized carbon black N234g with applied Freundlich isotherm for four different gases.

However, for unsaturated hydrocarbons like Propylene or 1-Butene, the observation is different. Here, the surface even shows heterogeneous structures for higher adsorption temperatures. This is already a first indication, that double bonds are of great importance with respect to their potential for interacting with the π-electrons of the graphite surface via $\pi - \pi$ stacking. Therefore, several graphitized surfaces will be investigated using the adsorption of nitrogen and 1-Butene.

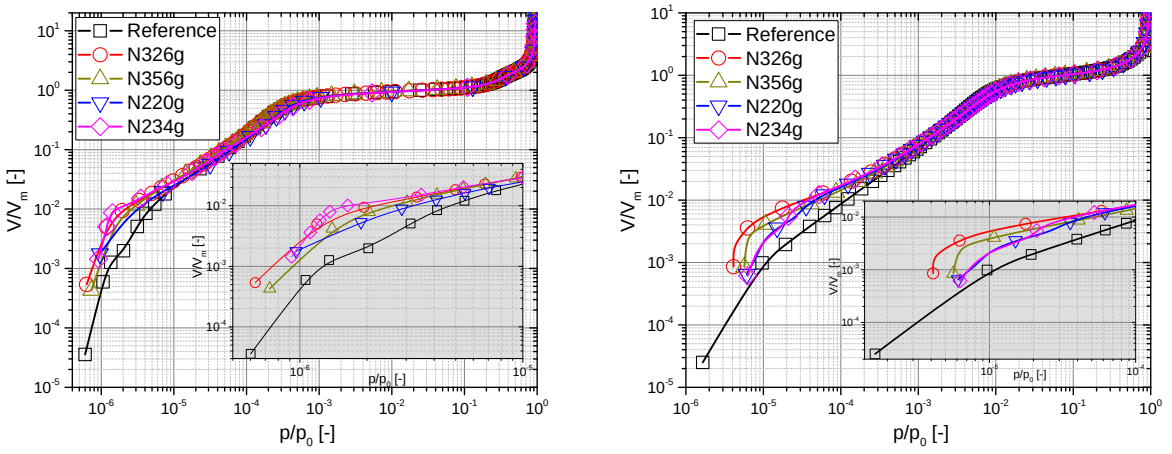

(a) Nitrogen (T=77 K)

(b) 1-Butene (T=266.89 K)

Figure 4.3.: Adsorption isotherms of different graphitized surfaces. The insets show the low pressure regimes.

From figures 4.3a and 4.3b a similar medium- to high-pressure region can be identified. At low relative pressures $p/p_0 < 10^{-5}$ in the case of nitrogen and $p/p_0 < 10^{-3}$ for 1-Butene, a spreading in the surface coverage indicates some differences regarding the energetic heterogeneities of the different graphitized carbon blacks. In general, the most homogeneous surface is the

reference sample, which is a graphitized carbon black undergoing a special treatment involving platinum during the graphitization process.
All other graphitized carbon blacks are very similar and show only very minor differences. Since the graphitization process is a homogenization of the surface structures, i.e. the defects vanish almost completely [47] and the graphitic-crystallites are growing in size [139], there is no dependency on the specific surface area or structure visible in the ranking of the different carbon blacks. This is even more obvious considering the scale on which these effects are relevant.[1] Though, even for graphitized surfaces there can still be a wide range of surface activity. In figure 4.4 three different types of graphite are depicted. Comparing the pure graphite pow-

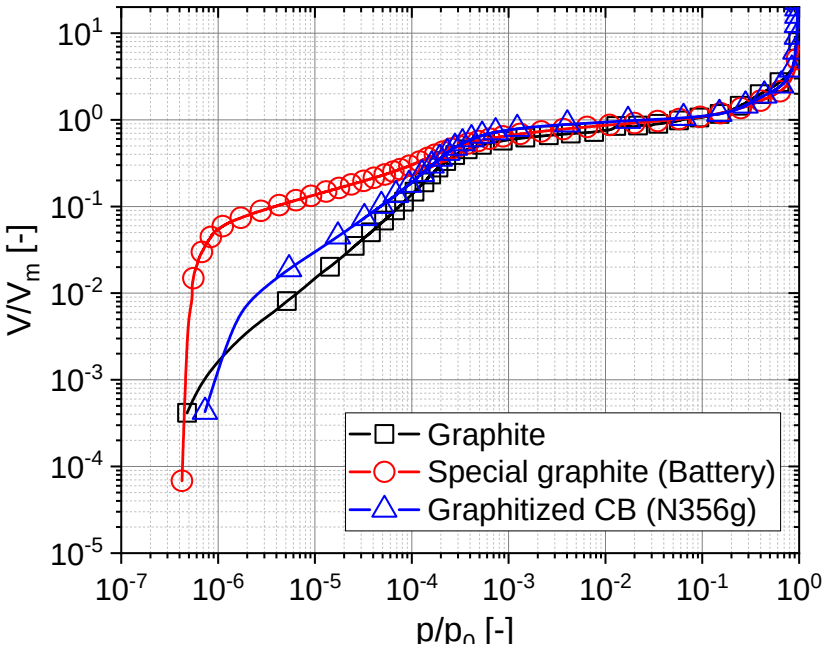

Figure 4.4.: Nitrogen (T=77 K) adsorption isotherms of three different types of graphite. The indicated special graphite is SGB10L (see table 3.1 on page 37) from Kropfmühl GmbH, often used in battery technology.

der with an graphitized carbon black yields already a small difference in the level of activity, hence surface heterogeneity. Obviously, this difference is negligible in comparison to the special graphite SGB10L from Kropfmühl GmbH. Here, a very high level of heterogeneity is achieved although the surface area is comparably small (11 m^2/g, see table 3.1). This special graphite is often used in electronics especially in battery technology.
Up to this point, only qualitative statements with respect to the energetic structure of the surfaces could be given. For a first-order approximation of the surface-energy and their respective distribution, a method, which was first used by Ross and co-workers will be used [140]. Here, a special form of the energy distribution function $f(Q)$ is assumed and with – in the simplest case – the Langmuir equation without modifications used as model isotherm in equation (2.26), an isotherm can be constructed. For homogeneous surfaces a single Gaussian peak is often sufficient to describe the observed experimental isotherm fairly well. In figures 4.5a and 4.5b this

[1] For the surface area, the mean diameter of the primary particles is relevant ($10 - 100$ nm); The structure is determined by the shape of the primary aggregate ($30 - 200$ nm).

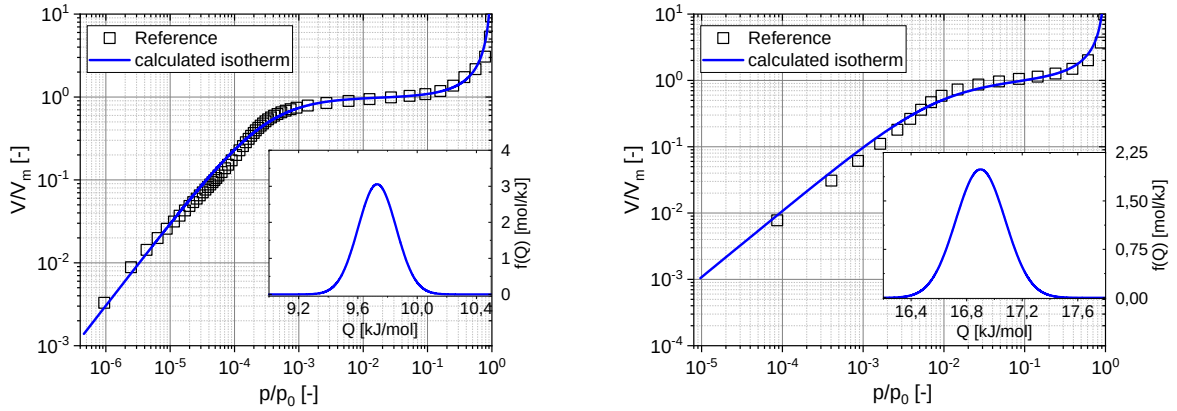

(a) Nitrogen (T=77 K)

(b) 1-Butene (T=266.89 K)

Figure 4.5.: Adsorption isotherms of the reference graphitized CB with calculated isotherms, assuming one single Gaussian-peak, without lateral interaction. The inset shows the corresponding energy distribution function.

method has been applied for nitrogen and 1-Butene adsorption on the reference carbon black. Omitting any lateral interactions between adjacent gas molecules, the assumption of one single, rather narrow, Gaussian peak agrees reasonably well with the experimental data. However, the special feature of the characteristic curvature around the transition point between linear, i.e. Freundlich-like to mono-layer, i.e. Langmuir adsorption, is not very well represented by the calculated isotherm. Additionally, there is an inflection point in the isotherm data within the low pressure regime (Nitrogen: $p/p_0 \sim 5 - 6\ 10^{-5}$; 1-Butene: $p/p_0 \sim 1 - 2\ 10^{-3}$), which cannot be found in the calculated isotherm. Regarding the characteristic sharp transition from sub- to mono-layer coverage, this can be adjusted with the width of the energy distribution function and more importantly by considering lateral interactions between the adsorbed gas molecules. In figures 4.6a and 4.6b the effect of the latter is depicted. A clear shift of the energy distribution is apparent, which leads to a much better fit between the calculated and measured isotherm. Considering several different Gaussian peaks, enhances the quality of agreement even more. Especially in the low pressure regime, sites with higher energy are very important. The position of the various peaks is representing different energetic structures of the surface, i.e. besides the main peak indicating the graphitic basal plains, there are several structural defects like edges or cavities present on the surface (see figure 4.7, a similar explanation can be found here: [47]).

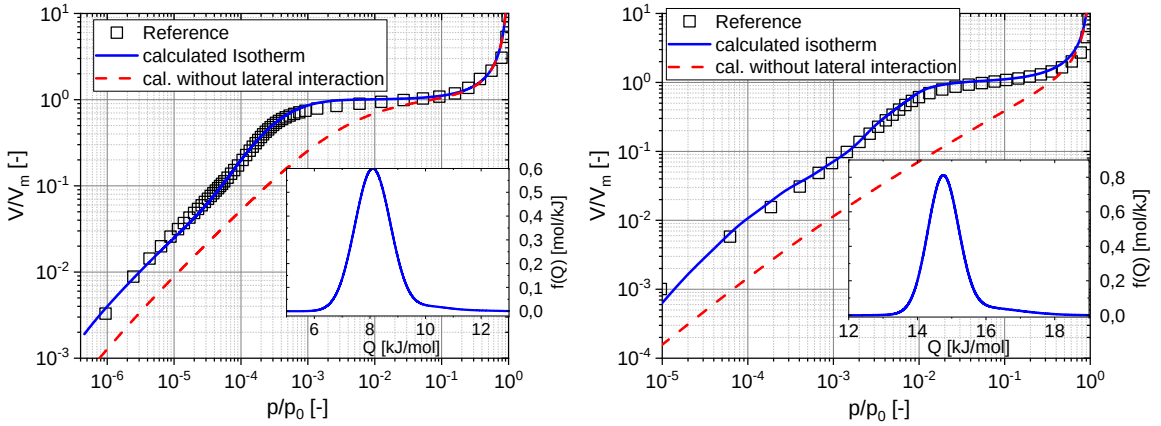

(a) Nitrogen (T=77 K) (b) 1-Butene (T=266.89 K)

Figure 4.6.: Influence of lateral interaction of gas molecules on a graphitized reference surface. Depicted in the inset is the estimated energy distribution function, constructed out of four different Gaussian peaks. The dashed red line was calculated, using the same energy distribution, but omitting lateral interactions.

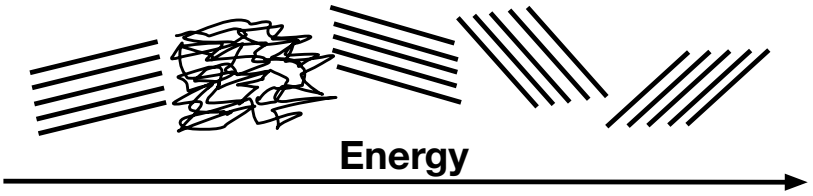

Figure 4.7.: Illustration of different possible surface structures on carbon blacks, representing different energy levels. With increasing energy there are: (i) basal-plains of graphite crystallites, (ii) amorphous carbon, (iii) edges due to defects between crystals and (iv) slit like cavities. Figure based on [113]

Comparing the energy distribution function in the inset of figure 4.6a with the one in figure 4.6b, shows a shift towards higher energy values, but essentially no qualitative different shape. Therefore, in case of a very homogeneous surface, the surface probed by a nitrogen molecule looks very similar to the surface a 1-Butene molecule can "see". However, omitting the lateral interaction, while taking the same energy distribution function as indicated via the red dashed line in figure 4.6, leads to a very different shape and position of the calculated isotherms. In other words, there needs to be a shift in the whole energy distribution function towards higher energies to compensate at least the main discrepancy caused by the effect of lateral interaction. Henceforth, all energy distributions are calculated considering lateral interaction.
In figure 4.8 two example isotherms of the graphitized carbon black N220g are shown for Nitrogen and 1-Butene adsorption. In both cases the experimental data is shown as symbols and an calculated isotherm, using the energy distribution function depicted in figure 4.9, is shown

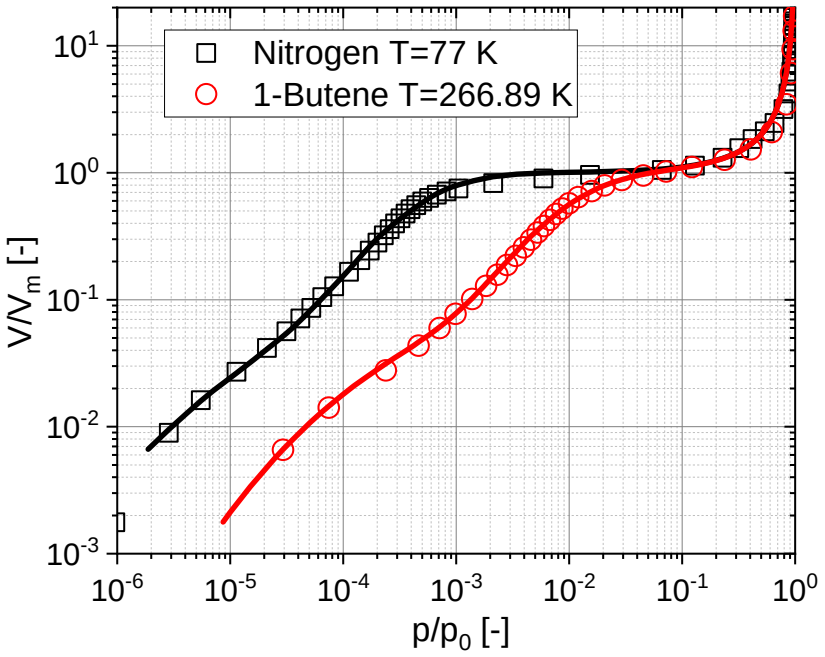

Figure 4.8.: Adsorption on graphitized carbon black (here: N220g as an example) with calculated isotherms, using four Gaussian peaks in the energy distribution function and equation (2.27) on page 18 as model isotherm.

with a line. Figure 4.9 finally shows the energy distribution of several graphitized carbon blacks (see figure 4.3 for all isotherms) for adsorption of Nitrogen an 1-Butene.

All surfaces show a characteristic, sharp main peak and only minor portions of highly active

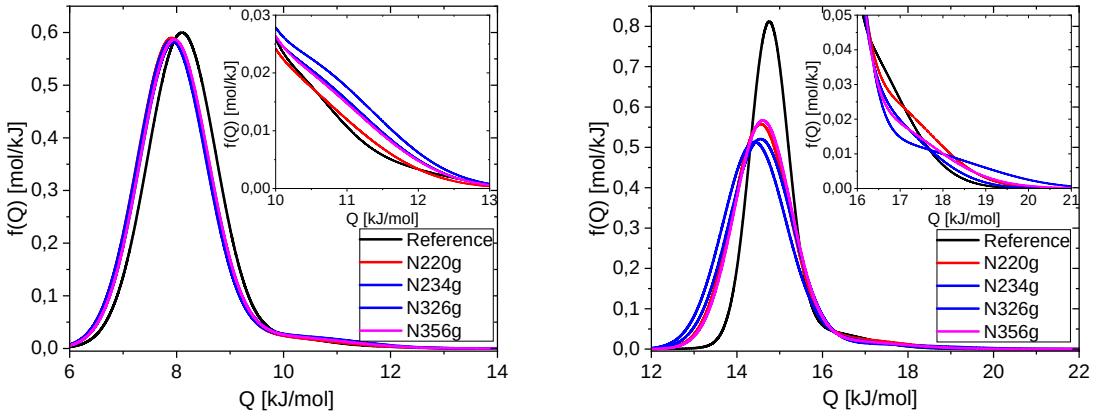

(a) Nitrogen (T=77 K)

(b) 1-Butene (T=266.89 K)

Figure 4.9.: Evaluated energy distribution functions for different graphitized carbon blacks (see figure 4.3 for the respective isotherms). The inset shows a zoomed view of the area of high energies Q.

sites, i.e. defects or cavities. In case of 1-Butene, the reference carbon black shows a slightly more narrow peak representing the graphitic crystals. This is presumably due to the special sur-

face treatment during the graphitization process. In general for both types of gas, the portions of sites with energies higher than 20% of the main peak $Q > 1.2\,Q_{\text{graph. crystals}}$ is lower than 1% in terms of their occurrence.

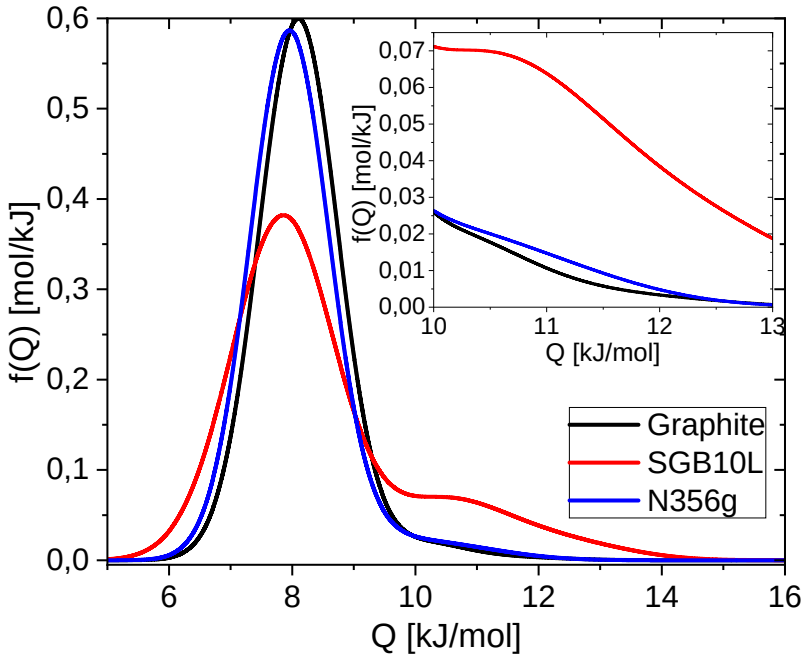

Figure 4.10.: Energy distribution function for three different types of graphite (see figure 4.4 for the isotherm data) for the adsorption of nitrogen (T=77 K). The inset shows a magnification of the high energy region.

Figure 4.4 already indicates, that there will be a much bigger difference in the energetic structure comparing these different graphite surfaces. Consequently, in figure 4.10 the corresponding energy distribution functions are depicted. There is a clear difference in the width of the graphitic main peak as well as in the ratio of highly active sites. Apparently, there are 5 times more sites with higher energies present, compared to the graphitized carbon black.

Influence of Surface Morphology in Multilayer Adsorption

In the previous paragraph, all relevant scales are in the range of the size of gas molecules, i.e. below nano-meter, up to the mono-layer coverage $V = V_m$, which is determined by the size of the primary filler particles (10-90 nm). Accordingly, the energetic structure of the surface has been primarily investigated. Additionally to this energetically based inhomogeneity, there is a morphological roughness of the surface. For characterizing this roughness effects, the adsorption of gas molecules in multiple layers has to be investigated. In figure 4.11 an example of the adsorption for nitrogen on the reference carbon black is shown. Using a linear y-axis, first a moderate increase of volume is observed. After approximately twice the volume of a mono-layer V_m has been adsorbed, the amount of gas increases more rapidly while approaching the saturation vapour pressure p_0. In section 2.2.3 the basics of investigating the morphological roughness have been introduced. Using the classical fractal FHH-plot, the surface fractal dimension D_S can be obtained. In figure 4.12 the fractal FHH-plot is depicted for nitrogen

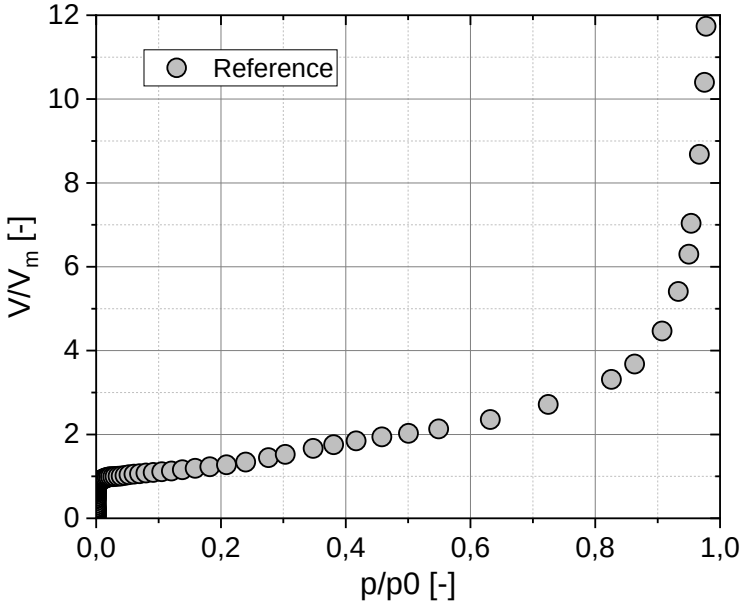

Figure 4.11.: Multi-layer adsorption of reference material for nitrogen ($T = 77\ K$).

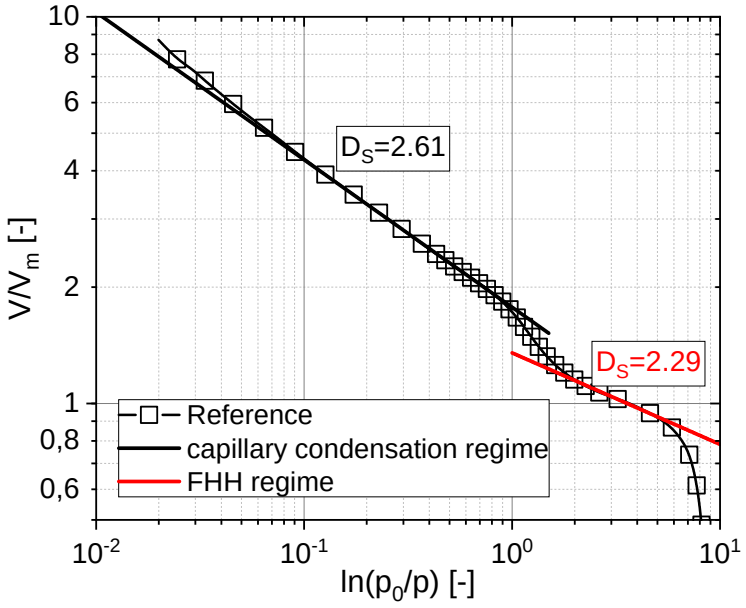

Figure 4.12.: Classical fractal FHH-plot of reference material for nitrogen ($T = 77\ K$).

adsorption on the reference carbon black. According to equation (2.33) (see section 2.2.3 on page 19), there should be a linear scaling in a double logarithmic plot. In fact, there are two separated regimes observable in figure 4.12. At lower pressures, i.e. on the right hand side in the plot, where the surface coverage V/V_m is around unity, a lower roughness value is observed ($D_S = 2.3$). As the surface gets covered successively, the roughness changes to a higher value ($D_S = 2.6$). The first regime is assumed to be dominated by the short-range van-der-Waals interaction because these low pressures represent only small distances from the surface, i.e. thin films of gas molecules (Often referred to as FHH-regime – see the red spheres in figure 2.6,

representing the layer of molecules in the vicinity of the surface.). Hence, the van-der-Waals potential dominates the interaction process and therefore equation (2.34) can be used to fit the observed scaling.
In the second regime, often referred to as capillary condensation regime, equation (2.35) is valid because the interaction is dominated by the surface tension γ of the solid-adsorbate-interface at larger film thicknesses. This observation for graphitized carbon black indicates a geometrical cut-off length, where the surface becomes rougher, thus the surface is of bi-fractal nature. However, the value of $D_S = 2.6$ beyond the cut-off represents a rather rough surface and other methods, e.g. indicate a rather smooth surface for graphitized CB ($D_S < 2.4$).[106] In general, all graphitized carbon blacks show a similar behaviour with a universal roughness of $D_S = 2.3$ on small scales and $D_S = 2.6$ on larger scales (see: [44, 93]).
Alternatively to the aforementioned classical, fractal FHH-plot, the usual x-axis scaled with $ln(p_0/p)$ can be transformed into a new axis scaled with the film thickness z/z_m, where z is the distance from the surface and z_m is the average thickness of a mono-layer, i.e. the size of the respective gas molecules. By solving equation (2.32) for z, a relation between z and the pressure p can be obtained (see appendix A.1.1 for the corresponding formulas). In figure 4.13

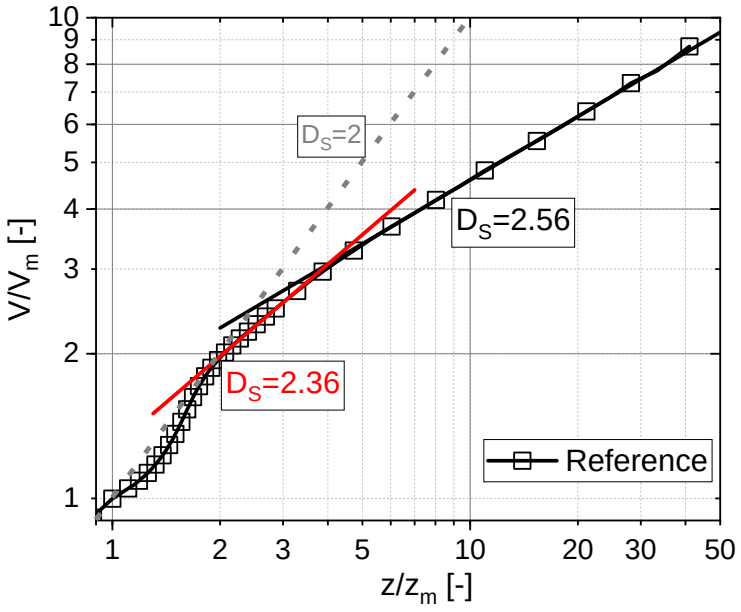

Figure 4.13.: Transformed fractal FHH-plot for the reference carbon black for nitrogen (T=77 K) adsorption. Scaling according to equation (2.31) with $z_m = 0.35$ nm [141].

this coordinate-transformation has been performed and the resulting transformed FHH-plot is shown for the same system as in figure 4.12. Here, the surface coverage V/V_m is shown as a function of the average film thickness z/z_m. On perfectly flat surfaces with $D_S = 2$ a linear scaling ($D_S = 2 \Rightarrow 3 - D_S = 1$) between the volume and the thickness of the respective film is expected. In figure 4.13 this case is represented by the gray, dotted line. Interestingly, there is no simple power-law dependency observed between the mono-layer coverage and the formation of a second layer of gas $V/V_m = z/z_m = 1 \rightarrow V/V_m = z/z_m = 2$. In fact, the data of all graphitized carbon blacks coincide within this interval, indicating no (or only minor) observable roughness effects for the first two layers of gas molecules. Furthermore, the point

$V/V_m = z/z_m = 2$ seems to represent an universal cut-off length, at which the surface roughness takes effect.
Consequently, beyond the formation of a second layer, the slope is apparently smaller compared to a flat surface. This first regime of roughness between $2 < V/V_m < 3$ and $2 < z/z_m < 4$ yields a surface fractal dimension of $D_S = 2.36$. This regime represents small distances $z < 1.4$ nm and could be attributed to the roughness before the geometrical cut-off observed also in the classical FHH-plot by only considering the van-der-Waals interaction. However, in the transformed FHH-plot there is no separation of interaction-regimes necessary, since both contributions are intrinsically considered by calculating the value for the film thickness z from the measured pressure p. Beyond the point $(V/V_m = 3,\ z/z_m = 4)$ a surface roughness of $D_S = 2.56$ can be found, which is comparable to the expected roughness from the classical FHH-plot.

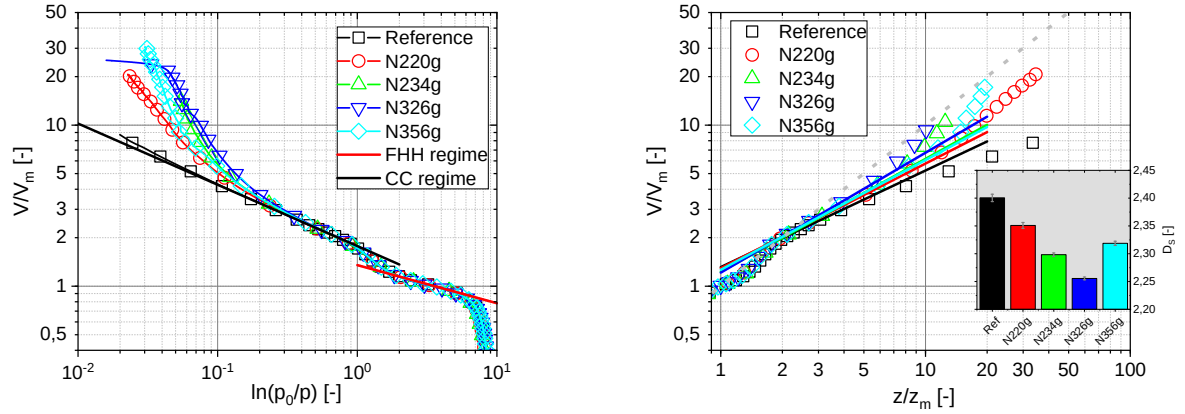

(a) Classical FHH-plot; Fits according to figure 4.12

(b) Transformed FHH-plot; Inset shows the respective fractal dimensions D_S, fitted in the range $2 < z/z_m < 6$

Figure 4.14.: Fractal FHH-plots of different graphitized carbon blacks for nitrogen (T=77 K) adsorption.

Comparing the classical FHH-plot for different graphitized carbon blacks (see: figure 4.14a) with the transformed FHH-plot (see: figure 4.14b)indicates a wider spreading for larger film thicknesses in case of the transformed FHH-plot. For the classical FHH-plot all graphitized carbon blacks follow the same curve until $ln(p_0/p) < 0.2$. Thus, there is an universal scaling in both regimes. However, the transformed FHH-plot shows increasing differences for thicknesses $z/z_m > 2$. Hence, there are different roughness values evaluated for the various samples (see the inset of figure 4.14b).
However, these differences do not reflect any macroscopically accessible structural parameter like the DPB number.[2] Rather, the differences are additionally influenced by experimental uncertainties in the high pressure regime, i.e. close to the saturation vapour pressure p_0. Nevertheless, information about the morphological surface-roughness can be obtained via the FHH-plot. Since small molecules like nitrogen are interacting differently than segments of polymer-chains, a natural next step is to utilize larger, more polymer-analogues gas molecules like 1-Butene for instance. In case of 1-Butene adsorption, no transition regime at lower pressures or film-

[2]The ranking between the values of D_S of N234g and N220g is contradicting their DPB number, although for the N326g and N356g the ranking is correct.

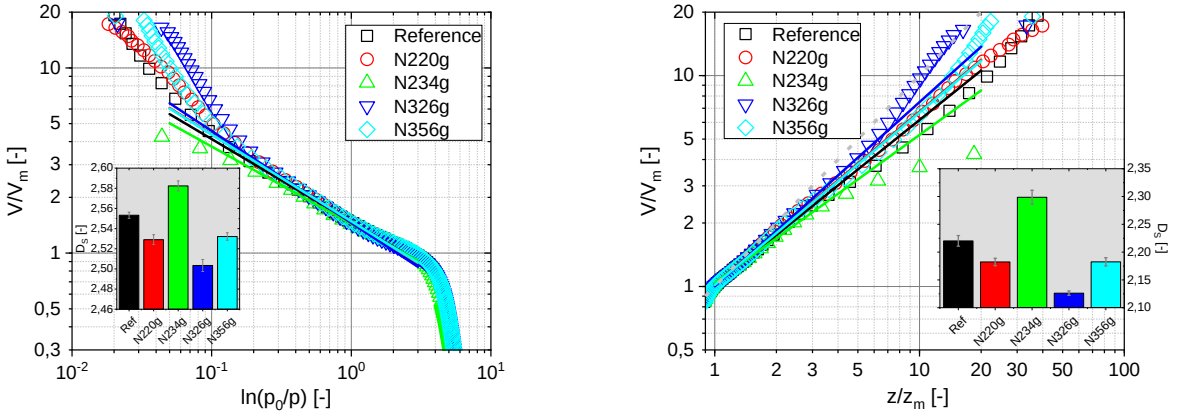

(a) Classical FHH-Plot

(b) Transformed FHH-Plot

Figure 4.15.: Fractal FHH-plots of different graphitized carbon blacks for adsorption of 1-Butene (T=266.89 K).

thicknesses is apparent (see figure 4.15). This is likely to be caused by the size of the 1-Butene molecules, which are almost twice as big as nitrogen molecules. Consequently, there will be less sensitivity for small-scale morphological structures present on the surface. For the classical FHH-plot the scaling is now not equal for the different graphitized carbon blacks, but still very similar ($2.5 < D_S < 2.58$), although slightly smaller, compared to nitrogen adsorption (see the inset of figure 4.15a). Again the overall spreading of the data is more pronounced for the transformed FHH-plot, hence there is a bigger scattering also in the fractal dimensions ($2.12 < D_S < 2.3$), which are considerably smaller than for the classical FHH-plot. The estimated values suggest a much smoother surface for the graphitized carbon blacks. Additionally the ranking between the different grades now follows the expected ranking of the macroscopically defined structure (e.g. DPB number).

4.1.2. Influence of Surface Modification on the Adsorption Characteristics

In the previous subsection, exclusively graphitized carbon blacks have been investigated. Therefore, it is necessary to give a comparison between graphitized carbon blacks and its non-graphitized, i.e. normal version.

In figure 4.16 the ASTM carbon black grade N234 is depicted with its graphitized version N234g (see table 3.1 for their characteristic descriptors), showing a generally different adsorption behaviour. At low pressures, the normal CB shows a much higher activity, hence at the same pressure much more of the surface is covered with gas molecules (e.g. at $p/p_0 = 10^{-5}$ the N234 shows a coverage of ≈ 10 % whereas for the N234g only 3 % of the surface is covered). Furthermore, a characteristic differentiation between these CB types at medium relative pressures ($10^{-4} < p/p_0 < 10^{-2}$) is apparent.
Based on these differences, modifications of the ASTM grade N339 using the ionic liquid AMIC according to the procedure described in subsection 3.3.2, can be evaluated. Three different

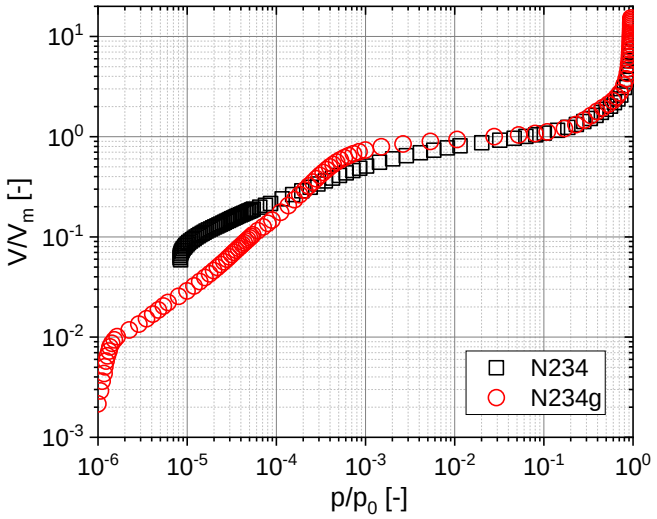

Figure 4.16.: Nitrogen adsorption isotherm (T= 77K) of N234 and its graphitized version N234g.

types of gas molecules have been used to characterize influences of the ionic liquid modifications. For this purpose, nitrogen as smallest molecule – hence probing the surface on the lowest length scale – propylene and 1-butene as monomer-similar gas molecules have been chosen. In figure 4.17 the resulting isotherms are plotted. To obtain a comparable saturation vapour pressure p_0 of approximately one bar, the temperature was adapted for the different gases accordingly. In general, there is a clear trend showing a reduced surface activity due to the modification compared to the unmodified carbon black. Especially for propylene the difference in surface coverage at low to medium pressures is significant.[3] Comparing the magnitude of the modification-effect between nitrogen and propylene adsorption, i.e. probing different length-scales of surface characteristics shows for the smaller nitrogen molecules less effect by the presence of AMIC molecules blocking certain features on the surface than for the larger, more polymer analogues propylene molecules.
However, comparing the nitrogen adsorption behaviour of the graphitization with the AMIC modification, indicates important differences. During the process of graphitization, the morphology of the surface changes on various length-scales. On scales below 1 nm, the surface will lose almost all its heterogeneous structures like crystallite-defects, edges or cavities, hence it will become energetically very homogeneous. Additionally, on the scale of several nm, the size of graphitic crystallites will increase from 5-10 nm up to 10-25 nm. These morphological changes of the surface lead to an overall remarkably different adsorption trend on a very broad range of relative pressures p/p_0 (see figure 4.16).
Thus, the difference observed in figure 4.17a, i.e. the drop in surface coverage at low pressures, is originating from purely local blocking of certain high-energy sites due to the presence of AMIC molecules.[4] Since there are no morphological changes because the surface is affected only locally, the resulting adsorption curves at medium and high relative pressures are similar. In fact, this is evident for all used gas types, as in all plots the curves with and without modifi-

[3]There is almost one order of magnitude difference for pressures $p/p_0 < 10^{-4}$ in the surface coverage.
[4]The AMIC molecules during the modification process will naturally favour the high energy sites of the CB, hence these sites will be blocked by AMIC molecules and therefore are not longer available for gas molecules.

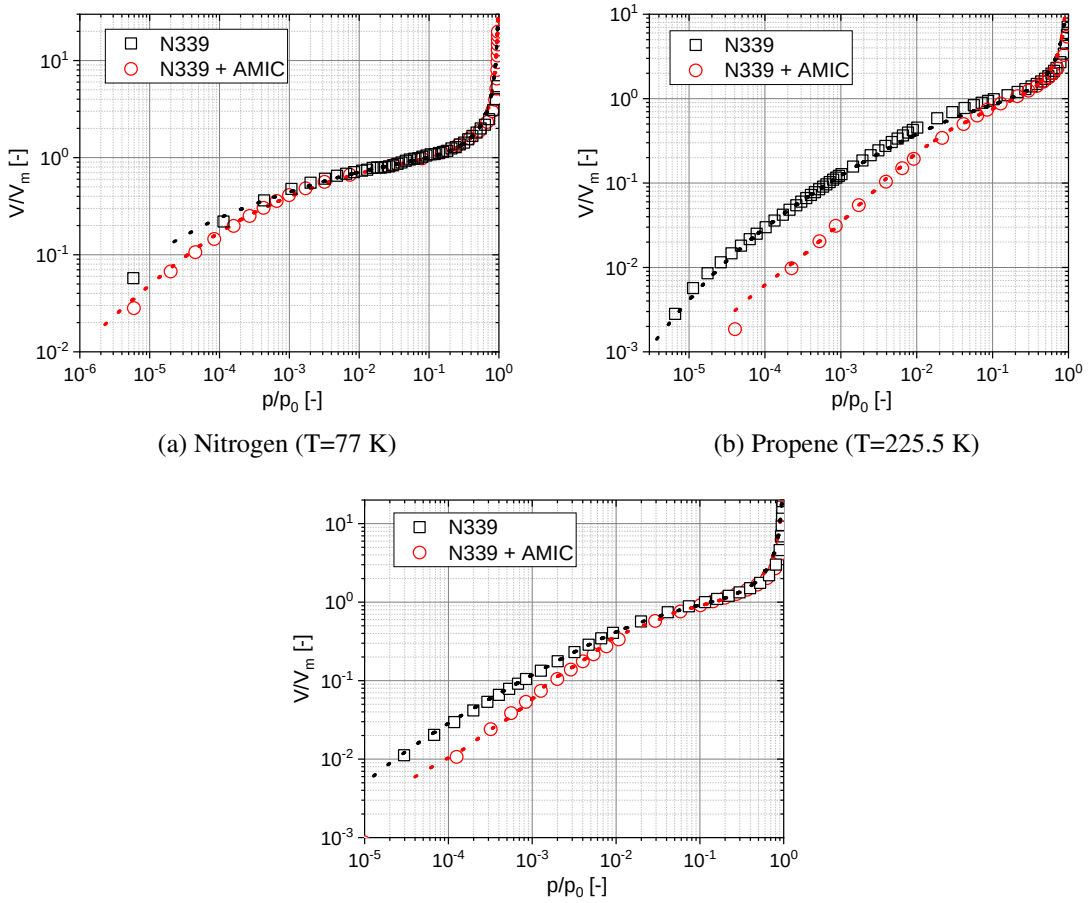

(a) Nitrogen (T=77 K)

(b) Propene (T=225.5 K)

(c) 1-Butene (T=266.89 K)

Figure 4.17.: Adsorption isotherms for N339 with and without modification with AMIC. The dotted lines indicate the calculated isotherm using the energy distributions depicted in figure 4.18

cation coincide at medium (Nitrogen) or at least higher pressures. Consequently, a calculation of the energy distribution function is meaningful, since these blocking effects should be apparent at the high energy regime of the surface. In figure 4.18 the respective energy distribution functions are shown for the three gas types. Unsurprisingly, the resulting graphs show a drop in the number of high energy sites for all types of gases, hence strengthening the aforementioned overall hypothesis of blocking surface-sites by AMIC molecules. Finally, analysing the specific surface area shows – as expected from the previous reasoning – no influence of the AMIC modification at all. In figure 4.19 the BET plot of all systems is shown. Obviously, there is no difference in slope at values of relative pressures $p/p_0 < 0.2$ for the respective type of gas, hence the surface area is unchanged.[5] Nevertheless, there are only minor differences occurring in the FHH-plots shown in figure 4.20, which could be attributed to the change of surface en-

[5]The specific surface area is calculated via the volume of one monolayer V_m (see eq. 2.24), which is reciprocally proportional to the sum of slope and intercept of a linear fit (see explanation on page 15). In the shown BET-plot in figure 4.19, the intercept is very close to zero, thus the slope will be the dominant term in calculating V_m and therefore also in the specific surface area.

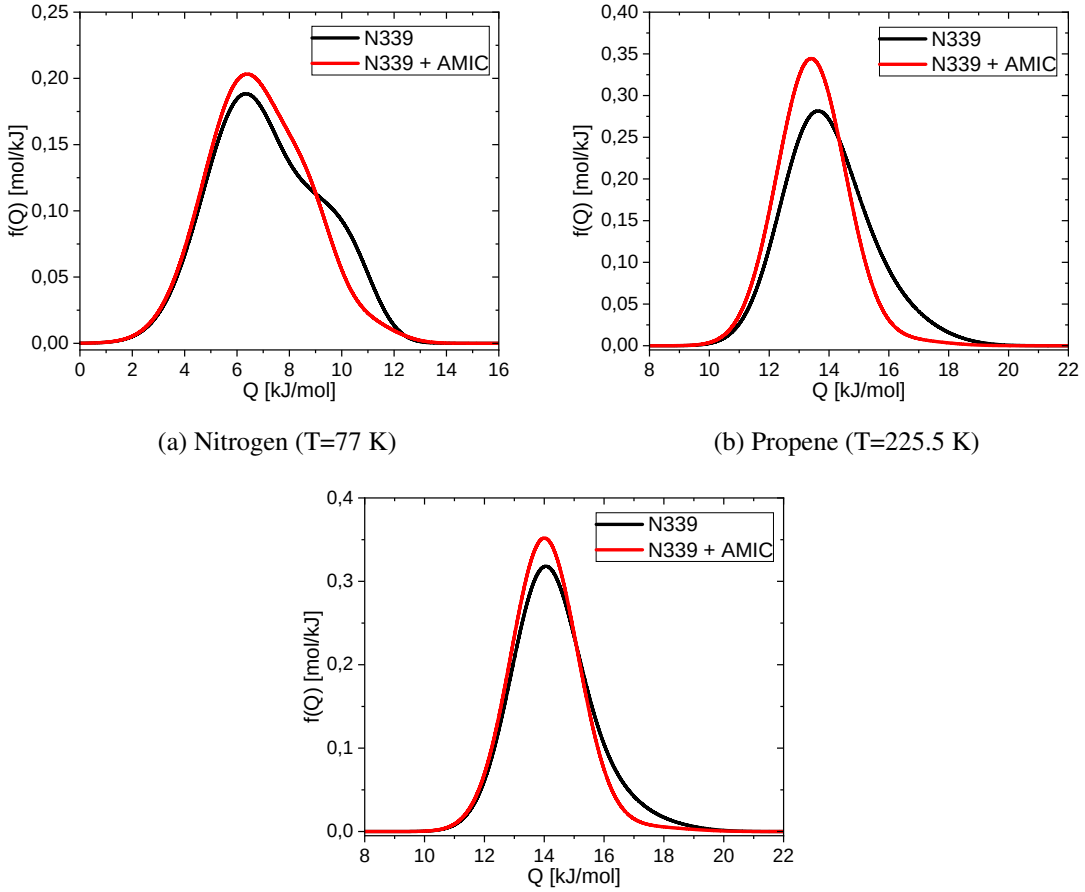

(a) Nitrogen (T=77 K)

(b) Propene (T=225.5 K)

(c) 1-Butene (T=266.89 K)

Figure 4.18.: Energy distribution functions for N339 and N339 modified with AMIC.

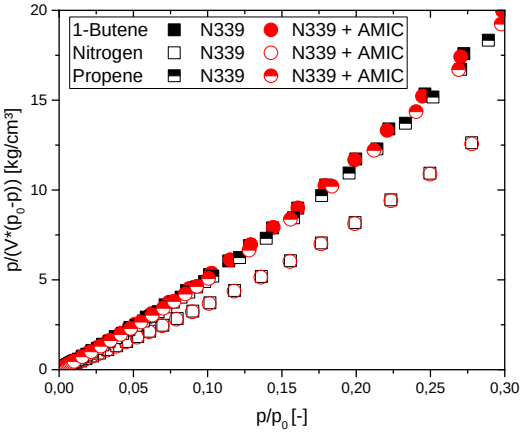

Figure 4.19.: BET plot with respect to equation (2.25) of N339 with and without AMIC modification for three type of gases as indicated.

ergy due to the polar ionic liquid. The observed differences in scaling, i.e. the fractal dimension of the surface D_S, are of minor magnitude and shouldn't be attributed to severe morphological

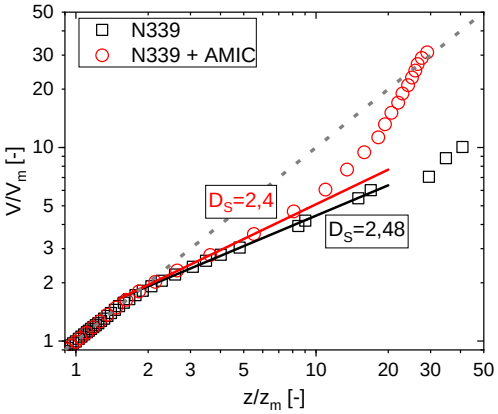

(a) Nitrogen (T=77 K)

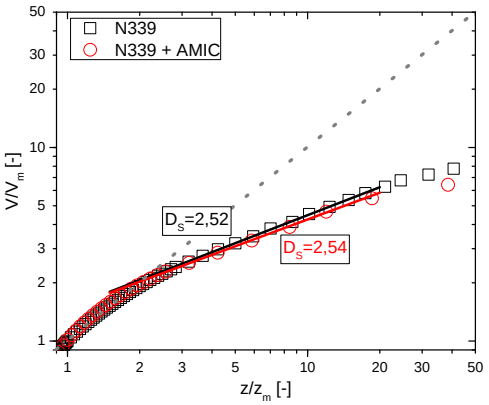

(b) Propene (T=225.5 K)

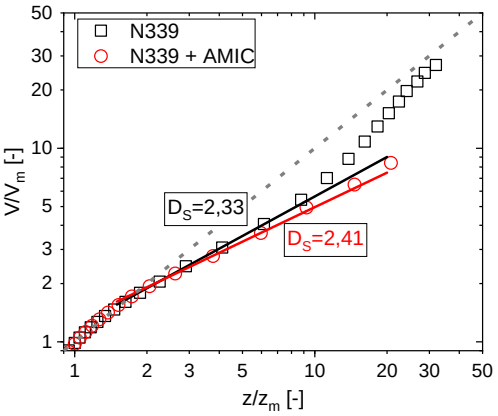

(c) 1-Butene (T=266.89 K)

Figure 4.20.: Fractal FHH-plots for N339 and N339 modified with AMIC.

changes due to AMIC-modifications. It is more likely a result of unknown surface parameters characterizing the capillary condensation potential (see second addend in eq. 2.32), e.g. the surface tension γ.

4.1.3. Gas Adsorption on Surfaces Featuring Unique Structures

In this subsection, special adsorption characteristics of different filler types will be discussed. Especially focussing on a wide range of different carbon-based filler materials, trying to elucidate the differences with respect to a well known reference surface like graphite. Additionally to carbon blacks, carbon nano tubes (CNT), graphenes or carbon nanohorns (CNH) are of recent interest as novel filler materials in elastomer composites. That is mainly due to the very high specific surface area (often several 100 m^2/g), which leads to a very high reinforcing potential and additionally to a very low mechanical- and electric percolation threshold. [130, 131]

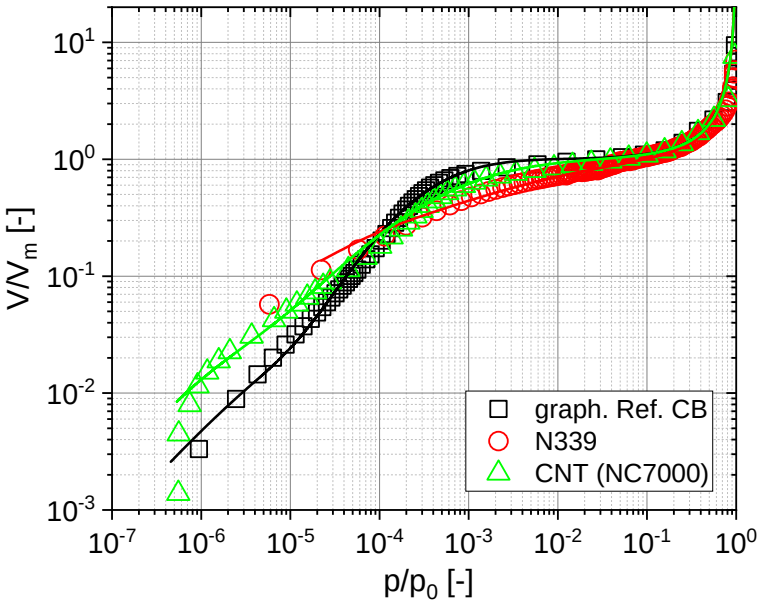

Figure 4.21.: Nitrogen adsorption (T=77K) of different carbon-based filler materials - graphitized CB, CB and carbon nanotubes (CNT). Lines indicate the calculated isotherms using the energy-distribution depicted in figure 4.26.

Comparing CNTs and the standard ASTM CB N339 with graphitized CB as depicted in figure 4.21 it is apparent, that the shape of the CNT curve shows more similarities to the graphitized CB than to the N339. Thus, the surface of a typical CNT shows very little high energy sites or amorphous structures like it is observed in typical CB samples. However, there are some high energy features present on the surface compared to the homogeneous reference, which is reflected by an increased surface coverage at low relative pressures $p/p_0 < 7 \cdot 10^{-4}$. These sites could possibly be found on each end of the tubes since at these locations edges and cavities are naturally located. This hypothesis is reinforced by a comparison to figure 4.3 with all graphitized CB types, which shows, that the CNT curve still yields higher low-pressure coverage values.
Moreover, there is a different curvature at medium relative pressures $10^{-4} < p/p_0 < 10^{-2}$ visible comparing CNT and graphitized CB. This transition regime shows in principle how quickly the surface will be covered up to the full mono-layer coverage $V = V_m$. Therefore, the curvature is an indirect indicator of the width of the energy distribution function, hence the energetic homogeneity, which ultimately can be seen in figure 4.26. Especially the N339 shows a very low curvature, hence shows a very wide energy distribution compared to the very narrow graphitized

CB. Due to the fact, that CNTs and graphenes are in principal both based on one mono-layer

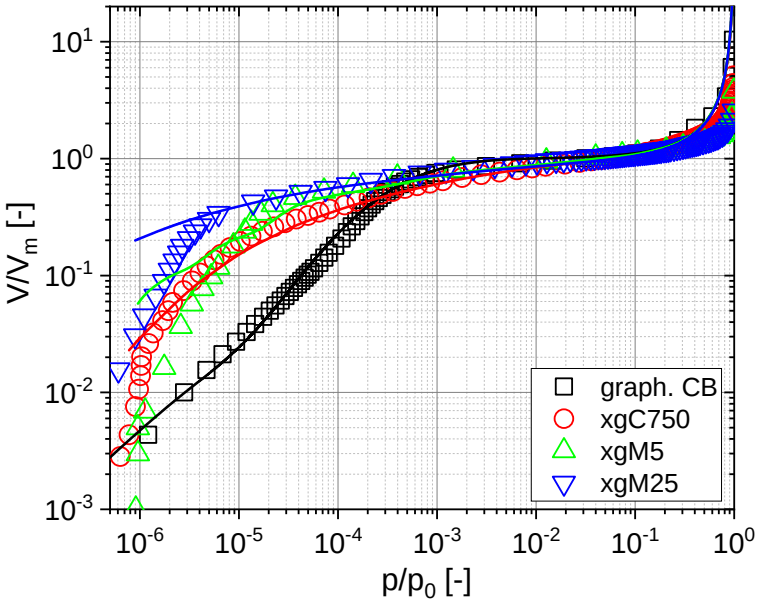

Figure 4.22.: Nitrogen adsorption (T=77K) of different carbon-based filler materials - graphitized CB and several graphenes. Lines indicate the calculated isotherms using the energy-distribution depicted in figure 4.26.

of graphite,[6] the comparison to graphitized CB should unveil interesting commonalities. However, most commercially available CNT-types are multi-wall CNT and graphenes are usually graphene-nano-platelets (GnP) or graphene-oxides. Especially these GnPs show very interesting structural properties.[131] The nitrogen adsorption isotherms shown in figure 4.22 indicate a significantly different behaviour of the GnPs compared to the graph. CB (and therefore the CNT). Most obviously, all types of GnP show a very high activity of the surface i.e. the coverage at low pressure is more than 10 times larger compared to graph. CB.
All types of GnPs shown here, exhibit a platelet structure, where stacked layers of graphite sheets form particles of sizes between 2 (xgC grade) and 25 (xgM25 grade) micrometers. From the specific surface area data of these GnPs in table 3.1, apparently these particles need to have an inner structure in the nanometer range, because only then these high values can be explained.[7] Most probably, the layered structure of the sheets are forming platelets and therefore causing the observed high activity of the surface. From a molecular point of view it is reasonable to assume, that gas molecules can penetrate this layered structure and therefore a lot of gas molecules can be adsorbed either between the sheets or at the stair-way like structures at the edges of platelets – already at very low pressure.[133]
In case of 1-Butene there is a qualitatively similar behaviour observable (see figure 4.23for the isotherms and energy-distributions). Here, the GnPs also show a very high activity compared to CB or graphitized CB. However, there are some remarkable differences. First of all, the high energy peak in case of nitrogen shows a higher amplitude compared to the main peak, which

[6] In principle, a single-walled CNT is a rolled-up graphene-sheet.
[7] For fillers, which consist of particles in the micrometer range, the typical values for the specific surface area are below 1 m^2/g.

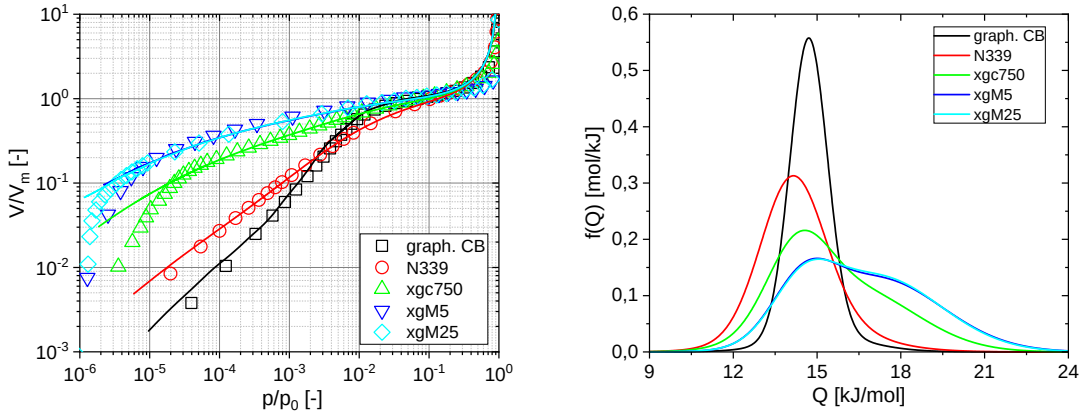

(a) Isotherm data

(b) Energy-distribution

Figure 4.23.: Comparison of graph. CB, CB and several GnPs for 1-butene (T=266.89 K) adsorption. The lines shown in the isotherm graph represent calculated data using the energy-distribution plotted besides.

is usually attributed to the graphitic planes of the crystals. This peak-to -peak ratio is reduced for 1-butene molecules,[8] which results from the bigger size of the 1-butene molecules that cannot enter the stacked structures as easily as nitrogen molecules. On the other hand, comparing the surface coverage at low pressures for both gases, reveals a very high affinity of 1-butene molecules to the graphene surface. Nitrogen molecules are covering always more of the surface compared to 1-butene molecules. This effect is shown in figure 4.24 in which the relative surface coverage $\Theta_{Nitrogen}/\Theta_{Gas}$ is plotted versus the relative pressure. For a typical CB (here N339 as an example) the ratio between nitrogen- and 1-butene surface-coverage is greater than 10 for low relative pressures $p/p_0 < 10^{-4}$, i.e. there are ten times more nitrogen molecules adsorbed onto the surface than 1-butene molecules. One aspect of this huge difference is the different temperature at which the measurement has been conducted ($\Delta T = 190K$), since the desorption rate is a function of temperature.[9] For N339, additional measurements using propylene as adsorptive gas have been performed at varying temperatures (see: dashed lines in figure 4.24). This yields a clear temperature dependency of the relative surface coverage, i.e. with increasing temperature, less propylene molecules can cover the surface.[10] However, the relative coverage of the GnPs is significantly lower than of N339[11], hence the affinity of the GnP-surface towards 1-butene molecules is substantially higher. In essence, the introduced relative coverage is depending on the temperature difference between the respective measurements but is also sensitive towards the characteristic interaction potential of the surface.
Apart from CNTs and GnPs, another recent type of fillers are carbon nanohorns (CNHs) and as an example for non-carbon-based fillers the nano-clay CLOISITE 116 was analysed. From the nitrogen adsorption isotherms (see figure 4.25) two unique features are apparent: (i) CNHs

[8] For nitrogen this ratio is ≈ 1.44, whereas for 1-butene the ratio changes to ≈ 0.8

[9] As discussed in section 2.2.1, the desorption rate depends on temperature: $k_{des} = 1/\tau = (1/\tau_0)exp\{-Q/RT\}$, hence increases with temperature.

[10] A temperature difference of $\Delta T = 30$ K leads to a change of relative coverage of ≈ 80 %.

[11] Both measured at the same temperature T=266.89 K.

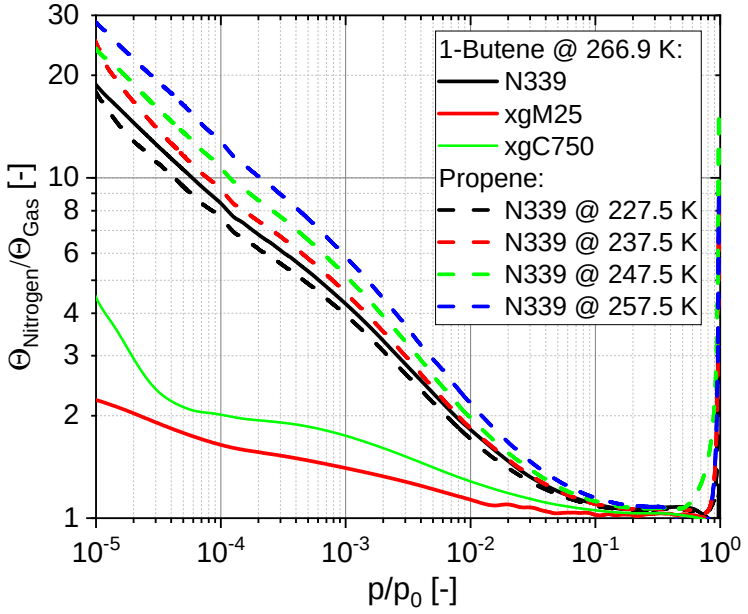

Figure 4.24.: Comparison of the relative surface coverage (the ratio of coverage between nitrogen and the used gas [here 1-butene and propene]) of N339 with two types of GnP. The dashed lines show relative coverages for propene adsorption on N339 for varying temperatures.

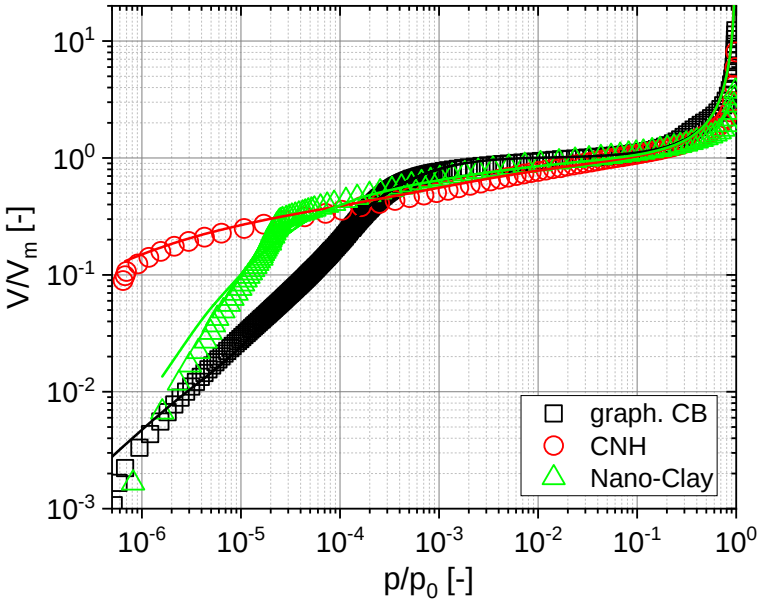

Figure 4.25.: Nitrogen adsorption (T=77K) of different filler materials - graphitized CB, carbon nano-horns and nano-clay CLOISITE 116. Lines indicate the calculated isotherms using the energy-distribution depicted in figure 4.26.

show a very linear adsorption curve, i.e. the surface is filled with constant rate[12] and (ii) the

[12]It can be described by a single power law over a wide pressure range.

nano clay shows a distinct kink at $p/p_0 \approx 2 \cdot 10^{-5}$, where a steep curve shows a rapid transition into a flat shaped curve. Similar to GnPs, the CNHs show a very high surface activity, which is reflected also in the rather high amount of high-energy sites in the energy-distribution function (see figure 4.26). A main structural element of CNHs are tubules of about 40-50 nm length with a diameter of 2-3 nm, which are ended by a five-pentagon conical cap.[38] These tubules alone would have a similar characteristic as CNT, hence there needs to be an important additional structure. In fact these tubules associate with each other and form structured aggregates with a diameter of 80-100 nm and have typically a bud-like shape.[142] Thus, there are many edges, cavities and conical holes that form a overall very fissured, heterogeneous surface structure.
The kink in the adsorption curve of the nano-clay is possibly caused by nano-pores formed by tetrahedral-shaped silicate structures, which are completely filled after reaching the pressure of the kink. However, theses examples should just give a very brief inside into the field of differently shaped filer materials. Focus of this work will be typical carbon blacks with modification on different length-scales. Up to this point, only the smallest possible length-scale, i.e. probing

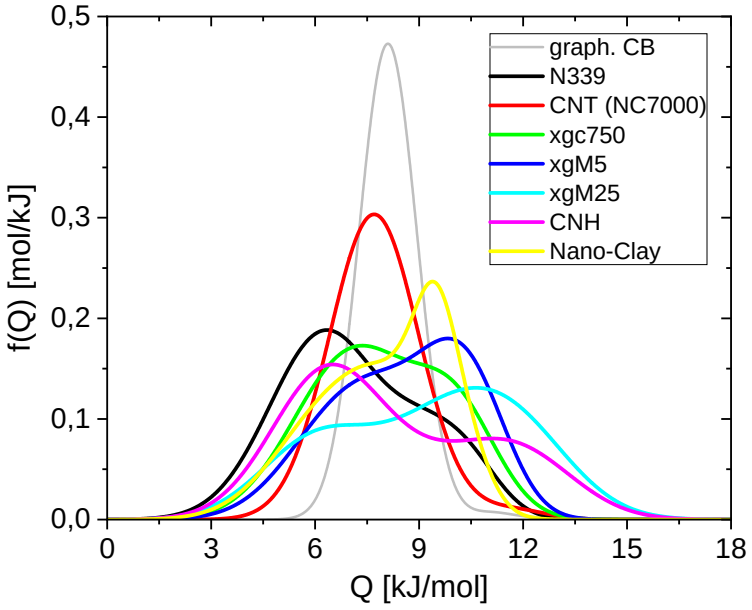

Figure 4.26.: Energy-distribution function for graphitized CB, CB, CNT, different graphenes, carbon nano-horns and nano-clay CLOISITE 116.

the surface with single molecules to access the energetic profile of the material, has been analysed. However, there is also a larger length-scale available to investigate. Therefore, the fractal FHH plot for the discussed carbon-based materials will be analysed in the following part. In section 4.1.1 the morphology of energetically very homogeneous surfaces like graphitized CB have been discussed and revealed rather small surface roughness values – based on the evaluation of the transformed FHH plot. However, for the energetically very active surfaces like GnPs or CNHs, figure 4.27 yields also a very rough surface (e.g. $D_S = 2.8$ in case of xgM25) for these materials. Taking into account that a fractal dimension $D_S = 3$ characterises an infinitely rough surface, the found values for the GnPs should be questioned critically with respect to their physical meaning. Indubitable the CNHs will have a very jagged surface morphology hence the found value of $D_S = 2.6$ could be realistic.

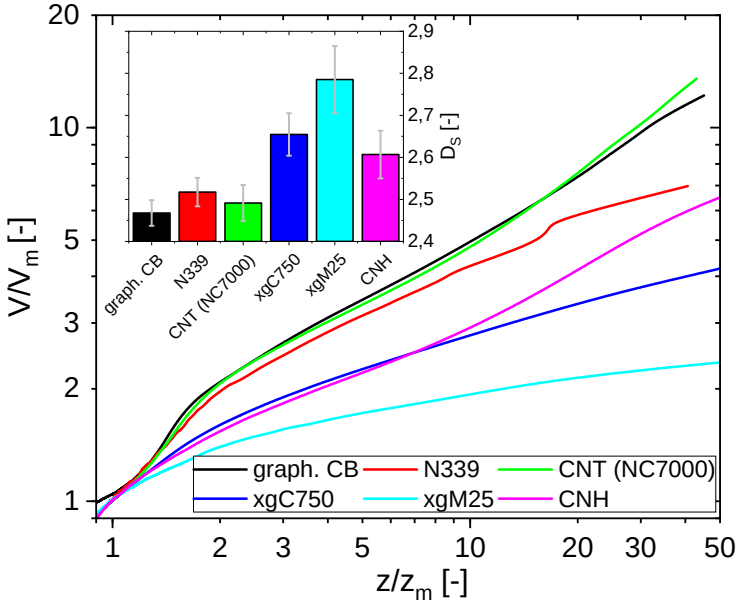

Figure 4.27.: Fractal FHH plot of graphitized CB, CB, CNT, different Graphenes and carbon nanohorns for nitrogen (T=77 K) adsorption. The inset shows the fractal dimension D_S yielding from the scaling in the range $2 < z/z_m < 10$ according to equation 2.31.

Furthermore, the values found for the CNTs are in an expected range, i.e. similar to graphitized CB and N339. Nevertheless, values beyond $D_S = 2.7$ are most likely artefacts of superimposed, secondary effects. Especially the capillary condensation will dominate the adsorption at these relative pressures[13], which can cause the theoretical prediction based on equation 2.32 to become invalid.[14] In case of 1-butene adsorption the trend is very similar to nitrogen, i.e. the roughness of all GnPs is on similar level. Interestingly, the variation in the surface fractal dimension comparing both gases is much higher for the CB and the graph. CB compared to the graphenes. This effect supports the hypothesis of an overall very high affinity of the graphene-surface towards 1-butene molecules as discussed for the relative coverages observed in figure 4.24.

[13]Typically very close to the saturation vapour pressure p_0, hence $p/p_0 \approx 1$.

[14]There could be additional terms in (2.32) becoming important for these fissured surfaces, which scale differently than $1/z$ with the distance z. Therefore, it is likely an overestimation or upper limit of the fractal dimension.

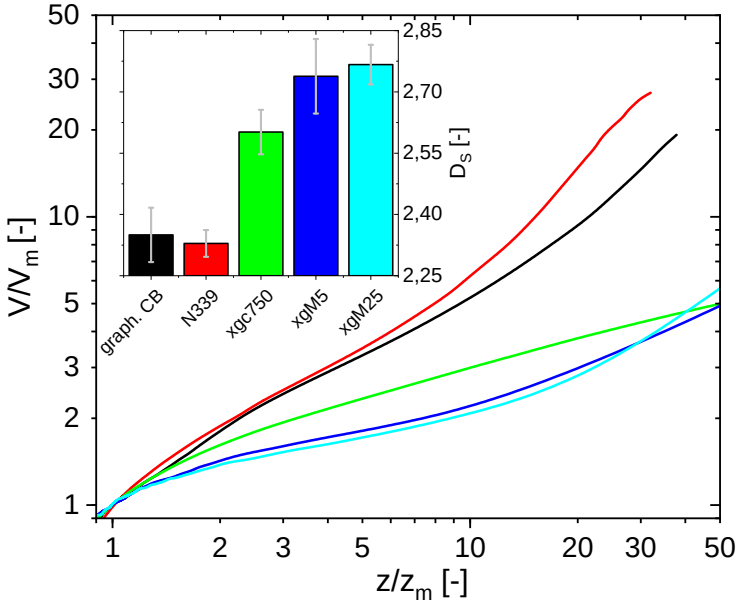

Figure 4.28.: Fractal FHH plot of graphitized CB, CB and different GnPs using 1-butene (T=266.89 K). The inset shows the fractal dimension D_S yielding from the scaling in the range $2 < z/z_m < 10$ according to equation 2.31.

4.2. Analysis of Fractal Structures of Filler Aggregates using TEM-Images

With this section a transition in the investigated length-scale is necessary. In the previous section, the surface was determining the scale at which effects were observed. Thus, when mixing polymers and fillers, the resulting interface[15] will influence the interphase and therefore the polymer-filler interaction. However, changes on a larger scale, i.e. changing the structure of filler-aggregates, will also lead to observable differences that will determine the macroscopic properties. Hence, an appropriate method for analysing these larger structures is needed. One possible tool is the transmission electron microscope (TEM), which covers a wide range of length-scales for the purpose of analysing filler aggregates or agglomerates respectively.
In the following subsections, TEM images of filler aggregates will be analysed and the results will be discussed. Two different filler types have been used: (i) N550 and (ii) Ecorax S247. The latter shows an increased structure (based on the typical oil absorption number DBP) while having a similar BET-specific surface area (see table 3.1) compared to the former. Both CBs have been incorporated into an EPDM matrix (The recipe can be found in table 3.3.). In the case of S247, TEM images of two filler levels (20 and 50 phr) have been taken into consideration. However, for the N550, only a filler level of 50 phr was measured with TEM.

In figure 4.29 one example of several hundred TEM-pictures is shown. To separate the aggregates, all samples have been swollen[16] and afterwards dried before the TEM preparation was

[15] In section 4.3 an example for modifying the interface will be discussed.
[16] A solvent can enter the polymer matrix, which leads to an equi-triaxial elongation of the sample.

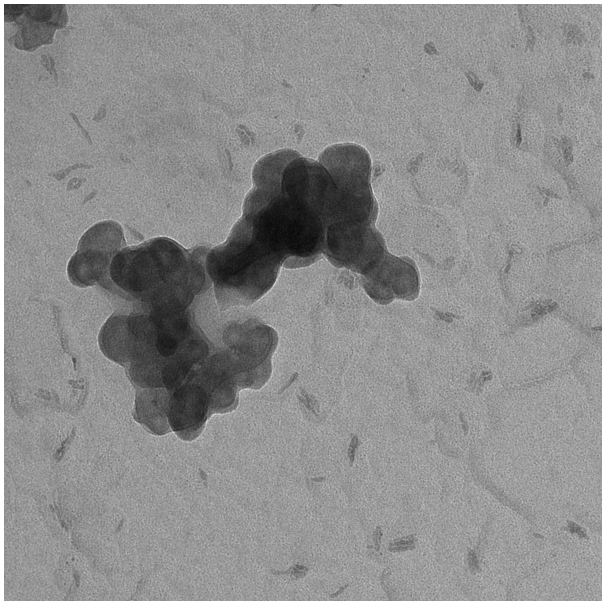

Figure 4.29.: Representative of more than 500 TEM-images of Ecorax S247 in a swollen state of an EPDM-matrix filled with 50 phr.

done. A detailed description of how the TEM images have been analysed including some examples of code segments about how to calculate the relevant properties of an aggregate can be found in appendix A.2.

4.2.1. Definitions of cluster size ξ

Characterizing fractal objects like filler aggregates in a quantitative way is key to elucidate their implications and effects in rubber applications. Therefore, it is important to define the correct descriptors for characterizing the size and shape of these fractal objects. In section 2.3, the main theoretical tools for this purpose have been introduced. To be able to apply equation (2.37) apparently two quantities are needed: (i) The mass m and (ii) the size ξ of the object. The former is not directly accessible, hence only indirect measures using the cross-sectional area A_S and perimeter P by applying equations (2.38) and (2.39) are possible. However, for the cluster-size ξ there are at least three natural definitions possible: (i) The radius of gyration R_{gyr}[17], (ii) the maximum radius R_{max} and (iii) a special radius of gyration - considering only the edge of a cluster - the hydrodynamic radius R_{hyd}.
These three different size-definitions are visualized in figure 4.30. All clusters, that will be characterized in the following, will represent two-dimensional projections of three-dimensional objects. Thus, the different definitions need to be understood with respect to their limitations in representing the reality. Choosing the maximum distance between two points on a cluster as its size R_{max} will obviously overestimate the dimensions of the aggregates systematically. Moreover, this effect will be especially important for significantly big clusters which leads to

[17]Defined as the average distance from the centre of mass considering all points of the sample.

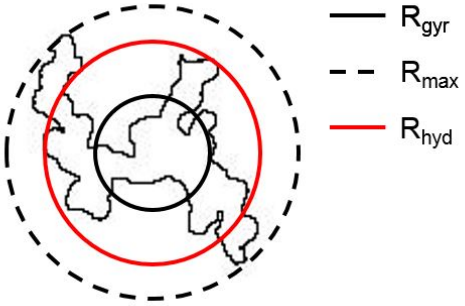

Figure 4.30.: Visualization of different definitions of cluster sizes ξ: Radius of gyration R_{gyr} (average distance of all points from the centre of mass (CM)), maximum size R_{max} and hydrodynamic radius R_{hyd} (Radius of gyration of all points forming the edge of a cluster).

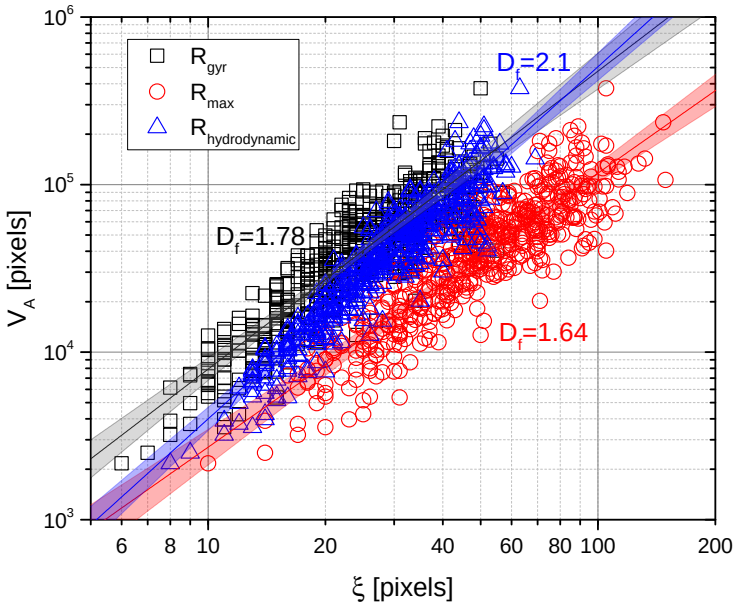

Figure 4.31.: Calculated volume of the clusters V_A according to equation (2.39) vs. different choices for cluster sizes ξ. Data from 20phr Ecorax S247 in an EPDM matrix.

an overestimation of the structure, i.e. the fractal dimension D_f will be smaller than expected. In figure 4.31 this effect can therefore be found since the fractal dimension in the case of $\xi = R_{max}$ is only $D_f = 1.64$. Taking furthermore into account that the volume of clusters V_A was calculated using equation (2.39), i.e. an overestimation of the real volume, the found value of the fractal dimension is much too low.[18]

However, picking the radius of gyration R_{gyr} as descriptor for the cluster-size ξ also leads to a rather small value – albeit already larger than in the previous case – for the fractal dimension of $D_f = 1.78$ (see figure 4.31). By definition of the radius of gyration as an average distance to the centre of mass (CM), the resulting size has to be smaller compared to the maximum distance. Thus, there is usually an underestimation of the size of the aggregate, hence the found value

[18]Choosing a lower value for the volume will most likely lead to even smaller values for the fractal dimension because especially larger clusters will be effected, hence the scaling will change accordingly.

$D_f = 1.78$ is still smaller than the theoretical value of $D_f = 1.9 - 1.95$ for ballistic aggregation processes.[19]
Since the radius of gyration weights every point of the cluster equally, it is not the best choice for describing its size properly. Consequently, just taking into account those points forming the edge of a cluster and define the radius of gyration of only these points as hydrodynamic radius, seems to be a more reasonable choice for the size of an aggregate. In figure 4.31 the resulting scaling, i.e. the fractal dimension $D_f = 2.1$ is much closer to the expected value than both previous discussed values. Especially investigating the position of the results for the hydrodynamic radius in relation to the other two possibilities, reveals an explanation for the good match of the fractal dimension. Neither is the hydrodynamic radius underestimating the small clusters nor is it overestimating the size of larger ones. Rather are the points in the case of small sized aggregates closer to the R_{max} values[20] and for the larger clusters closer to the results of R_{gyr}[21].

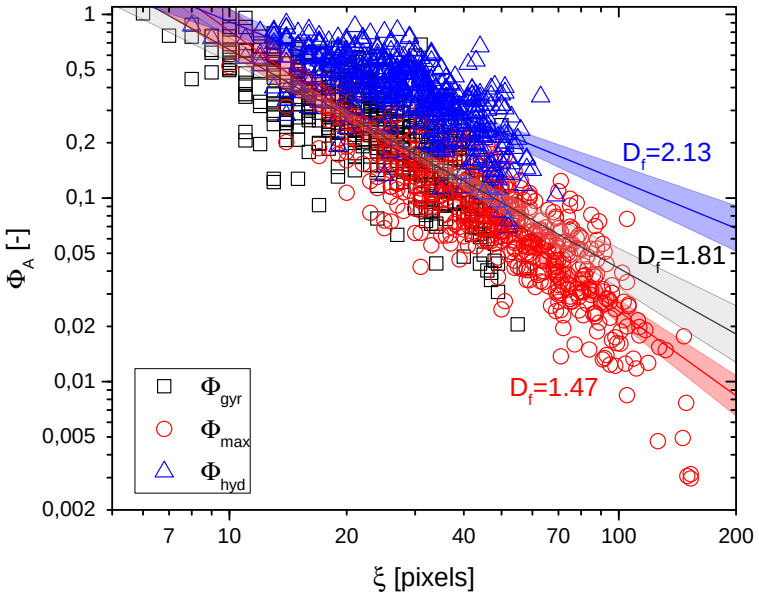

Figure 4.32.: Influence of the choice of cluster size ξ on the solid volume fraction Φ_A calculated by using equation (2.40) with three different choices of radius ξ: Here $\Phi_{gyr} = \Phi_{R_{gyr}}$, $\Phi_{max} = \Phi_{R_{max}}$ and $\Phi_{hyd} = \Phi_{R_{hydrodynamic}}$ in the case of 20 phr of S247 in EPDM.

This result can be emphasized by examination of the solid volume fraction Φ_A defined as the ratio between (an estimated) volume of the cluster V_A and a sphere around it (see section 2.3, equation (2.40)). Obviously, the definition of the sphere around the cluster is again depending on its size ξ, since there are three definitions for the size, there are also three different choices for the solid volume-fraction $\Phi_A = \Phi_{R_{gyr}}$, $\Phi_A = \Phi_{R_{max}}$ and $\Phi_A = \Phi_{R_{hyd}}$ respectively. The resulting values are depicted in figure 4.32 as a function of the corresponding cluster size ξ. Consequently, again the best match for the fractal dimension $D_f = 2.1$ is found for $\Phi_{R_{hyd}}$ vs.

[19] Now especially the effect of small clusters leads to the wrong scaling.
[20] Since these are less structured, therefore the maximum distance will be close to the R_{hyd} value.
[21] Since these are more likely structured, thus the maximum distance can be much larger than R_{hyd}

R_{hyd}. Moreover, the found values for Φ_A in the case of R_{max} are too small ($0.5 < \Phi_{R_{max}} < 0.002$) and for $\Phi_{R_{gyr}}$ even values greater than unity can be found. Henceforth, the hydrodynamic radius R_{hyd} will be used as the cluster size ξ.
A next step is to compare the cluster size distributions for different systems. First, a sample filled with high structured S247 below percolation threshold, secondly a sample with the same filler type but above percolation volume fraction and finally a sample with the same filler level as the latter but with a low structured N550 have been analysed. In figure 4.33 the resulting

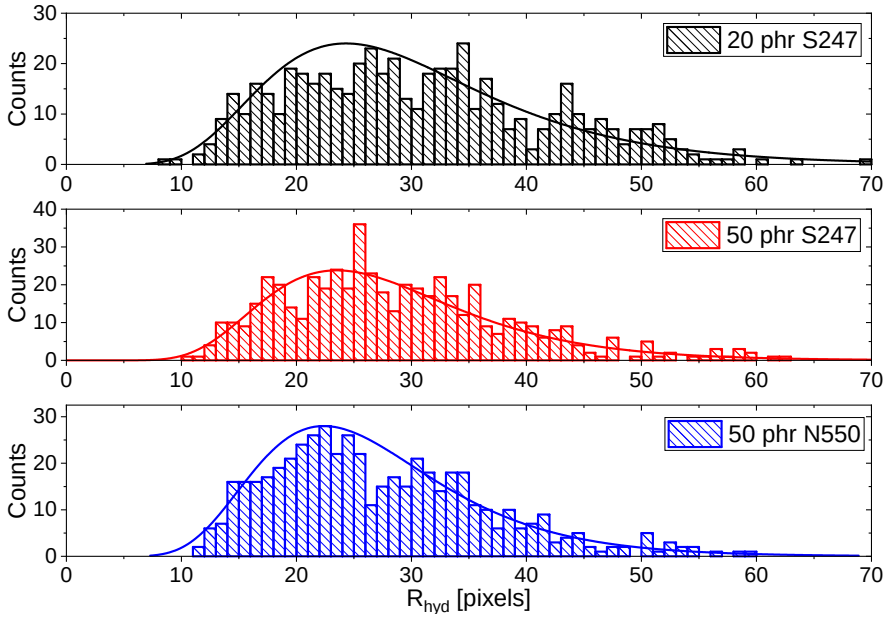

Figure 4.33.: Cluster size distribution for three different samples: top - 20 phr of S247, center - 50 phr of S247 and bottom - 50 phr of N550, all in EPDM. The lines indicate a fit using the log-normal distribution.

histograms of the sizes are depicted. All images are scaled equally, such that 10 pixels are approximately representing 50 nm in reality. Therefore, all cluster size distributions start at a value of about 10 pixels, i.e. 50 nm, which is characteristic for these types of CB as their primary particle size. Usually the smallest unit in rubber compounds are primary aggregates, which by definition are not breakable. Nevertheless, there is always a small probability to find primary particles or aggregates, which only consist out of few primary particles.
However, the average aggregate size for the low filled sample is roughly 150 nm. Increasing the filler level shifts the average value towards smaller sizes ($\approx$ 120 nm). This effect is most likely explained by increased shear forces during the mixing process, which will break down bigger clusters more often. Moreover, also the width of the distribution is decreased by an increased filler level - again showing a better micro-dispersion due to higher energy input during mixing. A comparison of the two latter samples[22] doesn't show significant differences in the distribution of the aggregate sizes. Thus, a more thoroughly performed analysis is needed to explain the differences between these two samples.[23]

[22] 50 phr S247 vs. 50 phr N550

[23] In section 4.4.2 mechanical data will be discussed in more detail. An observation was, that the S247 in EPDM shows always an improvement in mechanical strength and energy dissipation until 50 phr of filler level was

4.2.2. Determining the fractal dimension of different aggregates

In this subsection the aforementioned scaling relation between the mass, i.e. the volume of an aggregate and its size, expressed in equation (2.37), will be applied to all three samples, to extract their respective fractal dimension D_f. The previous subsection explained why the hydrodynamic radius R_{hyd} was chosen as cluster size ξ. However, the mass m or volume V are more difficult to access. As discussed in section 2.3 there are two easily applicable methods available to calculate the volume from a two dimensional picture. Both methods are only valid under certain assumptions, hence can only serve as approximations. In particular, the method of Herd et al. [53] using equation (2.39) only will give an upper limit of the volume. Whereas the method of Meakin et al. [117], using equation (2.38), is mostly an underestimation of the real volume. Taking into account these boundary conditions for both methods, an assessment

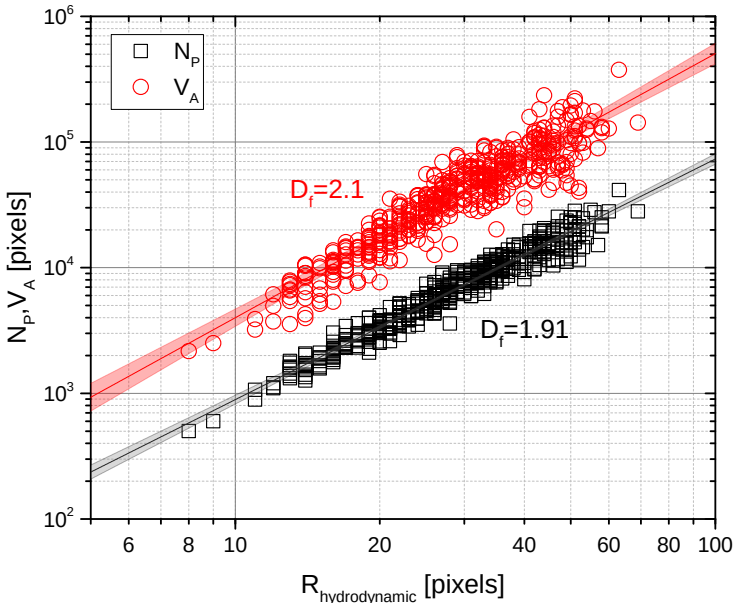

Figure 4.34.: Number of particles and volume of 20 phr Ecorax S247 clusters vs. their size (here the hydrodynamic radius) mixed in EPDM.

of the resulting scaling relations, i.e. the fractal dimensions is nevertheless possible. In figure 4.34 the first sample is analysed accordingly. For this low-filled compound the method of Herd gives a fractal dimension of $D_f = 2.1$ whereas the other method only yields $D_f = 1.91$.
Typical aggregation processes in a CB reactor are assumed to be under ballistic conditions, hence a fractal dimension of $D_f = 1.9 - 1.95$ is expected. Therefore, the Meakin method is giving a very reasonable number. However, considering all the processes previous to capturing the TEM image, like mixing of the compound, curing and afterwards the sample preparation including swelling of the sample, the resulting fractal dimension will most likely be higher than the expected ballistic aggregation value. During the process of mixing, mechanical forces will successively break down large clusters until theoretically[24] only non-breakable primary aggregates are present. In reality there will always be secondary or higher order aggregates present, which can be highly structured (leading to a lower value of D_f) or more compact (higher value

reached. Then the advantage of S247 was vanishing or was even a disadvantage.
[24] Assuming a perfect micro-dispersion.

of D_f). After mixing, samples are prepared via curing in a press. Before the actual cross-links will be formed (via a reaction of either sulphur or peroxides), the filler aggregates can form larger clusters due to flocculation processes.
Below the percolation threshold, only larger clusters but no filler network structure will be formed. In essence, there are processes that will reduce the fractal dimension (like flocculation of highly structured aggregates) and occurrences that will rather increase the fractal dimension. In case of the sample depicted in figure 4.34, both mechanisms (build-up and break-down of structures) will be of minor importance due to the low filler amount that leads to fairly small shear forces during mixing as well as to little flocculation effects. In general for typical compounds, the mixing process will have a larger influence compared to the flocculation during curing because the cross-linking reaction starts typically after a few minutes whereas the flocculation is a long time process which will be jammed by a permanent network. Therefore, the found average value[25] for the fractal dimension $D_f = 2.0$ seems to be in very good agreement with the expectation of ballistic particle aggregation processes.

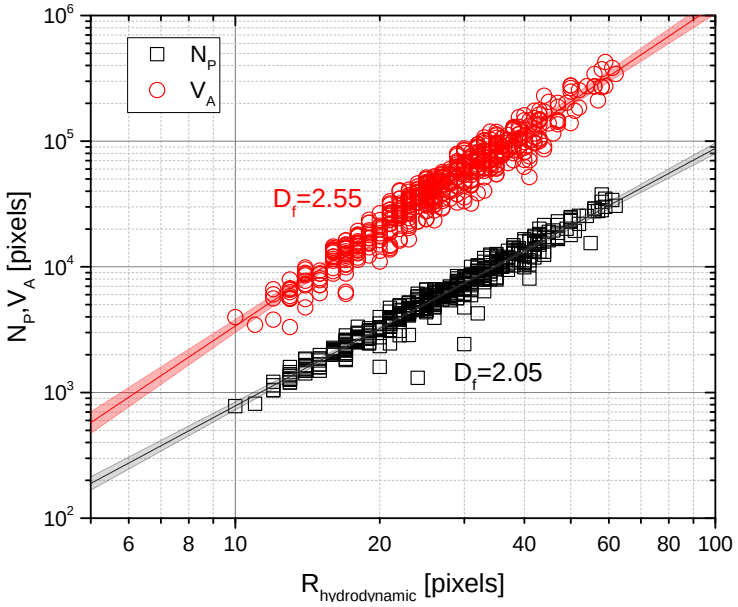

Figure 4.35.: Number of particles and volume of 50 phr Ecorax S247 clusters vs. their size (here the hydrodynamic radius) mixed in EPDM.

Investigating the samples with a higher filler level changes this agreement between both considered methods significantly. In figure 4.35 the S247 with 50 phr is depicted in a similar way. Here, the Meakin method yields a fractal dimension of $D_f = 2.05$, which is very close to the previously discussed overall value. In contrast, the method of Herd gives a very different value of $D_f = 2.55$. Such a high fractal dimension points towards very compact, i.e. much less structured aggregates. Both methods use the cross-sectional area A for calculating the volume. However, the Meakin method uses exclusively the value of A to estimate the number of particles (hence, the volume), whereas the method of Herd additionally uses the perimeter P of the clusters. While the area based method yields an increase of fractal dimension of 7.3 %, the Herd method shows an increase of 21.3 % compared to the lower filler level. Thus, the main

[25] Due to the fact that the difference between the two used methods is rather small.

difference between these two samples will be caused by changes in the perimeter-scaling.
In figure 4.36 the scaling relation between the cross-sectional area $A \propto R_{hyd}^{\gamma}$ and the perimeter $P \propto R_{hyd}^{\gamma}$ with the hydrodynamic radius R_{hyd} are depicted for both samples respectively. For

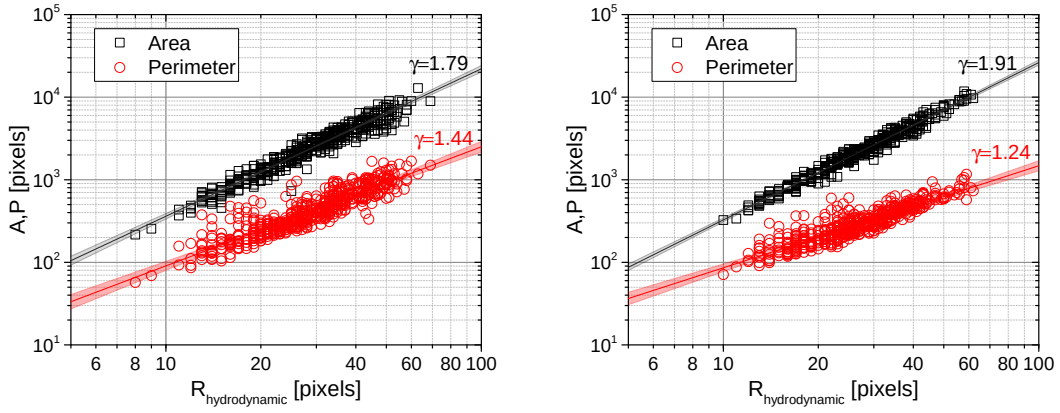

(a) 20 phr S247 (b) 50 phr S247

Figure 4.36.: Area A and perimeter P of aggregates vs. their hydrodynamic radius R_{hyd} for S247 in EPDM. The respective scaling is indicated with the exponent γ.

the area, the found scaling increases by approximately 7 % indicating slightly more compact structures. However, additionally the perimeter scaling changes by 14 % towards lower values, which explains the total change in the fractal dimension of 21 %.[26] Therefore, the method of Meakin is missing an important feature of capturing the structural change, which is found in the perimeter of aggregates. Although the method of Herd is very likely an overestimate of the aggregates' volume, it is nevertheless more sensitive to structural changes than the Meakin method. Analysing the third sample accordingly (see figure 4.37), reveals a similar scaling of the area compared to the 50 phr S247 sample but a much larger value for the exponent is found in case of the perimeter scaling. Thus, there are more highly structured aggregates found for the sample filled with 50 phr N550. Unsurprisingly, the found overall fractal dimension for this sample (see figure 4.38) is in case of the Herd method smaller than for the 50 phr S247 sample. Also the similar value for the Meakin method is already visible in figure 4.37 from the scaling of the cross-sectional area.
As discussed already in the previous subsection, calculating the solid volume fraction Φ_A using equation (2.40) often reveals more insights than the pure volume-size relation. In figure 4.39 a comparison of the S247 sample filled with 20 phr and 50 phr are shown respectively. Using this representation, the above discussed big difference in the aggregate-structure due to the higher filler loading becomes even more obvious. Since the value of Φ_A represents the ratio of the estimated value of the volume to the volume of a sphere with size ξ, more compact structures will lead to higher values of Φ_A[27] whereas highly structured clusters yield much lower numbers. Comparing clusters of equal size for both samples exhibits very different volume fractions. For

[26] According to equation (2.39) the volume scales with $V_A \propto \frac{A^2}{P}$, hence an increase in A- and a decrease in P-scaling, overall increases the scaling ($= D_f$) of V_A.
[27] A sphere will consequently lead to the limiting value of $\Phi_A = 1$, which is in these examples represented by the primary particles.

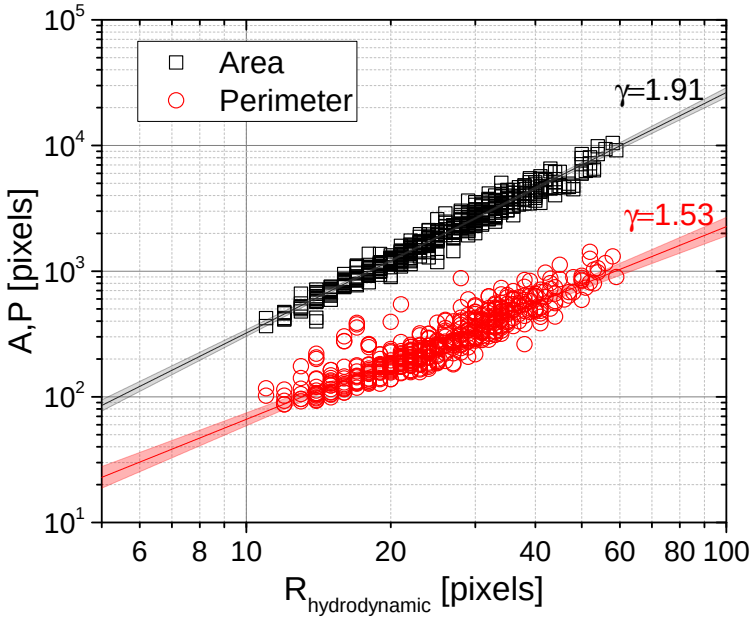

Figure 4.37.: Area A and perimeter P of aggregates vs. their hydrodynamic radius R_{hyd} for 50 phr N550 in EPDM. The respective scaling is indicated with the exponent γ.

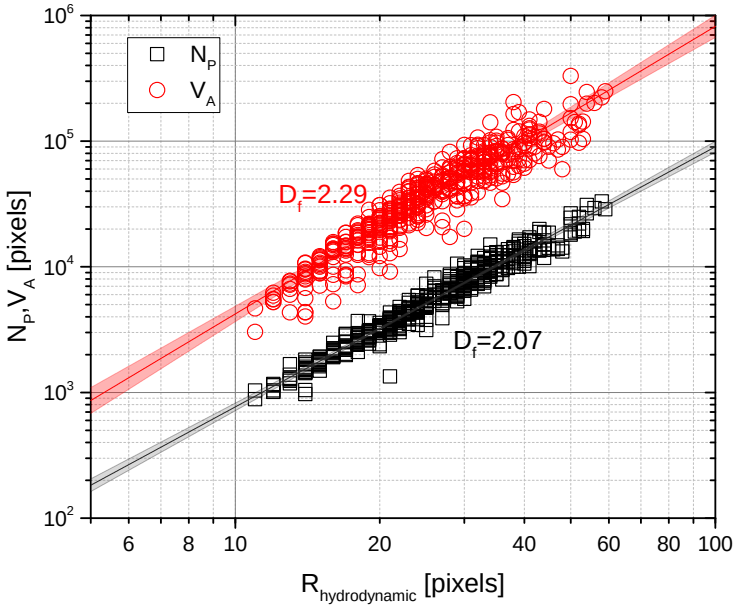

Figure 4.38.: Number of particles and volume of 50 phr N550 clusters vs. their size (here the hydrodynamic radius) mixed in EPDM.

instance clusters with a size of 50 nm in case of the S247 filled with 20 phr leads to values of $0.1 < \Phi_A < 0.3$, while the highly filled sample yields values of about $0.3 < \Phi_A < 0.6$. Most of this breakdown of aggregate-structure will occur during the mixing process. With higher filler loading, the shear forces inside the compound are increased, since more energy is needed to

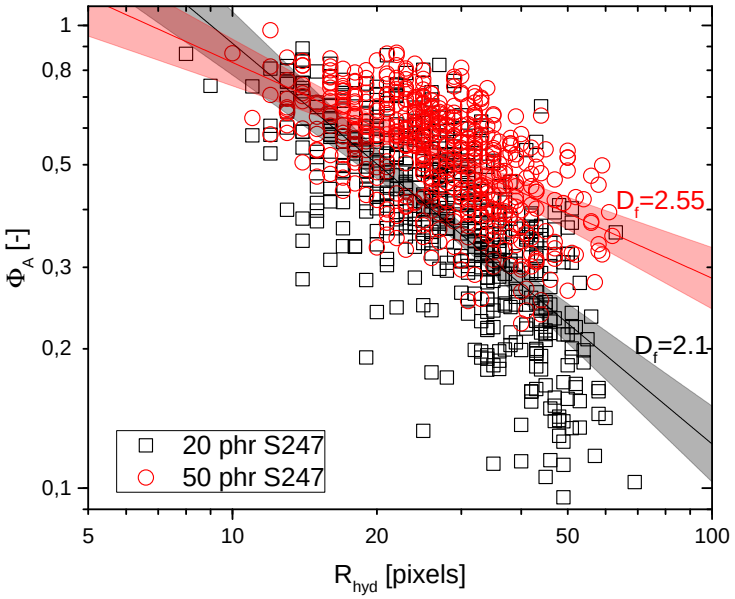

Figure 4.39.: Solid volume fraction Φ_A (equation 2.40) using the hydrodynamic radius R_{hyd} as cluster size for S247 in EPDM. Fractal dimension D_f calculated via $\Phi_A \propto \xi^{D_f-3}$.

separate larger agglomerates. However, the filler fraction alone cannot explain this breakdown. In figure 4.40 the two types of CB are compared with respect of their solid volume fraction Φ_A.

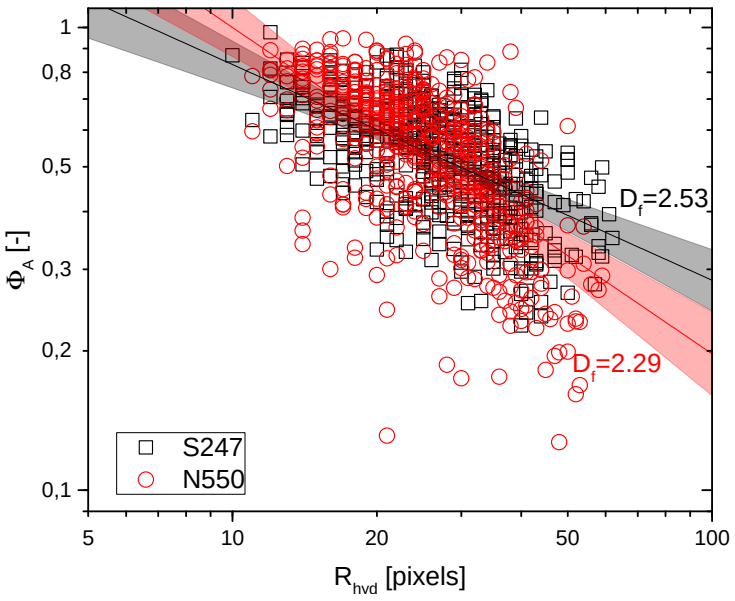

Figure 4.40.: Solid volume fraction Φ_A (equation 2.40) using the hydrodynamic radius R_{hyd} as cluster size for the highly filled (50 phr) samples of S247 and N550 in EPDM. Fractal dimension D_f calculated via $\Phi_A \propto \xi^{D_f-3}$.

For N550 the volume fraction Φ_A at 250 nm sized aggregates[28] is still lower ($0.13 < \Phi_A < 0.35$) than for S247. Thus, the structural-breakdown inside the mixer is especially pronounced for the S247. Since the S247 was developed for having a higher structure compared to the N550, this advantage leads to an accelerated loss of just its structure. This mechanism of auto-amplification of structure-loss obviously occurs above a threshold value of filler level.[29] Additionally to these differences at larger cluster sizes, there is an overall different shape of the cloud of points.[30] For the purpose of quantifying this difference, an analysis of the distribution of Φ_A-values is depicted in figure 4.41. First of all, the mean values for the high and low filled samples differ

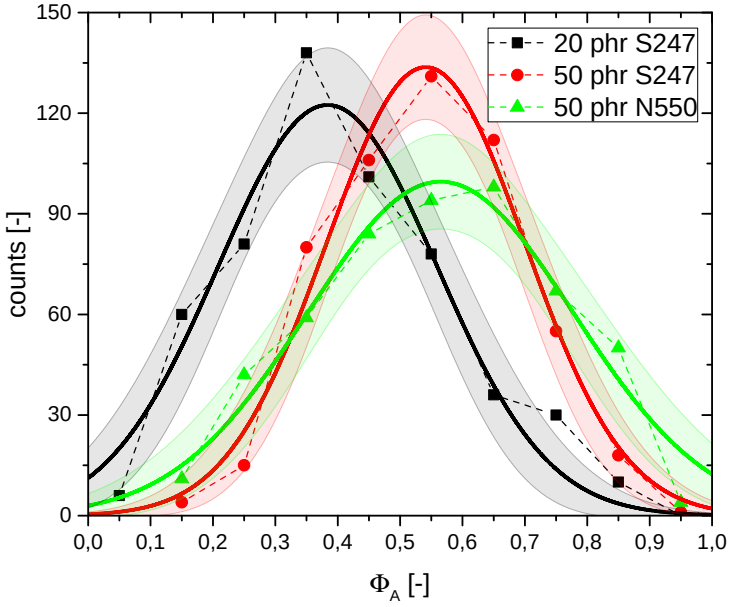

Figure 4.41.: Histogram of solid volume fraction values Φ_A for all three samples. The data was fitted by a Gaussian distribution function (including 95 % confidence bands).

significantly. The 20 phr filled sample yields an average value of $\langle \Phi_A \rangle = 0.38$. For the highly filled samples $\langle \Phi_A \rangle = 0.54$ and $\langle \Phi_A \rangle = 0.56$ can be found for the S247 and N550 respectively. Thus, on average the clusters for the S247 and N550 have the same solid volume fraction. This fact shows, that for the mechanically relevant effective volume fraction Φ_{eff} in equation (2.41) the denominator is not the number average of Φ_A but the second moment, i.e. a weighted average, amplifying the effect of larger ξ-values. In section 4.4.2 the effective filler volume fraction will be calculated using the mechanical material model DFM (see section 2.4.3) and these values will be compared to those from TEM image analysis discussed here.[31]

[28] 50 pixels

[29] This threshold will probably be closely related to the mechanical percolation threshold, which defines the transition between hydrodynamic amplification and a superstructure forming a filler-network.

[30] It should be noted, that the overall uncertainty is larger compared to the volume-size plots. This effect is caused by the calculation of Φ_A, which includes the error of both the volume V_A and the cluster size ξ.

[31] See figure 4.62.

4.3. Rheological Characterization of Compounds to Investigate the Polymer Filler Interaction

In this section the effect of an ionic liquid treated surface will be analysed in rubber compounds. Focus will be the elucidation of relations between structural characteristics on nano-scales (section 4.1) and the resulting mechanical- and dielectric properties of the samples on the macro-scale.
For this purpose, non-cured compounds will be investigated in special combined rheological-dielectric experiments. Especially focussing on different types of polymers with varying polarities to understand the nature of polymer-filler coupling mechanisms. Since in cured rubber compounds several different networks exist[32], and hence influence each other, it is reasonable to investigate non-vulcanized samples in order to switch off the effect of chemical cross-links and thus focus on the effects of polymer-filler coupling. Therefore, rheological measurements described in section 3.4 have been performed using the measurement profile depicted in figure 4.42. The whole experiment can be divided into six different sections as indicated in figure 4.42, where various effects can be observed. This section is therefore organized in three major

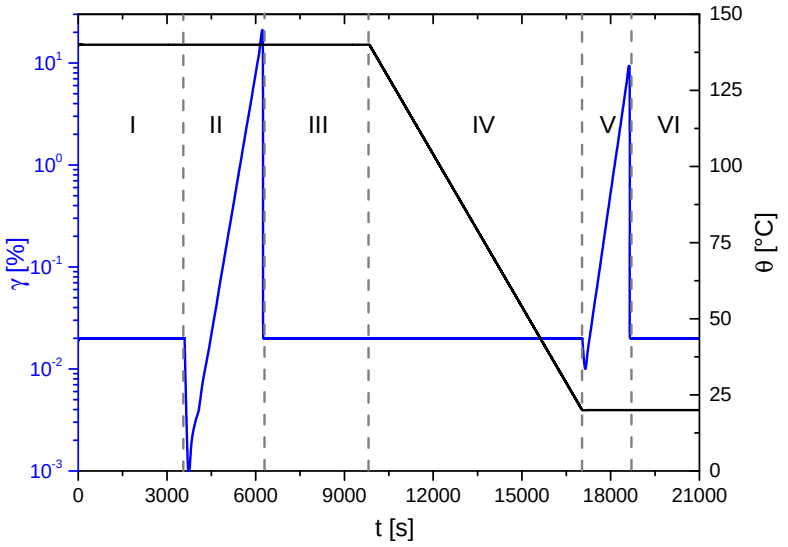

Figure 4.42.: Measuring profile for flocculation and strain sweep experiments at different temperature. Right axis indicates the dynamic amplitude γ and the right axis shows the temperature. I: Initial Flocculation at 140 °C; II: Strain sweep at 140 °C; III: Re-flocculation at 140 °C; IV: Cooling down at low amplitude to room temperature; V: Strain sweep at room temperature; VI: Relaxation at room temperature

subsections. Within the first part, the process of filler-network formation will be discussed (see part I, III and VI in figure 4.42), followed by an investigation of its breakdown (see part II and V in figure 4.42) and finally the influence of temperature (see part IV in figure 4.42) will be analysed. Each subsection compares data from three types of polymers: (i) Natural rubber (NR

[32] Additional to the intrinsic polymer entanglement network, there is the filler network if the filler level is above the percolation threshold. Finally there is the chemical network due to curing reactions of sulphur or peroxides, interconnecting polymer chains.

- see figure 3.1a; using the recipe shown in table 3.2.), (ii) nitrile butadiene rubber (NBR - see figure 3.1c; using the recipe 3.4) and (iii) hydrogenated nitrile butadiene rubber (HNBR - see figure 3.1b;: using the recipe 3.4).[33]

4.3.1. Combination of Rheological and Dielectric Measurements for Various Polymer Systems using Surface-Modified Carbon Black Part I: Filler-Flocculation

Within the initial part of the experiment depicted in figure 4.42, filler flocculation at a small strain amplitude and high temperature is observed as discussed previously in the initial part of section 2.4.2.

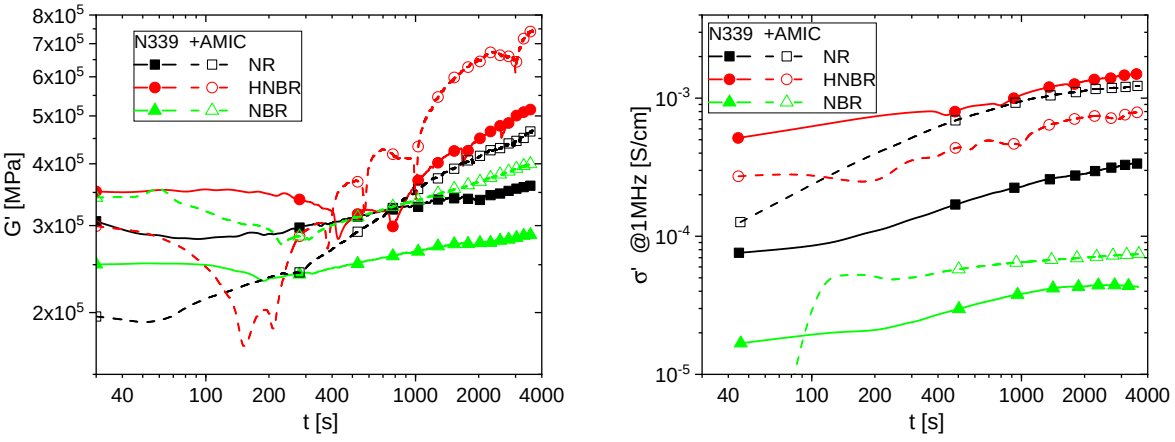

(a) Mechanical flocculation

(b) Dielectric flocculation

Figure 4.43.: Flocculation experiment at 140 °C for all polymers (color code as indicated) filled with 50 phr of N339 with (filled symbols) and without (open symbols) modification of AMIC. (a): Storage modulus G' and (b): Real part of the conductivity σ' at a frequency of 1 MHz.

In figure 4.43 the build-up process of a filler network is shown as a function of time. Especially two parameters are measured simultaneously: (i) The mechanical (storage) modulus G', i.e. the material stiffness at a respective frequency[34] (see figure 4.43a) and (ii) The electrical conductivity (see figure 4.43b), thus the dielectric response of the sample at different electric frequencies.[35]
Especially at elevated temperatures, filler aggregates will form larger agglomerates induced by entropic depletion forces. Hence, the average distance between two aggregates will decrease with time, thus the mechanical modulus will increase due to a stiffening of filler-filler bonds

[33] Here, the filler level of N339 is always 50 phr.
[34] Here always constantly 1 Hz.
[35] Henceforth, all conductivity values are taken at an electric frequency of 1 MHz to increase the signal to noise ratio and to reduce the influence of a bad contact between the sample and electrode, which could induce electrode-polarization effects.

mediated by a thin layer of confined polymer at the filler surface. Therefore, also the conductivity shows qualitatively a similar trend since the ability for charge carriers to move through the material will increase due to the reduced filler-filler gap-distance and the overall higher number of filler-filler contacts.
In case of NR, figure 4.43a indicates a much faster increase with time for the AMIC-modified surface. Thus, the mechanism of flocculation is strongly depending on the polymer-filler coupling. In section 4.1.2 the filler surface, i.e. the interface between particle and polymer-monomers was analysed focusing on the energetic characteristics. It was found, that deploying ionic liquid molecules onto the filler surface, decreases its activity[36] via blocking of mostly high-energy sites of the surface.[37]
Taking this into account, the observed differences in the flocculation behaviour (see NR curves in figure 4.43a) show the expected behaviour: By decreasing the amount of energetically high active sites, the polymer-filler interaction is reduced in its strength. Hence, at elevated temperatures, it becomes easier for filler aggregates to push polymer chains aside while moving through the matrix. This movement is directly influenced by adjacent filler particles due to entropic depletion forces.[38] Consequently, the build-up of a filler-network will be accelerated in the case of an decreased polymer-filler interaction, thus the modulus increases faster in the NR-AMIC system. Furthermore, this reduced coupling results in smaller average filler-filler distances, in which polymer chains will be confined, thus the conductivity will be increased accordingly.
However, comparing the flocculation curves for the NBR, which mainly differs from NR by its polarity, shows a less pronounced influence of the AMIC modification especially in case of the mechanical stiffness. While the NR shows a significantly different slope between unmodified and modified surface, the NBR curves are much more similar to each other. Moreover, the conductivity shows an overall smaller value compared to the NR and there is no significant difference between the modified and non-modified sample.[39]
In case of the hydrogenated NBR (HNBR), the qualitative behaviour of the mechanical network formation process is similar to both other polymers since the modulus in case of AMIC rises faster and is therefore on a higher level. However, the conductivity does show a unique behaviour by being smaller in case of the modified surface. This effect supports the hypothesis of an overall weak polymer filler interaction between HNBR and N339 since the average filler-filler gap distance is reduced, hence there is an overall higher conductivity. With the addition of AMIC, the interaction is then even enhanced (see figure 4.45b), therefore there is more polymer bound to the interface, thus the conductivity is reduced.
These polymer-specific flocculation characteristics are especially apparent in the re-flocculation stage[40] (after the first break-down discussed in the next sub-section) depicted in figure 4.44. For a better comparison, the curves have been quantitatively analysed applying a simple power law dependency of the modulus $G' \propto t^{\alpha}$ and the conductivity $\sigma' \propto t^{\beta}$ with time t. The respective slopes, i.e. the exponents α and β are summarized in table 4.1.

[36] Since only non-polar gases could be used, also only the activity of the dispersive part of the surface decreases. Hence, there is no information about the polar part of the surface.
[37] See the energy-distributions depicted in figure 4.18
[38] See section 2.4.2 for more details.
[39] Although the general trend of an reduced conductivity in case of AMIC is also valid in case of NBR
[40] Since the state of the material after mixing and pre-treatment is not fully comparable (e.g. due to not fully relaxed normal stresses in the material) the state after the first strain sweep is well defined and will lead to more reliable results.

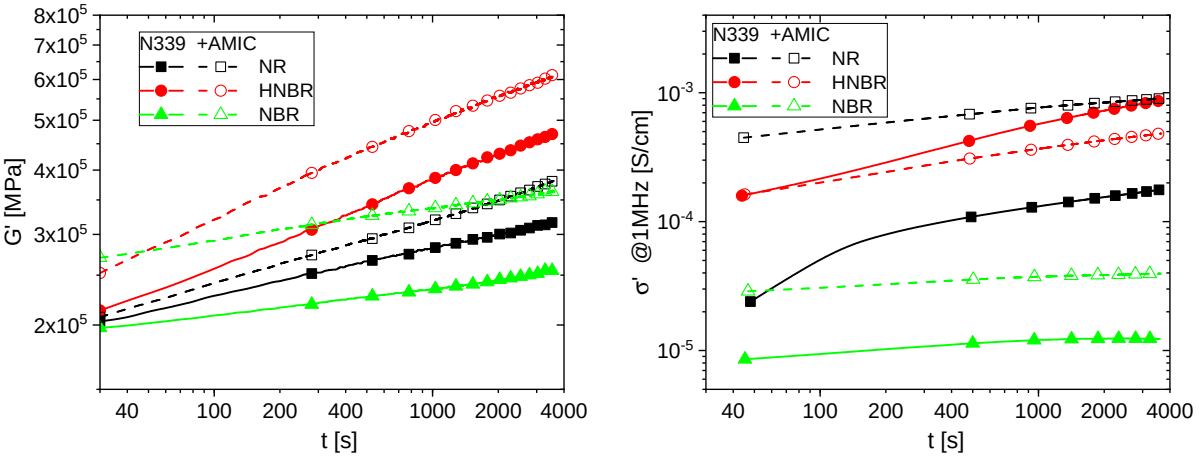

(a) Mechanical flocculation

(b) Dielectric flocculation

Figure 4.44.: Re-flocculation experiment, i.e. after a conditioning strain sweep (see subsection 4.3.2), at 140 °C for all polymers (color code as indicated) filled with 50 phr of N339 with (filled symbols) and without (open symbols) modification of AMIC. (a): Storage modulus G' and (b): Real part of the conductivity σ' at a frequency of 1 MHz.

Table 4.1.: Summary of all scaling-exponents following a power-law relation for the modulus $G' \propto t^{\alpha}$ and the conductivity $\sigma' \propto t^{\beta}$ for both flocculation tests (initial and re-flocculation) at 140°C for all systems NR, NBR and HNBR respectively. All values including the given errors are from a linear fit at larger times.

	α [-]		β [-]	
System	initial	re-flocculation	initial	re-flocculation
NR+N339	0.1 ± 0.001	0.09 ± 0.001	0.3 ± 0.006	0.22 ± 0.0003
NR+AMIC	0.19 ± 0.004	0.15 ± 0.0006	0.13 ± 0.005	0.12 ± 0.0005
NBR+N339	0.05 ± 0.001	0.06 ± 0.0005	0.09 ± 0.007	0.01 ± 0.0016
NBR+AMIC	0.13 ± 0.0006	0.06 ± 0.0005	0.11 ± 0.0006	0.04 ± 0.0005
HNBR+N339	0.26 ± 0.008	0.16 ± 0.0005	0.24 ± 0.007	0.3 ± 0.0007
HNBR+AMIC	0.21 ± 0.02	0.16 ± 0.0005	0.12 ± 0.02	0.2 ± 0.0005

The build-up process of a mechanically active network structure is most affected by the presence of a surface modification in the NR system since the exponent α is only there significantly increased. Moreover, both polar polymers show no influence of the AMIC treatment in the rate of the mechanical flocculation. However, the absolute value of the exponent α suggests already substantial differences between both polar polymers. In case of the non-saturated NBR, the flocculation rate, i.e. the exponent α, is significantly reduced in comparison to the saturated HNBR. Thus, the presence of double bonds within the polymer chain strongly affects the ability to interact with the filler surface through bonds formed via a π-π stacking mechanism. Furthermore, the value of α in case of the modified NR is almost the same as in case of the HNBR,

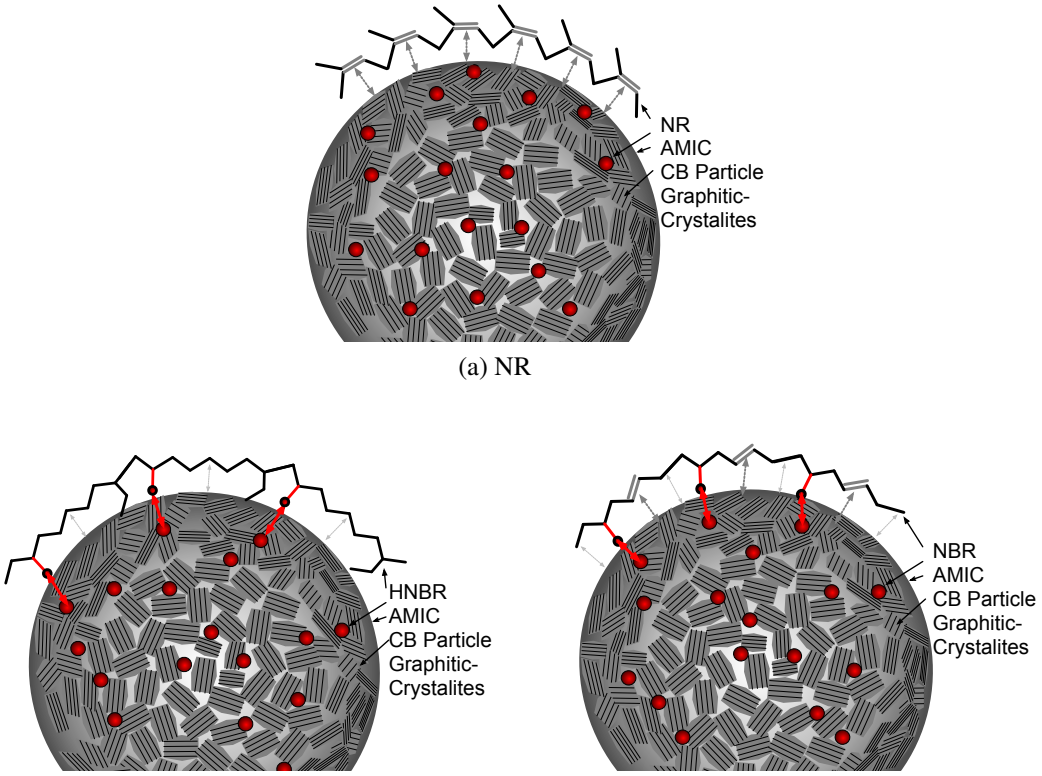

(a) NR

(b) HNBR

(c) NBR

Figure 4.45.: Sketch (Note: wrong scale) of the principle mechanism of different polymer-filler interactions. On the surface of the CB (gray sphere) are the graphitic crystallites distributed and the AMIC molecules (small red spheres) block a certain portion of them. Additionally, 3 monomers of the respective polymer types are shown with there characteristic groups (e.g. nitrile group: red part) and the double bond (highlighted in gray). The possible bonds are indicated as arrows (red=polar, dark-gray=π-π, light-gray=van-der-Waals).

indicating once again only a weak polymer-filler interaction.
The build-up of an electrically conducting network shows similar trends as well as differences between all polymers. In case of NR the effect of the surface modification leads to opposite trends in the absolute value of the flocculation exponent β in comparison to α, i.e. there is a decrease in β where there is an increase in α with AMIC. Accordingly, also the HNBR shows the same decrease in electrical flocculation speed with the addition of AMIC, albeit on a higher absolute level. In case of the NBR both exponents are on very small levels, i.e. there is very little change in the network structure with time. In figure 4.45 a simplified sketch[41] as a proposed material model is illustrated.
In both non-saturated polymers (NR and NBR) the polymer filler interaction is dominated by the aforementioned π-π stacking effect. Hence, blocking active sites of the surface disturbs this bonding-mechanism and reduces the effective polymer-filler coupling. In case of NR, this weakening is most pronounced since there is only one main bonding mechanism. In contrast,

[41]The shown sizes of the polymer and the filler are not matching, since a typical size of a primary CB particle is in the range of 10-50 nm and the monomer of a polymer chain is usually below 1 nm in length.

the polar groups of the NBR can interact with the AMIC molecules on the filler surface and therefore balance the missing π-π stacking effect. Consequently, the absence of double bonds[42] in the HNBR leads to a weak overall filler-interaction and the presence of polar groups on the surface – although blocking high-active sites – should overall increase the ability to interact with the surface. From just the mechanical stiffness this effect is not observable, however the reduced conductivity in case of the AMIC modified system supports this picture.
Obviously, from the similarities and differences between the mechanically- and electrically effective network structures, more information of the nature of the polymer-filler coupling can be extracted. To further elaborate specifically on this point, the next subsection will discuss the breakdown of the filler-network during the strain sweep in between the two previously discussed flocculation phases.

4.3.2. Combination of Rheological and Dielectric Measurements for Various Polymer Systems using Surface-Modified Carbon Black Part II: Filler-Network Breakdown

In between the two previously discussed flocculation phases, a conditioning strain sweep was performed. With increasing dynamic strain amplitude the material is exposed to rising shear stresses. These stresses are distributed over the various network structures and hence the network will undergo structural changes. In particular the break-down of the filler-network is well known for filled elastomers as the Payne-Effect. In figure 4.46 the respective curves are

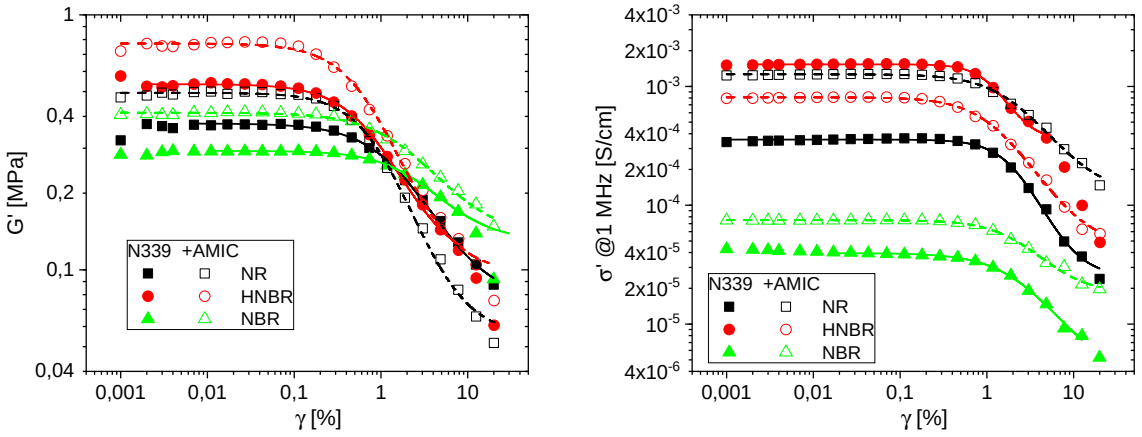

(a) mechanical break-down

(b) dielectrical break-down

Figure 4.46.: Strain sweep comparison at 140 °C for NR, HNBR and NBR with and without AMIC modification.including a fit using the Kraus-Model (see: solid- and dashed lines; According to equation 2.57).

depicted. Figure 4.46a shows the mechanical storage modulus G' and figure 4.46b the simultaneously measured real-part of the conductivity σ' at 1 MHz. In both cases, the Kraus model (see section 2.4.2) was applied to quantify the characteristics of the respective changes in modulus and conductivity. In table 4.2 the fitting parameters of the model are summarized. In accordance

[42]Usually the degree of hydrogenation is about 95 %, thus there are only view double bonds present.

Table 4.2.: Summary of all fit parameters using the Kraus model to parametrise the strain sweep depicted in figure 4.46. Instead of the small strain modulus G'_0 in case of fitting the Kraus model also to conductivity data, i.e. the small strain conductivity σ'_0 was used respectively.

System	G'_0 [kPa] / σ'_0 [10^{-4}S/cm]	γ_0 [%]	m [-]
NR+N339 (G')	375.1 ± 1.91	1.95 ± 0.1	0.59 ± 0.03
NR+AMIC (G')	501.9 ± 2.79	1.04 ± 0.03	0.67 ± 0.03
NR+N339 (σ')	3.6 ± 0.02	2.19 ± 0.09	0.97 ± 0.07
NR+AMIC (σ')	12.7 ± 0.07	2.19 ± 0.12	0.69 ± 0.04
NBR+N339 (G')	294 ± 1.7	9.86 ± 0.35	0.47 ± 0.02
NBR+AMIC (G')	418.5 ± 2.4	2.63 ± 0.02	0.53 ± 0.04
NBR+N339 (σ')	0.41 ± 0.0033	2.77 ± 0.33	0.54 ± 0.04
NBR+AMIC (σ')	0.749 ± 0.0032	2.55 ± 0.13	0.75 ± 0.04
HNBR+N339 (G')	545.8 ± 4.4	1.04 ± 0.05	0.55 ± 0.03
HNBR+AMIC (G')	791.5 ± 7.7	0.73 ± 0.04	0.63 ± 0.04
HNBR+N339 (σ')	15.4 ± 0.12	1.67 ± 0.09	0.84 ± 0.06
HNBR+AMIC (σ')	8.1 ± 0.04	1.33 ± 0.05	0.72 ± 0.03

with the accelerated build-up process of the mechanically active filler-network in case of the NR due to the presence of AMIC, also its break-down shows a similar tendency. Since for the NR the AMIC molecules reduce the polymer-filler interaction, the resulting filler-filler bonds are much stiffer and hence show a characteristic brittleness or a decreased elasticity at larger deformations.[43] This effect is reflected by an increased small-strain modulus G'_0 (more filler-filler-bond brittleness), a decreased critical strain γ_0 (less stability due to a lack of bond-elasticity) and an increased fractal exponent m (an overall accelerated break-down of the network).
However, in case of both polar polymers, where the blocking mechanism of the AMIC can (partly) be compensated by additional polar bonds, the break-down of the load-bearing paths shows significant differences. Only the increased level of the small-strain modulus for the AMIC-modified systems is common to all polymers. A comparison of the strain sweeps of only the non-modified systems in figure 4.46a yields a clear ranking with respect to characteristics of the filler network break-down. HNBR shows the highest initial value of stiffness and the steepest drop at higher strains. Due to a lack of double bonds, the potential for interacting with the surface of the CB via the aforementioned π-π-stacking mechanism is lowest.
Both double bond-containing polymers NR and NBR show a dynamically softer response and yield a more stable filler-network. Nevertheless, they are different since the NR filler network-structure is still stiffer and therefore breaks down more rapidly than the NBR. These differences are likely caused by the different micro-structure since the methyl group of the NR might reduce the effectiveness of the π-π-stacking due to spatial hindrance effects. Therefore, the load-bearing paths within the NBR system show the highest stability of all polymers.
Introducing the AMIC as polar surface modification leads to additional bonds utilizing to the

[43] There is less polymer confined to the surface, thus the average filler-filler gap is smaller and therefore behaves less elastic.

nitrile group of both NBR and HNBR. Consequently, comparing all three modified systems in figure 4.46a shows a different ranking with respect to the overall Payne-effect. Now the NR system is by far the weakest since the modulus drops the fastest, showing the influence of blocked interaction sites on the surface. Although the HNBR has the highest small-strain modulus, the break-down of the filler network is less pronounced compared to the NR. This indicates, that the additionally available bonds between the polymer and the more polar CB stabilize the filler-filler bond. Moreover, in case of NBR this effect is even more pronounced since there can additionally be π-π-stacking bonds.
In essence, the polymer-filler coupling is determined by both the filler surface, on which there are various energetically active sites, and the polymer microstructure, which defines what type of dispersive and polar bonds can be formed. Hence, this interaction can be altered via blocking active sites with polar ionic liquid molecules on the surface, which reduces the dispersive- but increases the polar-interaction potential. For NR there are almost only dispersive interactions important, thus a blocking reduces its interaction. HNBR almost has no strong dispersive bonding potential but due to the polar nitrile groups some polar potential, therefore blocking dispersive bonds with polar groups shows even a slight advantage. Finally, the NBR does have the potential for both types of bonds and is hence able to benefit from a blocked dispersive bond by being able to form also polar bonds at the same position.
From the simultaneously measured conductivity (see figure 4.46b) further insights of the filler-network structure can be revealed. In particular, the role of paths within the fractal network, that are able to carry load or conduct charge carriers through the system is of significance. In general, both types of network, i.e. the mechanically- and electrically effective structures, show qualitatively a similar behaviour. However, there are also important differences observable. Overall, the strain level at which the conductivity drops from the initial value due to the break-down of the conductive network is slightly larger compared to the break-down of the mechanical network. This effect is more obvious when both strain sweeps are normalized to their respective small-strain values (see figure 4.47). While in case of the storage modulus there is

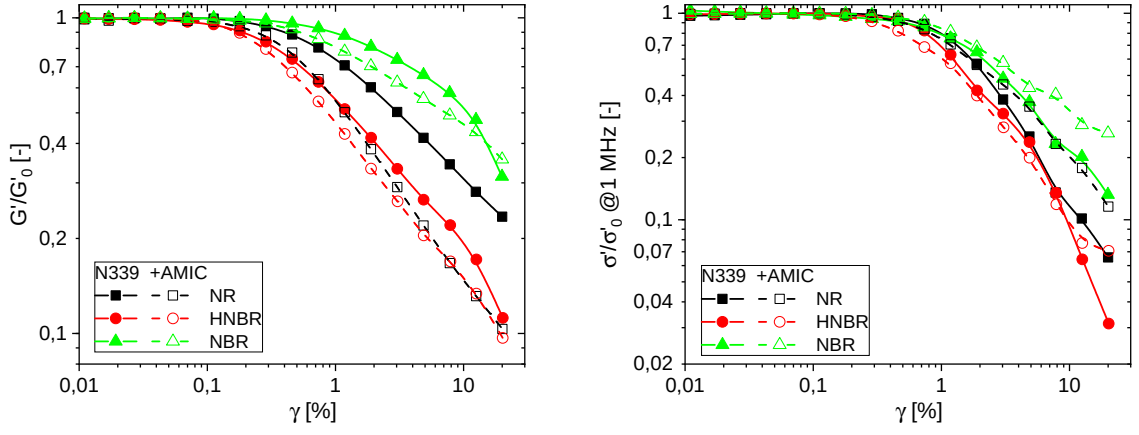

(a) Mechanical breakdown

(b) Dielectric breakdown

Figure 4.47.: Normalized (with respect to the small strain value) strain sweep comparison at 140 °C for NR, HNBR and NBR with and without AMIC modification.

a pronounced differentiation between the various system (polymer type and surface modifica-

tion), the difference in the conductivity is less significant. Especially the critical strain at which the network breaks down is almost the same for all systems (only the AMIC-modified HNBR is slightly different). Apparently, all systems, which show a reduced polymer-filler coupling due to either surface modification (NR+AMIC) or in general a weak interaction (HNBR± AMIC), yield an early mechanical breakdown but still a normal conductivity breakdown. Moreover, the absolute value of the conductivity is in these systems the highest due to the stiffest filler-filler bonds, which are formed because of a reduced amount of confined polymer adjacent to the filler interface.
Therefore, the effect of an early mechanical breakdown is caused by these stiff filler-filler bonds, which then cannot carry any load, and hence the modulus drops. On the other hand, these filler aggregates – formally connected mechanically via the filler-filler bond – are not spatially separated very much after the mechanical break-down. Hence, electrons or other charged particles might still be able to use the filler-filler contact to be transferred further, i.e. the conductivity is still on high level. Nevertheless, also the conductivity drops significantly albeit later than the modulus. Overall the changes of the conductivity - once the conductive network breaks-down - are in average more pronounced than those of the modulus, i.e. the slope of the Payne-Effect curves are steeper in case of the conductivity (see also the values of the parameter m in table 4.2, which are higher in case of the conductivity compared to those describing the modulus).
While the conductivity is governed by continuous paths within the filler network, the mechanical network is additionally influenced by non-continuous substructures which still reinforce hydrodynamically but have no effect on conductivity any more.[44]

4.3.3. Combination of Rheological and Dielectric Measurements for Various Polymer Systems using Surface-Modified Carbon Black Part III: An-isothermal heat Treatment

The previously discussed isothermal re-flocculation phase is followed by a cooling-down phase from 140 °C to 20 °C with a cooling rate of 1 K/min (see regime IV in figure 4.42). Since only non-cross-linked systems are analysed, mainly the filler-polymer interaction determines the behaviour of the material. However, also polymer specific characteristics like the molecular weight distribution influences the temperature dependency. To better assess the micro-mechanical processes, which lead to the characteristic changes in modulus and conductivity, the previously discussed isothermal flocculation phase is plotted additionally to the non-isothermal phase in figure 4.48. Apparently, there is only a weak increase of the modulus during the isothermal flocculation phase in contrast to a significantly stronger change during the an-isothermal cooling. Essentially, the characteristic behaviour during flocculation depends on (i) the depletion forces, which are the main driver for the movement of filler particles or aggregates and (ii) the strength of the polymer-filler interaction. The latter defines the molecular friction between polymer segments and the filler surface, i.e. how easily a filler particle in motion[45] is able to push away adjacent polymer chains. Moreover, the strength of the polymer-filler coupling in-

[44] The effect of a more pronounced drop in conductivity with increasing strain amplitude should also be influenced by the total filler amount since at very high filler concentrations the conductivity will become less dependent on the load, because the structural rearrangements within the filler network will not lead to significant spatial distances between adjacent filler agglomerates.
[45] Driven by entropic depletion forces.

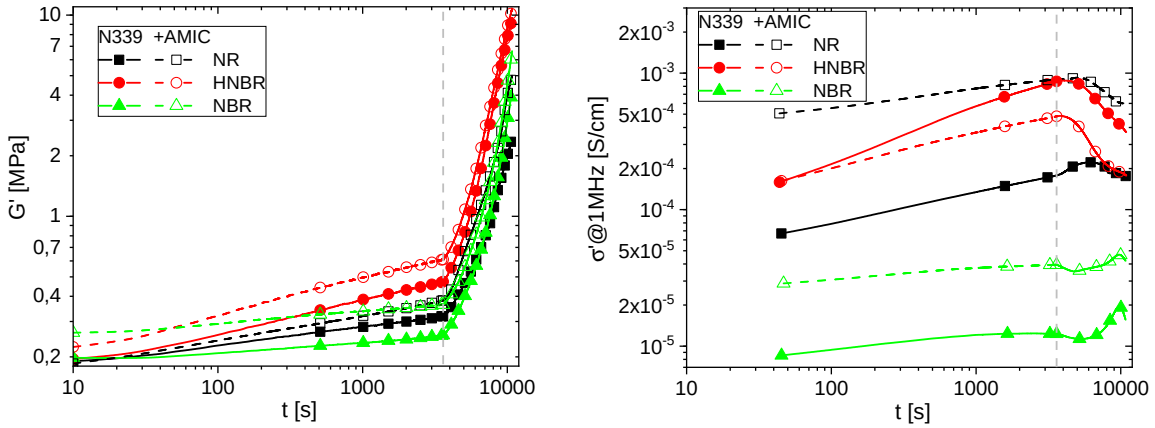

(a) Modulus (b) Conductivity

Figure 4.48.: Storage moduli and conductivity of all three polymer types (NR, NBR and HNBR) + 50 phr N339 (± AMIC) as a function of time during the flocculation and the cool-down. The vertical dashed line indicates the change from isothermal to an-isothermal conditions.

fluences the effective thickness of the layer formed via polymer chains, which are reduced in mobility due to the confinement effect at the filler surface. However, the volume of this immobilized, interfacial layer will apparently depend on the temperature since with increasing thermal energy the desorption rate of polymer segments at the surface will be increased. Thus, the layer-thickness will decrease with increasing temperature.
Consequently, under isothermal conditions the layer thickness around filler particles will be predominantly influenced by (i) the temperature and (ii) the respective strength of the polymer-filler coupling. Thus, the observed agglomeration and filler-network-build-up is mainly caused by the movement of fillers influenced by depletion forces.[46] However, at non-isothermal conditions both mechanisms will change with time. Especially the gradient of polymer-mobility – from the filler surface to the polymer-bulk – will have a pronounced temperature dependency. Since a reduced thermal energy decreases the desorption rate of chains at the filler-interface, the amount of segments, which are confined at the filler surface, is increased. Therefore, the resulting effective layer-thickness of immobilized chains will grow during the cool-down phase. The filler-filler bonds that have been created during the process of flocculation are rather weak at elevated temperatures due to only minor overlapping of two adjacent polymer-layers (of reduced mobility) at the filler surfaces.[47] With decreasing temperature, these filler-filler bonds become stronger because of an increasing volume ($\propto$ (thickness)^3) of layers, which can consequently lead to a more pronounced overlap between two filler aggregates. Hence, at similar average distances of adjacent filler particles, the main difference between high- and low temperature is the strength of filler-filler bonds, which are formed through bridges of immobilized polymer chains confined at the polymer-filler interface. In essence, these bridges are weak at high temperature since the polymer is less confined and become stronger with decreasing temperature due to an

[46] Therefore, it is reasonable to expect only a weak dependency of modulus and conductivity on time, since all observed slopes [see table 4.1] are much smaller than unity.
[47] Since these layers are rather thin at high temperatures.

increasing overlap of the aforementioned layers.
While this transition of layer-mobility changes the mechanical stiffness of the filler network substantially[48], the conductivity is almost not influenced. As previously discussed in subsection 4.3.1, under isothermal conditions the main parameter, which changes with time is the average inter-particle distance, and hence the conductivity changes according to the mechanical stiffness. That is, because paths, which are able to carry stresses as well as transport charge carriers, are build-up with time. However, with decreasing temperature the average inter-particle distances are less affected and the dynamics of the filler-filler bridges will be the dominant process. Consequently, for charge carriers the paths are not significantly changing with time, thus the conductivity will stay on a similar level compared to the initial value at the beginning of the non-isothermal phase or even will decrease due to the reduced mobility of charge carriers in the filler-filler bridges.[49]

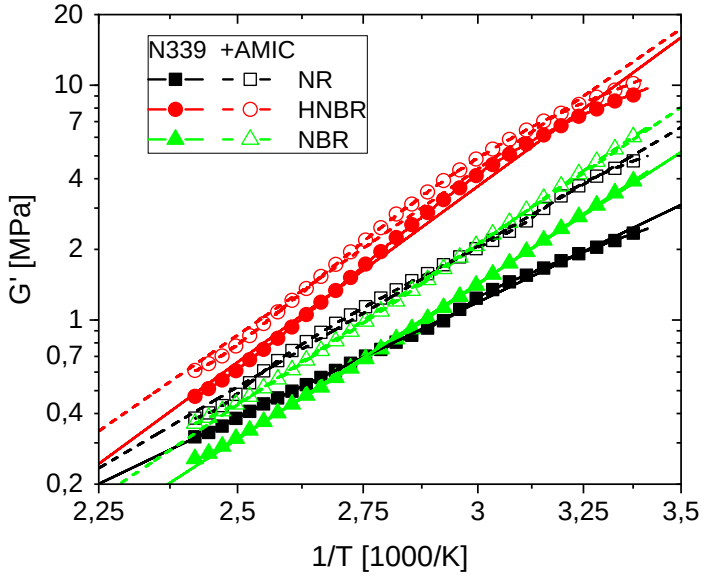

Figure 4.49.: Storage moduli of all three polymer types (NR, NBR and HNBR) + 50 phr N339 ($\pm$ AMIC) as a function of inverse temperature $1/T$. The temperature was changing from 140 °C to 20 °C as depicted in figure 4.42 IV. The lines indicate a linear fit to evaluate the apparent activation energies.

In figure 4.49 the anisothermal phase is depicted in an Arrhenius-like plot, i.e. the logarithmic property (here storage modulus G') is plotted vs. the inverse temperature $1/T$. This representation is useful to reveal characteristic temperature dependencies that follow an exponential function like $\propto \exp\{-E_a/RT\}$. Consequently, a linear increase in modulus with decreasing temperature becomes apparent for all systems – yielding an apparent activation energy E_a. In table 4.3 all respective apparent activation energies - performing a linear fit over the whole tem-

[48] The approximated slope (since the thermal behaviour is better described via an exponential function - see figure 4.49) in the log-log plot shown in figure 4.48 is 10-15 times higher than during the isothermal flocculation phase.

[49] Additionally to this main process, the depletion forces will be reduced with decreasing temperature since there is less thermal energy available for kinetic processes of fillers in the system. Therefore, the resulting rate of flocculation due to depletion forces will be reduced at lower temperatures.

perature range in figure 4.3 - are summarized. In case of the HNBR, the values for the activation

Table 4.3.: Summary of apparent activation energies for all measured polymers following the Arrhenius-law applied on the change of modulus while cooling the samples from 140 °C to 20 °C. (see figure 4.49 for the corresponding curves.)

	E_a [kJ/mol]		
System	NR	NBR	HNBR
N339	17.9 ± 0.05	24.2 ± 0.02	27.1 ± 0.14
AMIC	21.9 ± 0.07	25.1 ± 0.02	25.5 ± 0.14

energy are the highest in comparison to the NR and NBR. Moreover, only for the HNBR, the AMIC system shows a lower value compared to the reference. Although the value itself is influenced by the characteristic polymer-filler interaction, there are also other influencing factors. Each polymer without filler shows already a distinct temperature dependency. At low temperatures, the mobility of chain segments determine the glass transition temperature.[50] Towards more ambient temperatures the rubber-elastic plateau is found, which is determined by the entanglement density in terms of its height. The width of this plateau is influenced by the molecular weight of the polymer chains,[51] i.e. its length.[26] Consequently, there is a certain characteristic temperature after which there will be finally viscous flow behaviour, thus the modulus decreases monotonously with increasing temperature. Moreover, the shape of this crossover region gives rise to the polydispersity[52] of the polymer, i.e. the skewness of its molecular weight distribution.
Introducing filler into the system will change this temperature dependency in several ways. Locally, the dynamics is slowed down due to an additional filler interface, which creates an interphase with different characteristic temperature dependencies than the bulk polymer. This shifts the crossover between rubber plateau and viscous flow towards higher temperatures[53] and creates an additional slope in the G' vs. T plot due to thermally activated filler-filler bonds formed by the polymer-filler interphase. In essence, for all three discussed types of polymer, not only the interaction between polymer and filler is responsible for the characteristic temperature dependency depicted in figure 4.49, but also their characteristic differences determined by the entanglements and molecular weight distribution as unfilled melts.
Natural rubber has by far the highest weight average molecular weight M_w in comparison to the NBR and HNBR.[54] In terms of polydispersity, the NBR yields the largest value of 3.2 whereas the NR and HNBR both have a value of 2.4. The entanglement density is lowest in case of

[50] The more flexible, the lower the glass-transition temperature. Here: $T_G^{NR} = -60$ °C; $T_G^{NBR} = -14$ °C and $T_G^{HNBR} = -23$ °C

[51] The longer the chains, the more time ($\widehat{=}$ higher temperature) they need to thermally fluctuate out of their tube (constrained by the neighbouring entanglements).

[52] The ratio between the weight average $< M_W >$ and the number average $< M_N >$ of its molecular weight distribution $f(M)$.

[53] The characteristic relaxation times will be larger since the system is locally slowed down, thus also more thermal energy is required to generate enough fluctuations for a chain to relax.

[54] M_w^{NR}=832 kg/mol from GPC, M_w^{NBR}=190 kg/mol and M_w^{HNBR}=150 kg/mol from [143] since the same polymers were used here.

the NR, which leads to a plateau modulus of G_N=0.46 MPa.[55] Syed et al. [143] measured the plateau modulus G_N=0.79 MPa and G_N=1.38 MPa of both NBR and HNBR respectively. Qualitatively this entanglement related polymer ranking of moduli is also found in figure 4.49 but only at lower temperatures. While the HNBR is showing the largest value of modulus over the whole range of temperatures, there is a crossover between the NR and the NBR occurring towards elevated temperatures. This crossover is caused by different slopes of the curves, which indicate different interfacial properties on the one hand and additionally characteristic polymer dynamics on the other hand. However, the main contribution is caused by the influence of the filler interphase, since the AMIC modification in case of NR changes the slope significantly and the resulting curve in figure 4.49 is actually very similar to the NBR-AMIC curve. Nevertheless, there is still a different slope comparing these two polymers. Finally, the comparison of the HNBR yields overall the largest slope and moreover the only time that the AMIC system shows a slightly decreased apparent activation energy, indicating an enhancement in the strength of the polymer-filler coupling.

4.4. Energy Efficiency of Elastomers – Results

4.4.1. Ionic Liquid Modifications of Carbon Black in Cured Compounds

In the previous subsection, only the physical networks consisting of polymer entanglements and fillers influenced the characteristics of the compounds. Hence, the effect of a surface-modification with an ionic liquid solely resulted in an altered polymer-filler coupling. In contrast, this subsection describes additionally the potential influence of AMIC on the chemical network formation. Moreover, the type of CB and the non-polar polymer were changed from N339 to N550 and from NR to EPDM respectively due to higher practical significance in real applications.
In table 3.3 and 3.4 the recipes can be found for the EPDM and HNBR respectively. Before the samples can be prepared, a rheometer test has to be performed to measure the curing time of the compounds. In figure 4.50a the torque[56] at 180 °C is depicted as a function of time. There is a pronounced difference in the final torque reached after the vulcanisation reaction is finished and a plateau is reached. The EPDM with AMIC-modified N550 only reaches 75 % of the torque compared to the reference. Thus, the overall network density is reduced due to the modification of the filler surface with AMIC. Although in a non-polar system like NR depicted in figure 4.46 there is a significant drop in mechanical stiffness in case of AMIC,[57] this difference in torque is mainly attributed to the chemical network. If this effect would purely be caused by the polymer-filler interaction, the torque curves would show an off-set already from the beginning. Therefore, it is reasonable to assume that the AMIC-modified surface is more polar compared to the reference and hence more attractive for the polar molecules, thus there is potentially less free accelerator available for the network formation reactions since more of it is bound to the

[55] The plateau modulus G_N measured with rheological experiments is connected to the entanglement modulus G_e (which is 0.58 MPa in case of NR [144]) by a simple prefactor of $4/5$: $G_N = 4/5 G_e$.
[56] More precisely, the real part of the torque, since this is a dynamic test at a frequency of 1.67 Hz and 6 % of dynamic strain.
[57] At 6 % strain there is a drop to only 70 % of modulus for the AMIC system in comparison to the reference.

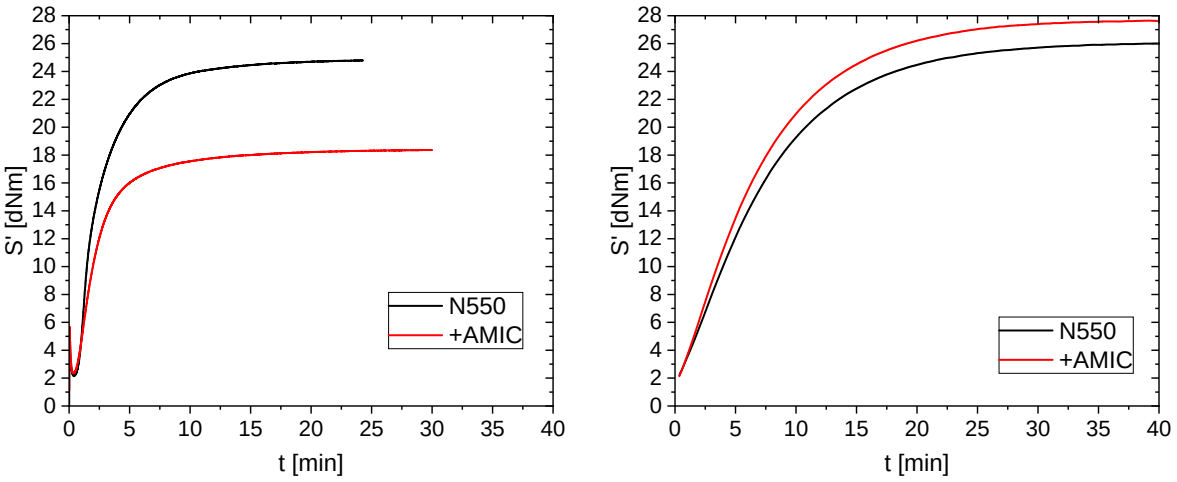

(a) EPDM (b) HNBR

Figure 4.50.: Curing curve, i.e. torque as a function of time for EPDM (at 180 °C) and HNBR (at 170 °C) + 40 phr N550 (± AMIC).

CB surface.
However, in case of a more polar polymer like HNBR depicted in figure 4.50b, the effect of the ionic liquid is very different. For HNBR the reference yields almost the same final torque value than the corresponding EPDM, but the modified system shows an even higher plateau value. This indicates either an increased network density or the effect of an enhanced polymer-filler coupling as discussed in the last part of the previous subsection. In principle, both effects are probable to occur at the same time and additional tests are necessary to decouple these phenomena.
Consequently, mechanical tests have been performed on these samples. First, a quasi-static tensile test[58] was performed. In figure 4.51 the resulting stress-strain curves for the EPDM are shown. There is again a very pronounced influence of the AMIC modification by reducing the stress level and therefore increasing the overall strain. However, the ultimate stress at break is almost identical compared to the reference, only at a significantly higher elongation at break. Although in general this effect is expected assuming an overall decreased network density, the magnitude of the softening due to AMIC seems rather high to be solely caused by an altered chemical network. Most likely, there is an additional effect of the filler network structure due to an decreased strength of the polymer-filler coupling.
In case of the HNBR, depicted in figure 4.52, the difference between AMIC and the reference is vice versa and much less pronounced. To further elucidate the different mechanisms of the observed network and filler effects, cyclic stress strain experiments have been conducted. As explained in section 2.4.3, this kind of experiment yields parameters describing the characteristics of the polymer on the one side, and some filler mechanics on the other side. In figure 4.53, both the measured curves and the respective fits using the DFM are shown. Additionally, there are all fitted parameters of the model given as an inset within the graph. Qualitatively, there is a pronounced difference between both systems with respect to the shape of the cycles and their

[58] See subsection 3.5.1

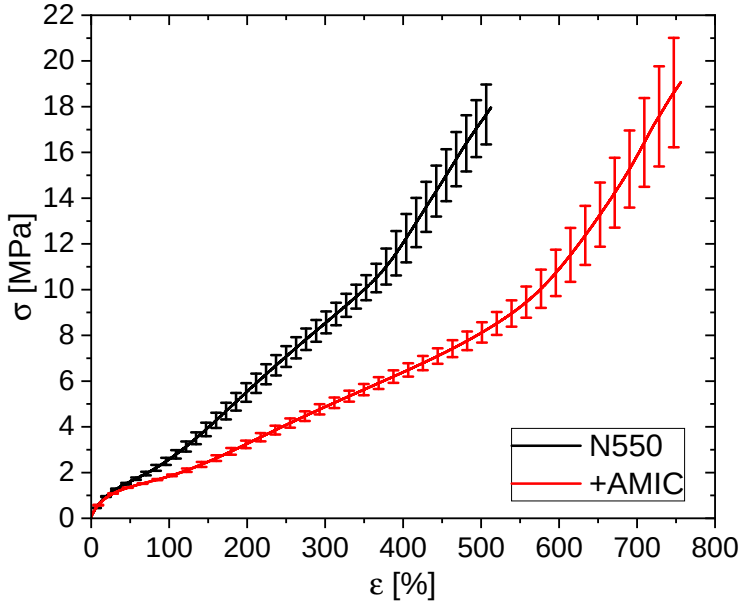

Figure 4.51.: Quasi-static tensile test for EPDM + 40 phr N550 (± AMIC). Error bars indicate 95 % confidence from at least 5 samples.

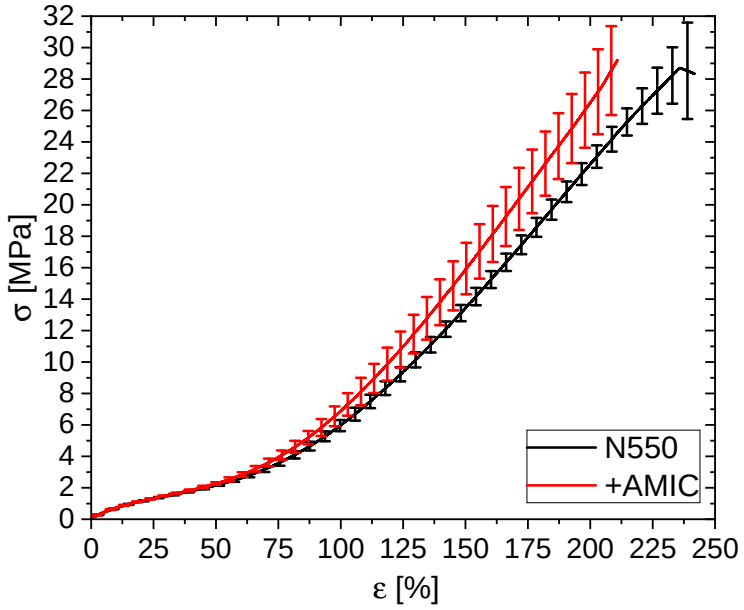

Figure 4.52.: Quasi-static tensile test for HNBR + 40 phr N550 (± AMIC). Error bars indicate 95 % confidence from at least 3 samples.

stress values at the respective strain amplitudes. In general, this indicates again a softer response of the modified sample, which is mostly caused by the reduced network density, which is also quantitatively found in the modulus $G_{total} = G_e + G_c$ in both cases, since the AMIC sample is

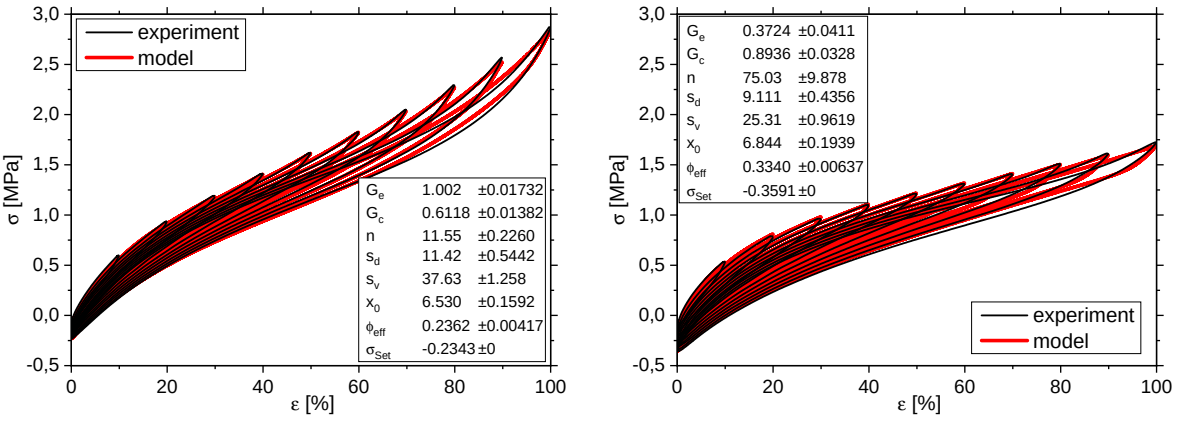

(a) N550 (b) N550+AMIC

Figure 4.53.: Cyclic, quasi-static stress-strain test to quantify the Mullins effect for EPDM + 40 phr N550 (± AMIC) using the DFM model. Only the 5th cycle at each strain amplitude is shown.

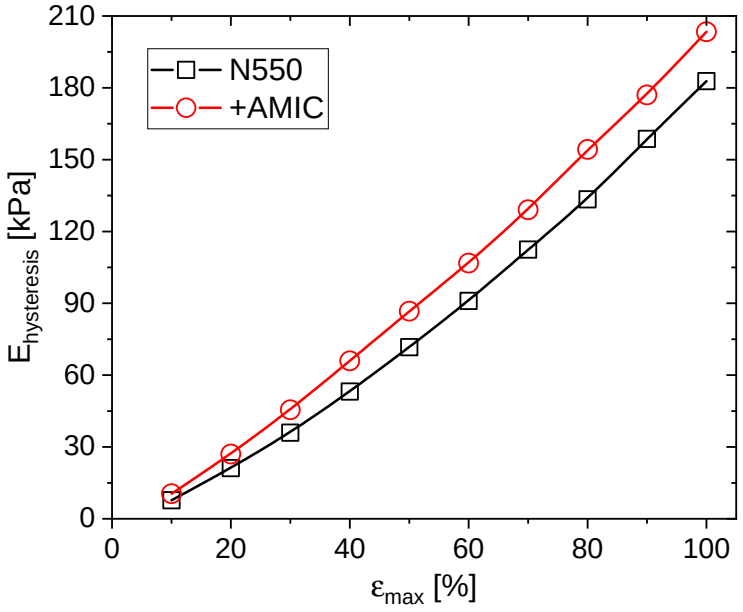

Figure 4.54.: Loss energy-density, i.e. the energy, dissipated in each cycle (unloading- subtracted from loading path), as a function of maximum strain amplitude for EPDM + 40 phr N550 (± AMIC).

only reaching 78 % of the modulus compared to the reference.[59][60]
However, the difference between the loading- and unloading paths, i.e. the energy-density,

[59] The model cannot decouple the effects of entanglements ($\propto G_e$) and cross-links ($\propto G_c$) easily, therefore it is recommended not to investigate the single values but the sum G_{total} of both moduli.

[60] Additionally the parameter n shows a rather high value in case of AMIC, which is caused by the lack of an upturn in the stress-strain cycles. Hence, the network is much looser and network strands are not stretched to a very high extend.

which is caused by the successive breakdown and re-agglomeration of filler clusters, also shows a systematic deviation between both systems. In figure 4.54 these hysteresis-energy-densities are depicted at each loading cycle, i.e. as a function of the respective maximum loading strain. Clearly, the AMIC modification leads to a higher loss of energy within each loading cycle compared to the reference. Furthermore, the absolute delta even increases with higher loading strains, although the relative difference is decreasing. Thus, though the main effect of AMIC seems to be the reduced overall network density, also an altered polymer-filler interaction is apparent, resulting in less stable filler-filler bonds, which dissipate more energy during their break-down and reformation process. Finally all other DFM-parameters s_d, s_v and x_0 are strongly affected by the different network density and therefore their values should not be interpreted. Only the measured set-stress σ_{set} arising from a permanent elongation of the sample at zero stress is also increasing by about 50 % due to the previously discussed cluster breakdown characteristics, additional to the network density effect.
From the previous discussion in subsection 4.3.1 and the first results of the curing curves (figure 4.50b) and the tensile test (figure 4.52), the expectation for the HNBR samples is a general trend towards more stability of the filler network in case of AMIC. Hence, opposite effects comparing the same cyclic tensile test with the EPDM samples are expected. In figure 4.55 the respective

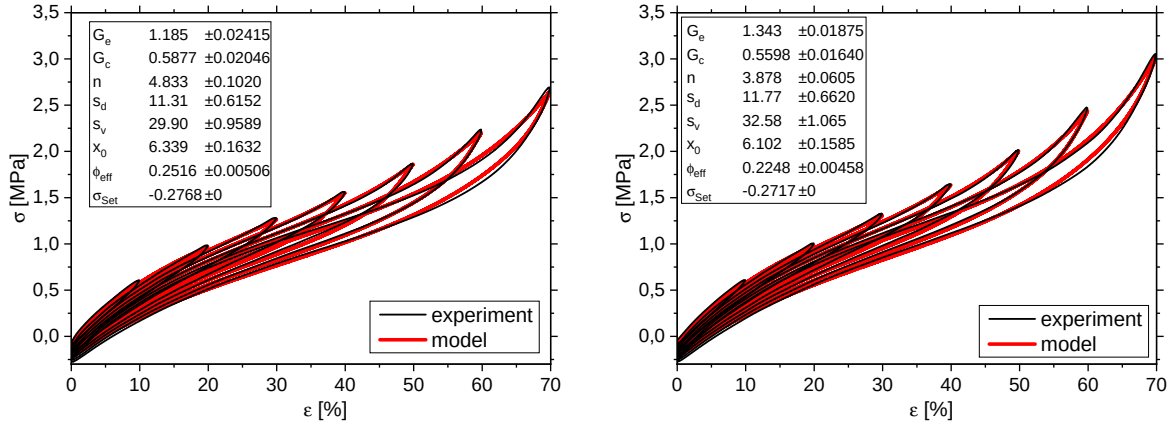

(a) N550 (b) N550+AMIC

Figure 4.55.: Cyclic, quasi-static stress-strain test to quantify the Mullins effect for HNBR + 40 phr N550 (± AMIC) using the DFM model.

results are shown and qualitatively there are only slight differences observable. Similar to the tensile test (figure 4.52), the stress is systematically higher in case of AMIC. Moreover, quantitatively the total modulus from the DFM is 7 % higher for the modified system. Consequently, a comparison of the hysteresis arising from the cluster breakdown and re-agglomeration depicted in figure 4.56 yields slightly decreased values in case of the AMIC system. This observation is in accordance with the expectation of an improved polymer-filler interaction by the addition of AMIC molecules onto the surface as discussed already extensively in section 4.3.

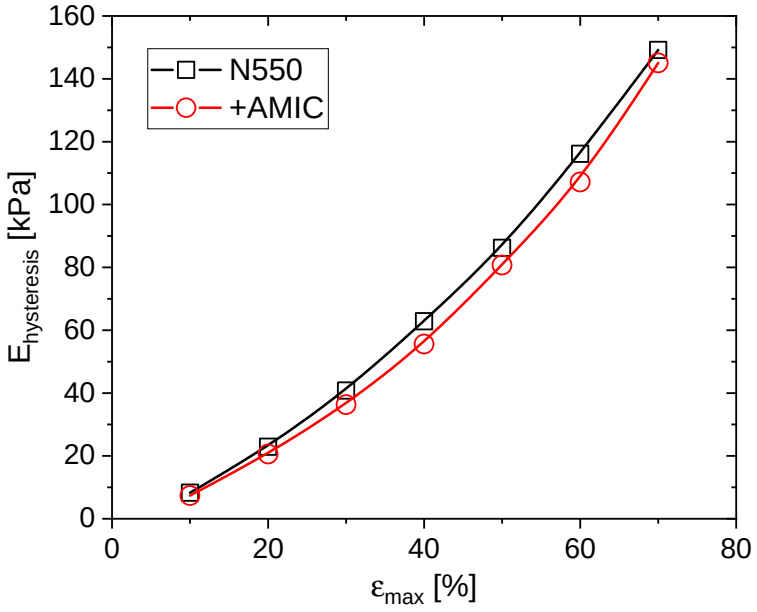

Figure 4.56.: Loss energy-density, i.e. the energy, dissipated in each cycle (unloading- subtracted from loading path), as a function of maximum strain amplitude for HNBR + 40 phr N550 (± AMIC).

4.4.2. Carbon Black Structure in Cured EPDM Compounds

In this subsection also carbon black filled samples are analysed with respect to the influence of a certain modification on mechanical characteristics. In contrast to the two former subsections, where the modification affected mainly the surface and therefore its energetic heterogeneity, now the difference mainly can be found in a different structure of the primary aggregates. Thus, the length-scale of the modification-effect is much larger now.[61] In fact, here the samples, discussed in section 4.2 with respect to a quantification of the structural differences using TEM, are further analysed especially focusing on their mechanical behaviour.
From the analysis of the structural characteristics, it could be concluded that the fractal dimension describing the spatial mass distribution of aggregates in case of S247 is reduced compared to N550 when the filler was used at a level of 50 phr. Moreover, this number was also reduced comparing the 20- versus 50 phr filled S247 samples. Hence, at higher filler loading the intrinsic structure of the aggregates breaks down to a certain degree most probable due to high shear forces during the mixing process. However, an analysis of the mechanical data is essential to see if these differences can be found also in the macroscopic properties of the samples. Therefore, first the compounds have been tested using some standard measures like shore A hardness and rebound resilience. In figure 4.57 both properties are plotted versus each other in such a way, that the energy-dissipative measure (rebound) is shown as a function of the respective stiffness (hardness). With this representation it is possible to better assess a realistic potential of the compound either at equal hardness (vertically) or at equal energy dissipation (horizontally). In case of the S247, there is a significant advantage compared to the N550 in terms of energy efficiency,

[61] While the surface modification happens on the sub-nm scale, the structure of the primary aggregates mainly shows up on several nm up to tens of nm.

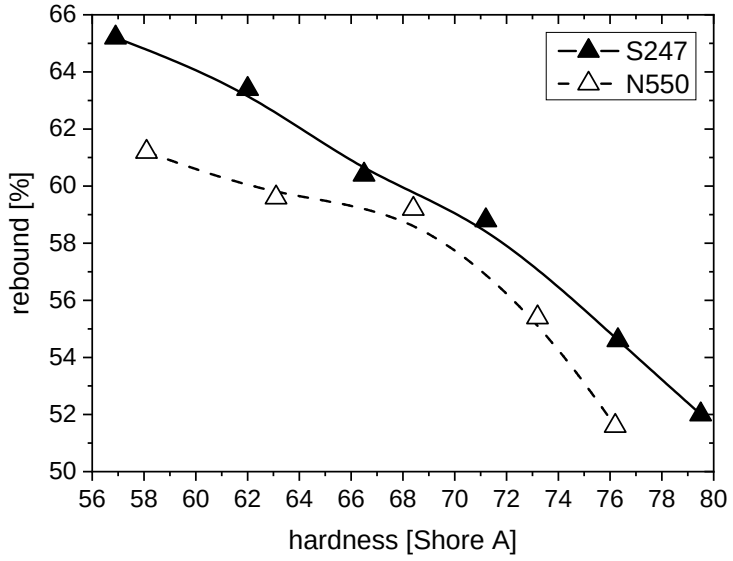

Figure 4.57.: Rebound and shore A hardness of EPDM filled with various levels of N550 and S247.

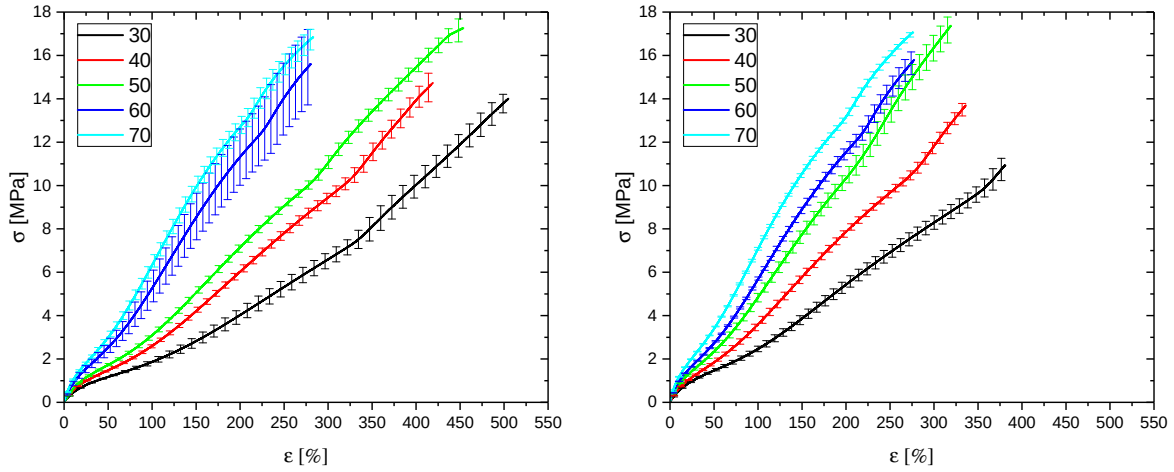

(a) N550 (b) S247

Figure 4.58.: Quasi-static tensile test for EPDM + CB (N550 and S247) (30-70 phr as indicated in the legend).

i.e. a high rebound value due to low hysteresis at similarly low hardness values. However, this advantage decreases slightly at medium and large hardness values, i.e. at filler levels higher than 50 phr. In case of standard tensile tests depicted in figure 4.58, the S247 shows higher stress values below 50 phr and lower values above 50 phr of filler level. This indicates a change in the reinforcing potential of the S247 compared with the N550. While below the mechanical percolation threshold the high structure CB S247 shows the expected benefit over the standard N550, above this limit of filler level the advantage vanishes and becomes even a disadvantage. This observation is expected from the previously discussed hypothesis of a structural breakdown of the aggregates inside the mixer due to high shear forces if there is a certain limit of filler volume fraction reached.

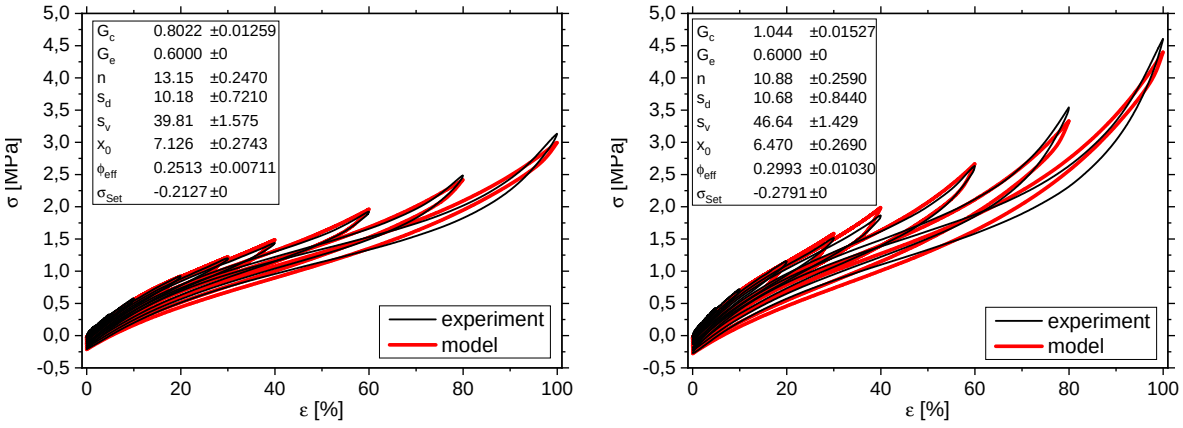

(a) N550 (b) S247

Figure 4.59.: Quasi-static, cyclic stress-strain test for EPDM + 50 phr CB (N550 and S247) to quantify the Mullins effect using the DFM model.

Since the filler level of 50 phr seems to be the critical point of transition, the corresponding cyclic quasi-static tensile tests of these samples including a quantification using the DFM are depicted as an example in figure 4.59.[62] The graphs in figure 4.60 show all parameters of the DFM except the effective filler volume fraction Φ_{eff} (which is separately plotted in figure 4.61) as a function of filler level. Fitting the DFM to the data yields larger values of G_c and smaller values of n, indicating an enhanced network density caused by a larger ratio of filler induced localizations, i.e. additional apparent network junctions due to the presence of filler aggregates. Moreover, the filler-effect is increasing the filler-filler bond strength (s_d and s_v), decreasing the average cluster size x_0 and leads finally to an increased effective filler volume fraction Φ_{eff}. All of these effects point into the direction of an enhanced structure in case of S247 and seems to disagree with the aforementioned hypothesis. Therefore, figure 4.61 summarizes the most robust parameter of the model with respect to the filler effect Φ_{eff} versus the filler volume fraction based on the value from the recipe Φ.[63] Compared to the identity line shown as gray dash-dotted line, both CBs show an increased slope, which is a direct evidence of the inherent structure of the filler. However, the expectation for the high structured S247 would be an even larger slope compared to the N550, which is not observable. There is even a decreasing slope at very high filler volume fractions in case of the S247. Hence, the structural breakdown of the S247 inside the mixer is still a reasonable hypothesis and figure 4.62 finally compares both methods of measuring the effective volume fraction. There is a clear correlation observable between both methods although they are operating on completely different lengths scales. Also there is an overestimation in case of the TEM analysis probably due to the averaging process to get the weight average solid volume fraction.[64]

[62] All other filler levels have been analysed in a similar way.
[63] See appendix **??** for all DFM-parameters as a function of filler level.
[64] The number of data points is most important for the quality of the distribution, which is the basis for any later processing.

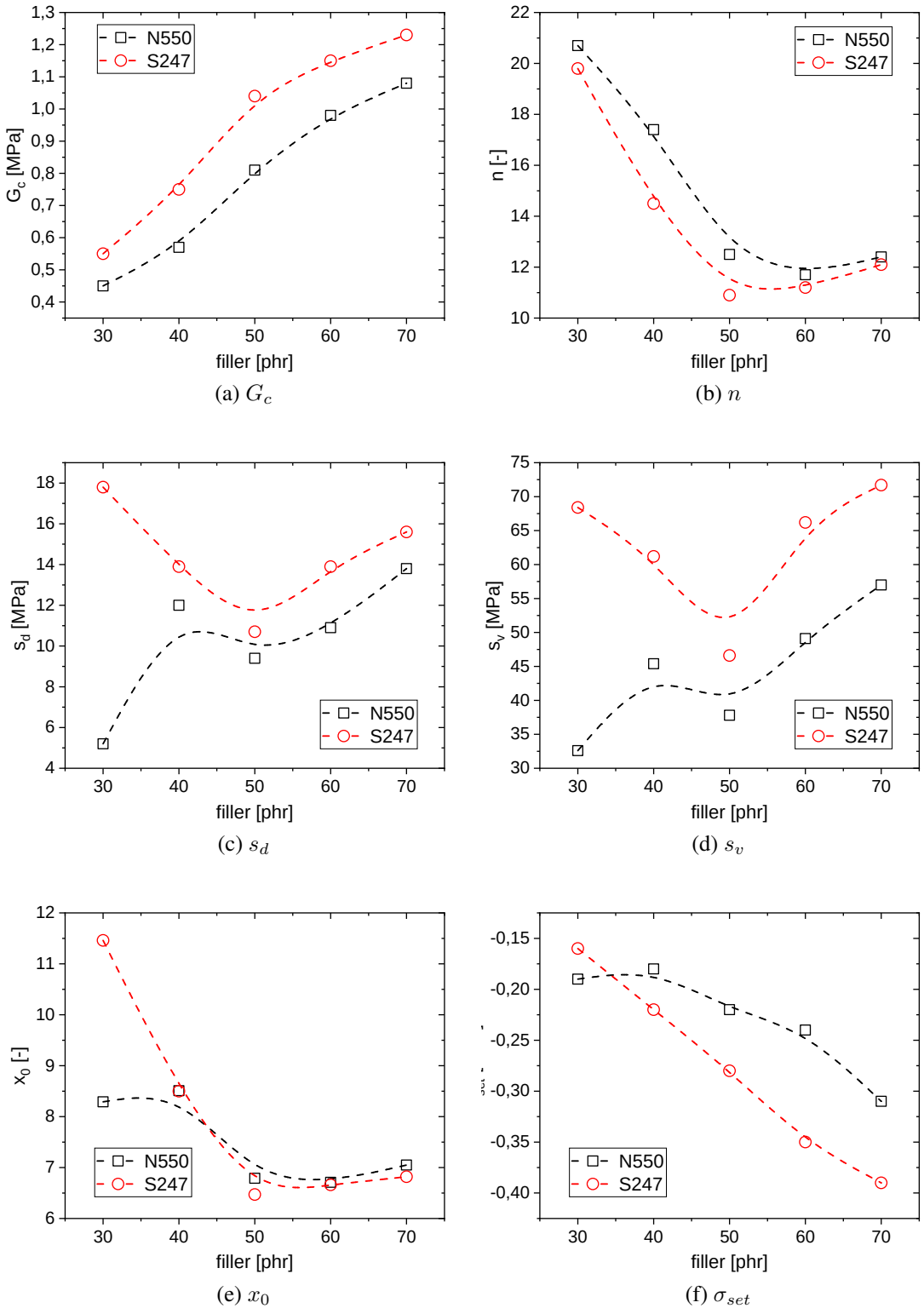

Figure 4.60.: DFM Fit-parameters for EPDM + CB (N550 and S247) (30-70 phr).

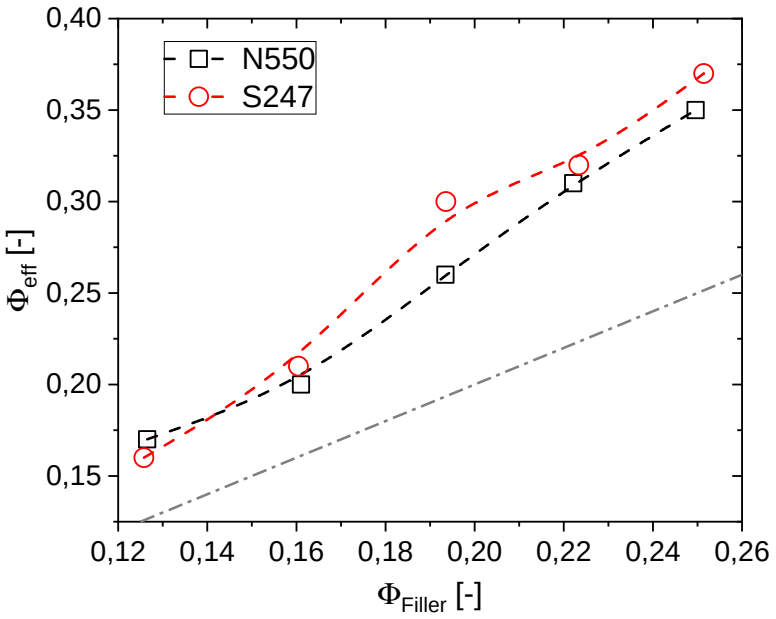

Figure 4.61.: Effective filler volume fraction Φ_{eff} from the DFM model of EPDM filled with various levels of N550 and S247 as a function of filler volume fraction (from recipe). The dash-dotted line indicates the identity.

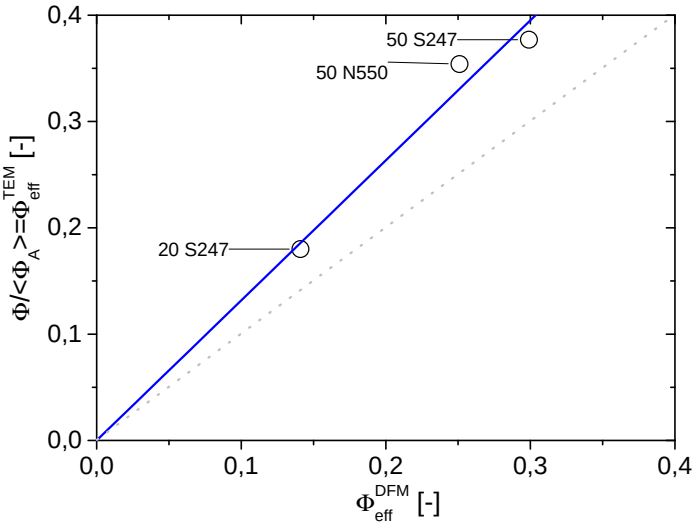

Figure 4.62.: Effective volume fraction calculated from TEM images (see section 4.2.2) in comparison to fitted values of Φ_{eff} from the DFM for S247 and N550 mixed in EPDM.

5. Summary and Conclusions

As discussed very generally in chapter 1, understanding the fundamental mechanisms of the polymer-filler interaction is a multi-scale problem. Therefore, various experimental results have been shown and discussed in the previous chapter 4 focussing on different scales respectively.

The smallest length-scale, i.e. the molecular interaction between polymer-chain segments and the surface of fillers, was analysed using the technique of static gas adsorption (see section 2.2 for a theoretical introduction, 3.2 for details of the experiment and 4.1 for results). In case of intrinsically homogeneous surfaces like graphite or graphitized CB, the amount of high energy sites is found to be very low. Thus, there are only few defects like edges of crystallites or cavities present on these surfaces (see figure 4.9 as an example of the narrow energy distribution function). Moreover, also the surface roughness is in general the lowest for these carbon-based reference materials (see e.g. figure 4.28 to compare various different surfaces).
Furthermore, there are materials like graphene and carbon nano-horns that exhibit an extraordinary high degree of energetic heterogeneity and morphological roughness (see figures 4.26 and 4.27 for the energy distribution and roughness respectively). Additionally, modifying an inhomogeneous surface (e.g. the ASTM CB N339) with ionic liquid molecules (AMIC) leads to an energetically more homogeneous surface without effecting the overall specific surface area and morphological surface-roughness. This effect can be explained by an interaction of the AMIC molecules with the high-energy sites of the surface. Since these sites are not longer available for interaction with gas molecules, they are blocked and hence the dispersive part of the surface is reduced in its activity (see figure 4.18 for the respective energy distribution functions).
Consequently, these blocked sites vary the polymer-filler interaction in a characteristic way. To investigate these changes on a macroscopic length-scale, combined rheological- and dielectric experiments have been conducted for non-cross-linked polymer melts using various types of polymers. In case of non-polar NR, containing many double bonds, a significant decreases in the strength of the polymer-filler interaction was found. On the one hand there was a higher flocculation-rate, leading to an increased modulus observable (see the black curves in figure 4.44 for the flocculation behaviour.). On the other side the break-down of the filler network was found to be accelerated (see again the black curves in figure 4.46 for the Payne-effect.). Hence, due to the blocking of high-energy sites, less polymer segments are bound strongly onto the filler surface and therefore form only a thin layer of confined polymer at the interface. The overlapping of interfacial layers of adjacent filler aggregates leads to the formation of stiff and brittle filler-filler bonds, which leads to the observed higher stiffness at small strain amplitudes (and a faster flocculation) and the rapid break-down at higher strains.
However, in case of more polar polymers like NBR and HNBR observations yield additional aspects about the mechanism of polymer-filler interaction. Although the addition of AMIC onto the surface reduces its dispersive activity, the polar part of the surface is enhanced. Therefore,

the rheological experiments revealed no disadvantageous effect (HNBR) or even an enhancement in the polymer-filler coupling strength (NBR) (see again figures 4.44 and 4.46). Here, the additional polar groups of both polymers can benefit from the polar surface modifications via further polar interactions. The comparison between NBR and HNBR showed the importance of double bonds within the polymer chain, since these are able to interact with the graphitic structures of the CB surface via a π-π-stacking mechanism.
Moreover, cured EPDM[1]- and HNBR-based samples revealed an influence on the energy dissipation and the network density in case of AMIC-modifications (see figure 4.54 and 4.56 for the energy losses during a cyclic stress-strain experiment and figure 4.50 for the network density, depicted via the curing curve.). Apparently, the more polar surface of the filler within the EPDM matrix reduces the network density and thus increases the energy losses, whereas in case of HNBR the opposite effects were observed.

[1]Which is also a non-polar polymer.

Symbols

G, G_N, G_e, G_c, E	Shear-, Plateau-, Entanglement-, Cross-Link-, Young's Modulus
U, F	Internal-, Free Energy
T	Temperature
S	Entropy
λ	Elongation
$\vec{R}$	End-to-end distance
Ω	Conformations
ϵ	Strain
k_B	Boltzman constant
R	Universal gas constant
f	Force
σ	Stress
ν_c	Molar Cross-Link Density
ρ	Mass Density
M_c	Molecular Weight between cross-links
d_0	Tube Diameter
p, p_0	Pressure, Saturation Vapour Pressure
V	Volume
Θ	Surface Coverage
V_m	Monolayer Volume
Q	Adsorption Energy
z	Film Thickness
N_A	Avogadro Constant
α	Van-der-Waals Constant
D_S, D_f	Surface-, Mass-Fractal Dimension
m	Mass
ξ	Cluster Size
V_A	Aggregate Volume
A_S	Aggregate Cross-Sectional Area
P	Perimeter
Φ_A, Φ_{eff}	Aggregate-, Effective Filler Volume Fraction
s_d, s_v	Yield Stress of Damaged- or Virgin Filler-Filler bonds

List of Figures

List of Tables

A. Appendix

A.1. Static Gas Adsorption

A.1.1. Solving the FHH-equation

The three solutions of equation 2.32 are:

$$z_{1/2} = -\frac{1}{3}\left(-\frac{1}{2} \pm \frac{\sqrt{3}i}{2}\right)\left[-\frac{27N_a\alpha}{2RT\log\left(\frac{p_0}{p}\right)} + \frac{1}{2}\left[\left(-\frac{27N_a\alpha}{RT\log\left(\frac{p_0}{p}\right)} + \frac{2\left(-D_SM\gamma+2M\gamma\right)^3}{R^3T^3\rho^3\log^3\left(\frac{p_0}{p}\right)}\right)^2 - \dots \right.\right.$$
$$\left.\left. -\frac{4\left(-D_SM\gamma+2M\gamma\right)^6}{R^6T^6\rho^6\log^6\left(\frac{p_0}{p}\right)}\right]^{1/2} + \frac{\left(-D_SM\gamma+2M\gamma\right)^3}{R^3T^3\rho^3\log^3\left(\frac{p_0}{p}\right)}\right]^{1/3} - \frac{-D_SM\gamma+2M\gamma}{3RT\rho\log\left(\frac{p_0}{p}\right)} - \dots$$
$$-\frac{\left(-D_SM\gamma+2M\gamma\right)^2}{3R^2T^2\rho^2\left(-\frac{1}{2}-\frac{\sqrt{3}i}{2}\right)\log^2\left(\frac{p_0}{p}\right)} \cdot \dots \tag{A.1}$$
$$\cdot \frac{1}{\sqrt[3]{-\frac{27N_a\alpha}{2RT\log\left(\frac{p_0}{p}\right)} + \frac{1}{2}\sqrt{\left(-\frac{27N_a\alpha}{RT\log\left(\frac{p_0}{p}\right)} + \frac{2(-D_SM\gamma+2M\gamma)^3}{R^3T^3\rho^3\log^3\left(\frac{p_0}{p}\right)}\right)^2 - \frac{4(-D_SM\gamma+2M\gamma)^6}{R^6T^6\rho^6\log^6\left(\frac{p_0}{p}\right)}} + \frac{(-D_SM\gamma+2M\gamma)^3}{R^3T^3\rho^3\log^3\left(\frac{p_0}{p}\right)}}}$$

$$z_3 = -\frac{1}{3}\left[-\frac{27N_a\alpha}{2RT\log\left(\frac{p_0}{p}\right)} + \frac{1}{2}\left[\left(-\frac{27N_a\alpha}{RT\log\left(\frac{p_0}{p}\right)} + \frac{2\left(-D_SM\gamma+2M\gamma\right)^3}{R^3T^3\rho^3\log^3\left(\frac{p_0}{p}\right)}\right)^2 - \dots \right.\right.$$
$$\left.\left. -\frac{4\left(-D_SM\gamma+2M\gamma\right)^6}{R^6T^6\rho^6\log^6\left(\frac{p_0}{p}\right)}\right]^{1/2} + \frac{\left(-D_SM\gamma+2M\gamma\right)^3}{R^3T^3\rho^3\log^3\left(\frac{p_0}{p}\right)}\right]^{1/3} - \frac{-D_SM\gamma+2M\gamma}{3RT\rho\log\left(\frac{p_0}{p}\right)} - \dots$$
$$-\frac{\left(-D_SM\gamma+2M\gamma\right)^2}{3R^2T^2\rho^2\log^2\left(\frac{p_0}{p}\right)} \cdot \dots \tag{A.2}$$
$$\cdot \frac{1}{\sqrt[3]{-\frac{27N_a\alpha}{2RT\log\left(\frac{p_0}{p}\right)} + \frac{1}{2}\sqrt{\left(-\frac{27N_a\alpha}{RT\log\left(\frac{p_0}{p}\right)} + \frac{2(-D_SM\gamma+2M\gamma)^3}{R^3T^3\rho^3\log^3\left(\frac{p_0}{p}\right)}\right)^2 - \frac{4(-D_SM\gamma+2M\gamma)^6}{R^6T^6\rho^6\log^6\left(\frac{p_0}{p}\right)}} + \frac{(-D_SM\gamma+2M\gamma)^3}{R^3T^3\rho^3\log^3\left(\frac{p_0}{p}\right)}}}$$

A.1.2. Calculation of energy distribution function

To calculate the energy distribution function the following python script script was used:

```
import pandas as pd
import numpy as np
import matplotlib.pyplot as plt
from matplotlib import cm
#from scipy.optimize import curve_fit
from scipy import interpolate
import scipy as sy
import pylab as plb
#import math
import glob
import scipy.constants as sc
from mpl_toolkits.mplot3d import Axes3D
################################################
def Data_Import(Name):
header_names = ['p','p0','Vd','V','-']
data=pd.read_csv(Name,sep='\t',header=0,names=header_names)

return data
################################################
def BET(Name,Gas,T):
Data=Data_Import(Name)
Na = sc.Avogadro
if Gas=="Nitrogen":
M = 0.02801348
rho = 816
elif Gas=="1Butene":
M = 0.05611
rho = 620
elif Gas=="Ethan":
M = 0.03006
rho = 506
elif Gas=="Propene":
M = 0.04208
if T==227.5:
rho = 607
elif T==232.5:
rho=600
elif T==257.5:
rho = 567
Constant = Na*(2*np.sqrt(3)*(M/(4*np.sqrt(2)*Na*rho))**(2/3))/(22414)
x=Data['p']/Data['p0']
Index_min=np.max(np.where(x<=0.01))
```

```
Index_max=np.min(np.where(x>=0.15))
y=Data['p']/(Data['V']*(Data['p0']-Data['p']))
#BET_Fit=np.polyfit(x[Index_min:Index_max],y[Index_min:Index_max],1)
#BET_Fct=np.poly1d(BET_Fit)
par=np.polyfit(x[Index_min:Index_max],y[Index_min:Index_max],1,
cov=True)
A=par[0][0]
B=par[0][1]
V_m=1/(A+B)
#Fit_X = np.linspace(x[0:1], x[-2:-1], 150)
#Fit_Y = BET_Fct(Fit_X)
#C = 1+A/B
Area = round(V_m*Constant,3)
return V_m,Area#,C,Fit_X,Fit_Y,x,y
################################################
def LogNorm(Q,A,Q_av,het):
return A*plb.exp(-plb.log(Q/Q_av)**2/(2*het**2))
################################################
def Gauss(Q,A,Qav,het):
return A*plb.exp(-(Q-Qav)**2/(2*het**2))
################################################
def Langmuir_Iso(p,Q,C,p0,T):
R = sc.R
return (p*C*np.exp(Q/(R*T)))/(1+p*C*np.exp(Q/(R*T)))

################################################
def ModelIso(p,Q,C,p0,T,Gas):
R = sc.R
z = 4
if Gas=='Nitrogen':
omega = 5600
elif Gas=='1Butene':
omega = 22400
elif Gas=="Ethan":
omega = 15600
elif Gas=="Propene":
omega = 20000
theta = Langmuir_Iso(p,Q,C,p0,T)
b_BET = 1/(1-p/p0)
b_FG = np.exp(z*omega*theta/(R*T))
#b_FG = 1
return (p*b_FG*b_BET**2*C*np.exp(Q/(R*T)))/
(1+p*b_FG*b_BET*C*np.exp(Q/(R*T)))
#def Adamson(Name,Gas,T):
def DataFrameExport(Data):
```

```
Name = Data[5]

Temp_Iso =
{'p/p0':pd.Series(Data[0]),'\g(Q)\-(exp)':pd.Series(
Data[1]),'\g(Q)\-(sim)':pd.Series(Data[2]),
'Area':pd.Series(Data[15])}
Temp_Energy = {'f(Q)':pd.Series(Data[4]),'Q':pd.Series(Data[3]),
'A':pd.Series(Data[6]),'width':pd.Series(Data[7]),
'Q_av':pd.Series(Data[8]),'alpha':pd.Series(Data[9]),
'beta':pd.Series(Data[10]),'gamma':pd.Series(Data[11]),
'shift':pd.Series(Data[12]),'width2':pd.Series(Data[13]),
'width3':pd.Series(Data[14])}
df_Iso = pd.DataFrame(Temp_Iso)
df_Energy = pd.DataFrame(Temp_Energy)
df_Energy.to_csv(Name+'_EnergyDistribution_RossMethod.txt')
df_Iso.to_csv(Name+'_Isotherm_exp_vs_calc_RossMethod.txt')
return print('finished!!')

R = sc.R

#############-------------Test----------------################

def Ross_Method(Name,Gas,T,Q_avstart,w_start,a1,a2,Iterations,
alpha,beta,gamma,shift,type):

R = sc.R
Data = Data_Import(Name+".txt")
B = BET(Name+".txt",Gas,T)
p0 = Data['p0']*1000
p = Data['p']*1000
Q = np.arange(0,40000,40000/len(p))
Q_av = Q_avstart
a = w_start
#da = 0
w1 = a1*R*T
w2 = a2*R*T
w = a*R*T
Err = [100]*Iterations
Err[0]=100
#l = 1
if Gas=='Nitrogen':
tau = 0.00000008
k=1
M=0.02801348
elif Gas=="1Butene":
```

```
tau = 0.0000000000001
k=1
M=0.05611
elif Gas==’Propene’:
if T==227.5:
tau = 0.0000000000001
k=1
elif T==257.5:
tau = 0.0000000000001
k=1
elif T==232.5:
tau = 0.0000000000001
k=1
elif T==237.5:
tau = 0.0000000000001
k=1
elif T==242.5:
tau = 0.0000000000001
k=1
elif T==247.5:
tau = 0.0000000000001
k=1
elif T==252.5:
tau = 0.0000000000001
k=1
M=0.04208
elif Gas=="Ethan":
tau = 0.0000000000001
k=1
M=0.03007
C=k/(1/tau*np.sqrt(2*np.pi*M*R*T))

THET2 = [0]*len(p)
delta = 0
# First Iteration of main peak position
for l in range(0,Iterations):

Q_av = Q_av + delta
a = a #+ da
alpha=alpha#+delta
w = a*R*T
A = 0.001
if type==’Gauss’:
f = Gauss(Q,A,Q_av,w)+Gauss(Q,alpha*A,Q_av+shift,w1)+
Gauss(Q,beta*A,Q_av+1.5*shift,w2)+
```

```
Gauss(Q,gamma*A,Q_av+2*shift,w2)
I=sy.integrate.simps(f,Q)
if I>1.1 or I<0.9:
A = A/I

f = Gauss(Q,A,Q_av,w)+Gauss(Q,alpha*A,Q_av+shift,w1)+
Gauss(Q,beta*A,Q_av+1.5*shift,w2)+
Gauss(Q,gamma*A,Q_av+2*shift,w2)
elif type=='Lognormal':
f = LogNorm(Q,A,Q_av,w)
I=sy.integrate.simps(f,Q)
if I>1.1 or I<0.9:
A = A/I
f = LogNorm(Q,A,Q_av,w)
#while I>1.02 or I<0.98:

I = sy.integrate.simps(f,Q)
#a Min Work: Calculate Iso from model iso and energydist####
for i in range(2,len(p)):
theta = ModelIso(p[i],Q,C,p0,77.,Gas)
THET2[i] = sy.integrate.simps(f*theta,Q)


Theta_exp = Data['V']/B[0]

Err[l] = 1/len(p)*sum(np.sqrt(np.abs(1/p)*(THET2-Theta_exp)**2))
delErr = Err[l]-Err[l-1]
if delErr>0:
break


delta = 50

delta = 0
print('Iterations: position 1st ',l)
for l in range(0,Iterations):

Q_av = Q_av #+ delta
a = a #+ da
alpha=alpha+delta
w = a*R*T
A = 0.001
if type=='Gauss':
f = Gauss(Q,A,Q_av,w)+Gauss(Q,alpha*A,Q_av+shift,w1)+
Gauss(Q,beta*A,Q_av+1.5*shift,w2)+
```

```
Gauss(Q,gamma*A,Q_av+2*shift,w2)
I=sy.integrate.simps(f,Q)
if I>1.1 or I<0.9:
A = A/I

f = Gauss(Q,A,Q_av,w)+Gauss(Q,alpha*A,Q_av+shift,w1)+
Gauss(Q,beta*A,Q_av+1.5*shift,w2)+
Gauss(Q,gamma*A,Q_av+2*shift,w2)
elif type=='Lognormal':
f = LogNorm(Q,A,Q_av,w)
I=sy.integrate.simps(f,Q)
if I>1.1 or I<0.9:
A = A/I
f = LogNorm(Q,A,Q_av,w)
#while I>1.02 or I<0.98:

I = sy.integrate.simps(f,Q)

for i in range(2,len(p)):
theta = ModelIso(p[i],Q,C,p0,77.,Gas)
THET2[i] = sy.integrate.simps(f*theta,Q)


Theta_exp = Data['V']/B[0]

Err[l] = 1/len(p)*sum(np.sqrt(np.abs(1/p)*(THET2-Theta_exp)**2))
delErr = Err[l]-Err[l-1]
if delErr>0:
break

delta = 0.0005

print('Iterations: height alpha ',l)
delta = 0

for l in range(0,Iterations):

Q_av = Q_av #+ delta
a = a #+ da
alpha=alpha#+delta
beta = beta + delta
w = a*R*T
A = 0.001
if type=='Gauss':
f = Gauss(Q,A,Q_av,w)+Gauss(Q,alpha*A,Q_av+shift,w1)+
```

```
Gauss(Q,beta*A,Q_av+1.5*shift,w2)+
Gauss(Q,gamma*A,Q_av+2*shift,w2)
I=sy.integrate.simps(f,Q)
if I>1.1 or I<0.9:
A = A/I

f = Gauss(Q,A,Q_av,w)+Gauss(Q,alpha*A,Q_av+shift,w1)+
Gauss(Q,beta*A,Q_av+1.5*shift,w2)+
Gauss(Q,gamma*A,Q_av+2*shift,w2)
elif type=='Lognormal':
f = LogNorm(Q,A,Q_av,w)
I=sy.integrate.simps(f,Q)
if I>1.1 or I<0.9:
A = A/I
f = LogNorm(Q,A,Q_av,w)

I = sy.integrate.simps(f,Q)

for i in range(2,len(p)):
theta = ModelIso(p[i],Q,C,p0,77.,Gas)
THET2[i] = sy.integrate.simps(f*theta,Q)


Theta_exp = Data['V']/B[0]

Err[l] = 1/len(p)*sum(np.sqrt(np.abs(1/p)*(THET2-Theta_exp)**2))
delErr = Err[l]-Err[l-1]
if delErr>0:
break

delta = 0
print('Iterations: height beta ',l)

for l in range(0,Iterations):

Q_av = Q_av #+ delta
a = a #+ da
alpha=alpha#+delta
gamma = gamma + delta
w = a*R*T
A = 0.001
if type=='Gauss':
f = Gauss(Q,A,Q_av,w)+Gauss(Q,alpha*A,Q_av+shift,w1)+
Gauss(Q,beta*A,Q_av+1.5*shift,w2)+
Gauss(Q,gamma*A,Q_av+2*shift,w2)
```

```
I=sy.integrate.simps(f,Q)
if I>1.1 or I<0.9:
A = A/I

f = Gauss(Q,A,Q_av,w)+Gauss(Q,alpha*A,Q_av+shift,w1)+
Gauss(Q,beta*A,Q_av+1.5*shift,w2)+
Gauss(Q,gamma*A,Q_av+2*shift,w2)
elif type=='Lognormal':
f = LogNorm(Q,A,Q_av,w)
I=sy.integrate.simps(f,Q)
if I>1.1 or I<0.9:
A = A/I
f = LogNorm(Q,A,Q_av,w)

I = sy.integrate.simps(f,Q)

for i in range(2,len(p)):
theta = ModelIso(p[i],Q,C,p0,77.,Gas)
THET2[i] = sy.integrate.simps(f*theta,Q)


Theta_exp = Data['V']/B[0]

Err[l] = 1/len(p)*sum(np.sqrt(np.abs(1/p)*(THET2-Theta_exp)**2))
delErr = Err[l]-Err[l-1]
if delErr>0:
break

delta = 0
print('Iterations: height gamma ',l)


Q_av = Q_avstart
for l in range(0,Iterations):

Q_av = Q_av + delta
a = a #+ da
alpha=alpha#+delta
w = a*R*T
A = 0.001
if type=='Gauss':
f = Gauss(Q,A,Q_av,w)+Gauss(Q,alpha*A,Q_av+shift,w1)+
Gauss(Q,beta*A,Q_av+1.5*shift,w2)+
Gauss(Q,gamma*A,Q_av+2*shift,w2)
I=sy.integrate.simps(f,Q)
```

```
if I>1.1 or I<0.9:
A = A/I

f = Gauss(Q,A,Q_av,w)+Gauss(Q,alpha*A,Q_av+shift,w1)+
Gauss(Q,beta*A,Q_av+1.5*shift,w2)+
Gauss(Q,gamma*A,Q_av+2*shift,w2)
elif type=='Lognormal':
f = LogNorm(Q,A,Q_av,w)
I=sy.integrate.simps(f,Q)
if I>1.1 or I<0.9:
A = A/I
f = LogNorm(Q,A,Q_av,w)

I = sy.integrate.simps(f,Q)
#a# Min Work: Calc Iso from model iso and energydist###
for i in range(2,len(p)):
theta = ModelIso(p[i],Q,C,p0,77.,Gas)
THET2[i] = sy.integrate.simps(f*theta,Q)


Theta_exp = Data['V']/B[0]

Err[l] = 1/len(p)*sum(np.sqrt(np.abs(1/p)*(THET2-Theta_exp)**2))
delErr = Err[l]-Err[l-1]
if delErr>0:
break


delta = 50
print('Iterations: position 2nd',l)


plt.loglog(Data['p']/Data['p0'],Data['V']/B[0],'ko',ms=20,markevery=1,
fillstyle='none')
plt.loglog(p/p0,THET2,lw='3')

print(A,w,Q_av,alpha,beta,gamma,'Surface Area= '+str(B[1])+' m²/g')

Q_new = np.arange(0,np.max(Q),10)
f_new = Gauss(Q_new,A,Q_av,w)+Gauss(Q_new,alpha*A,Q_av+shift,w1)+
Gauss(Q_new,beta*A,Q_av+1.5*shift,w2)+
Gauss(Q_new,gamma*A,Q_av+2*shift,w2)
plt.figure()
plt.plot(Q_new,f_new)
```

```
return p/p0,Theta_exp,THET2,Q_new,f_new,Name,A,w,Q_av,alpha,
beta,gamma,shift,a1,a2,B[1]
```

A.2. TEM Image analysis

In this section there will be a detailed description of the TEM image analysis. In section 2.3 two different relations between the number of particles N_P ($\propto m \propto V_A$) in a cluster and the cross-sectional area A_S are given (equation (2.38) and (2.39)). With these equations one can estimate the volume and hence the mass of the cluster. By plotting the volume as a function of the size ξ the mass-fractal dimension D_f can be evaluated by applying equation (2.37). The challenge regarding the evaluation of the TEM images is in how to measure the different dimensions (e.g. area, size, perimeter) of the clusters.
As analysis tool the mathematical software Maple was used. The original TEM image is a gray-scale image, which means there are many intensity values (I). The first step will be to convert this multi-intensity image into a binary image where only black (=cluster) or white (= no cluster) pixels are present. To achieve this, a threshold value needs to be defined and every pixel with an intensity above this value is set to be $I = 1$ and below is set to $I = 0$ accordingly. Due to various defects within the image, a second step is required, in which the single black pixels that are not part of a bigger cluster are removed.

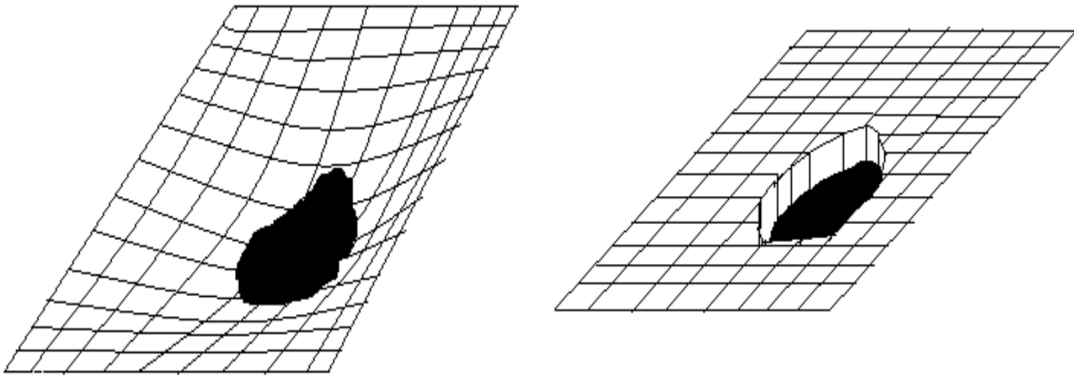

Figure A.1.: Sketch to illustrate the transformation from a continuous to a discrete intensity distribution.

The following lines of code show this procedure in detail:

```
AreaApproximation := proc (Bild::hfarray)
local Flaeche, img, img2, img3, x, y, Intensitaet, Schwelle;
Intensitaet := 1;
Schwelle := .5;
img := Create(Height(Bild, lower) .. Height(Bild, upper),
Width(Bild, lower) .. Width(Bild, upper),
proc (x, y) options operator, arrow; 1 end proc);
```

```
img2 := FitIntensity(Bild, Intensitaet .. 0);
img3 := Create(Height(Bild, lower) .. Height(Bild, upper),
Width(Bild, lower) .. Width(Bild, upper),
proc (x, y) options operator, arrow; 1 end proc);
for x from Height(Bild, lower) to Height(Bild, upper) do
   for y from Width(Bild, lower) to Width(Bild, upper) do
      if Intensitaet*Schwelle <= img2[x, y] then
         img[x, y] := 0;
         img3[x, y] := 0
      end if
   end do
end do;
for x from Height(Bild, lower)+iquo(Height(Bild), 100)
 to Height(Bild, upper)-iquo(Height(Bild), 100) do
   for y from Width(Bild, lower)+iquo(Height(Bild), 100)
    to Width(Bild, upper)-iquo(Height(Bild), 100) do
      if img[x, y] = 0 and img[x+iquo(Height(Bild), 100), y]
       = 1 and img[x, y+iquo(Height(Bild), 100)] = 1 and
       img[x-iquo(Height(Bild), 100), y] = 1
      and img[x, y-iquo(Height(Bild), 100)] = 1 and
      img[x+iquo(Height(Bild), 100), y+iquo(Height(Bild), 100)] = 1
      and img[x-iquo(Height(Bild), 100), y+iquo(Height(Bild), 100)]
       = 1
      and img[x-iquo(Height(Bild), 100), y-iquo(Height(Bild), 100)]
       = 1
      and img[x+iquo(Height(Bild), 100), y-iquo(Height(Bild), 100)]
       = 1
      then
         img[x-iquo(Height(Bild), 100) .. x+iquo(Height(Bild), 100),
         y-iquo(Height(Bild), 100) .. y+iquo(Height(Bild), 100)] := 1
      end if
   end do
end do;
return img
end proc
```

With an image of only two intensities as depicted on the right side of figure A.1 the area can easily be calculated with the mean intensity I_{mean}, which is calculated with Maple via:

$$I_{mean} = \frac{N_{black} I_{black} + N_{white} I_{white}}{N_{black} + N_{white}} \tag{A.3}$$

with the second equation:

$$N_{black} + N_{white} = \text{(width of image)} \times \text{(height of image)}. \tag{A.4}$$

Equation A.3 is solved for N_{black} to get the number of pixels i.e. the cross-sectional area of the aggregate. This calculation is shown as code-lines in the following:

```
NumberofBlack := proc(Bild::anything)
local A,x,y,Hoehe,Breite;
Hoehe:=Height(Bild):Breite:=Width(Bild):
A:=solve({y/(x+y)=Intensity(Bild,mean),x+y=Hoehe*Breite},{x, y}):
assign(A):
return x;
end proc:
```

With this method, the area of the aggregates can be measured. Two more properties are still needed to estimate the fractal dimension: i) the perimeter P and ii) the size of the cluster ξ. To get the perimeter P the edge of a cluster needs to be detected. This is easily achieved by looking for pixels where the intensity is changed with respect to the neighbouring pixel. A procedure where this is done is shown in the following:

```
EdgeDetection := proc(Bild::anything)
local x,y,imgHelp,Hoehe,Breite,xmin,ymin,xmax,ymax,Schwelle,
Intensitaet,
Praezision; Hoehe:=Height(Bild):Breite:=Width(Bild):
Schwelle:=.5:Intensitaet:=1:Praezision:=1:
xmin:=Height(Bild,lower):xmax:=Height(Bild,upper):
ymin:=Width(Bild,lower):ymax:=Width(Bild,upper):
imgHelp:=Create(xmin..xmax,ymin..ymax,(x, y)->1,fit=true):
for x from xmin+Praezision to xmax do
   for y from ymin to ymax-Praezision do
      if Schwelle*Intensitaet <= abs(Bild[x,y+Praezision]-
      Bild[x-Praezision,y]) or
      Schwelle*Intensitaet <= abs(Bild[x-Praezision,y]-
      Bild[x,y]) or
      Schwelle*Intensitaet <= abs(Bild[x-Praezision,y+Praezision]-
      Bild[x-Praezision,y]) or
      Schwelle*Intensitaet <= abs(Bild[x,y]-
      Bild[x-Praezision,y+Praezision]) then
         imgHelp[x-Praezision, y]:=0:
      end if:
   end do:
end do:
return imgHelp:
end proc:
```

The last missing ingredient for the fractal analysis of the aggregate structure is the size ξ. There are actually three obvious choices for the size: i) $\xi = R_{max}$ the maximum diameter of the cluster, ii) $\xi = R_{gyration}$ the radius of gyration and iii) $\xi = R_{hydrodynamic}$ the hydrodynamic radius, which is the radius of gyration of only considering the edge of the cluster. To calculate these radii it is needed to estimate the coordinates of the centre of mass $\vec{R}_{CM}$ of the cluster (see

figure 4.30 for an illustration).

$$\vec{R}_{CM} = \frac{1}{N_{all}} \sum_{i}^{N_{all}} \vec{r}_i \tag{A.5}$$

$$R_{max} = \max\left(\left|\vec{R}_i - \vec{R}_{CM}\right|\right) \tag{A.6}$$

$$R_{gyration} = \frac{1}{N_{all}} \sum_{i=1}^{N_{all}} \left|\vec{R}_i - \vec{R}_{CM}\right| \tag{A.7}$$

$$R_{hydrodynamic} = \frac{1}{N_{edge}} \sum_{i=1}^{N_{edge}} \left|\vec{R}_i - \vec{R}_{CM}\right| \tag{A.8}$$

The respective Maple code is as follows:

```
SchwerpunktBestimmung := proc(Bild::anything)
local x,y,xs,ys,xmin,xmax,ymin,ymax,N,X,Y,SP:
xmin:=Height(Bild,lower):xmax:=Height(Bild,upper):
ymin:=Width(Bild,lower):ymax:=Width(Bild,upper):
N:=round(NumberofBlack(Bild)):
X:=0:Y:=0:
for x from xmin to xmax do
   for y from ymin to ymax do
      if Bild[x,y]=0 then
         xs:=x:ys:=y:
         X:=X+xs:Y:=Y+ys:
      end if:
   end do:
end do:
SP:=evalf([X/N,Y/N]):
return SP:
end proc:
```

```
MeanSizeOf := proc(Bild::anything)
local x,y,xs,ys,xmin,xmax,ymin,ymax,SP,diffx,diffy,RGyr,N,R,
R1,Rmax,Groesse,Groessemin,i;
read("SchwerpunktBestimmung"):
SP:=SchwerpunktBestimmung(Bild);
xs:=SP[1]:ys:=SP[2]:
xmin:=Height(Bild,lower):xmax:=Height(Bild,upper):
ymin:=Width(Bild,lower):ymax:=Width(Bild,upper):
N:=round(NumberofBlack(Bild)):
Rmax:=Array(1 .. N):R:=1:R1:=0:
diffx:=0:diffy:=0:
i:=1:
for x from xmin to xmax do
   for y from ymin to ymax do
```

```
      if Bild[x, y] = 0 then
         diffx:=abs(x-xs):diffy:=abs(y-ys):
         R:=evalf(sqrt(diffx^2+diffy^2)):
         Rmax[i]:=R:
         i:=i+1:
         R1:=R1+R:
      end if:
   end do:
end do:
Groesse:=max(Rmax):
Groessemin:=min(Rmax):
RGyr:=evalf(R1/N):
return RGyr:
end proc:
```

Finite size effects:
Maple is converting each TEM-image into a matrix with entries of the intensity at each pixel. Accordingly, the speed with which the program can scan through the matrix is depending on the size of the image. The original images were taken with a resolution of 4 megapixels (MP) which leads to very computationally expensive calculations when analysing several thousands of individual clusters. To reduce the effort, the size of the images was reduced by a factor of 100 (200×200 instead of 2000×2000 pixels). This leads to a much faster calculation, but also to unwanted side effects. One of this is the so called finite size effect. The images consist of single pixels and by reducing the resolution the accuracy of describing shapes (e.g. of clusters) with these low amount of pixels is reduced. To take into account this inaccuracy, 1000 test-images with circles of different diameter were created and analysed.

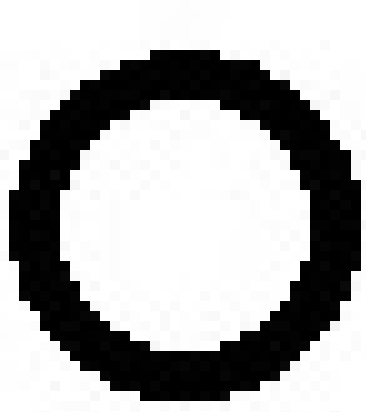

Figure A.2.: Typical example of small sized circle with finite size effects due to a limited amount of pixels.

Depicted in figure A.3 is the scaling of the perimeter P, volume V and area A for spheres with different radius. As expected, the scaling turns out to be $S \propto R$, $A \propto R^2$ and $V \propto R^3$ respectively. This serves as proof of concept for the calculation of the different values in the

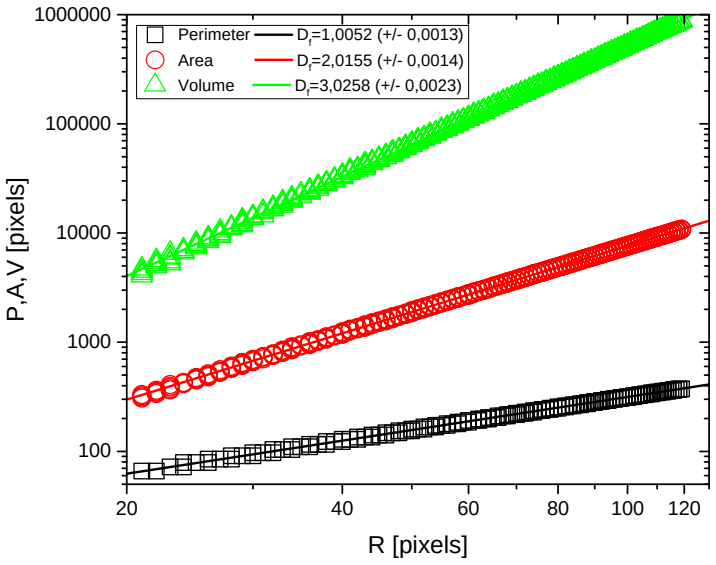

Figure A.3.: Perimeter area and volume calculated for 1000 spheres of different radii.

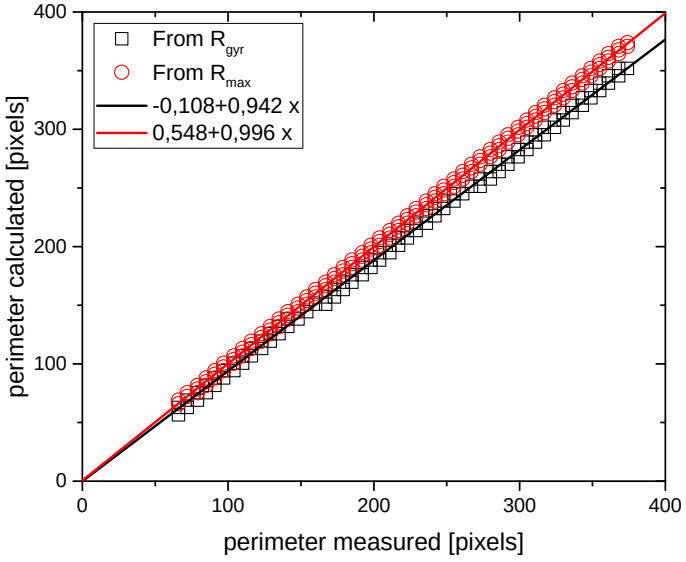

Figure A.4.: Perimeter of 1000 spheres measured vs. calculated with i) radius of gyration R_{gyr} and ii) maximum radius R_{max}.

analysis explained in the text above. For radii between 10 and 20 pixels one observers a bit more deviation from the perfectly linear behaviour, which is a first hint on some finite-size effects (see figure A.2). Additionally to the area and the volume of spheres, the perimeter is used as one important measure. In figure A.4 the measured perimeter is compared to two different calculated values. One of those perimeters was calculated with the maximum radius of the sphere, whereas the other was using the radius of gyration. It turns out that for the maximum diameter an almost perfect correlation is found. For the radius of gyration a small correction needs to be considered.

The finite size effects gets more obvious if not only the volume itself is considered but the volume-fraction of each aggregate (here: spheres) Φ_A as the ratio of volume which is measured and a sphere with radius R_{max}.

$$\Phi_A = \frac{V_{Sphere}}{\frac{4}{3}\pi R_{max}^3} \tag{A.9}$$

This volume fraction in case of spheres (or circles as their respective 2-D-projections) should always be equal to one. In figure A.5 the deviation becomes very obvious for small radii. In case of spheres with radius larger than 30 pixels the error becomes less than $2\,\%$ of the expected theoretical value.

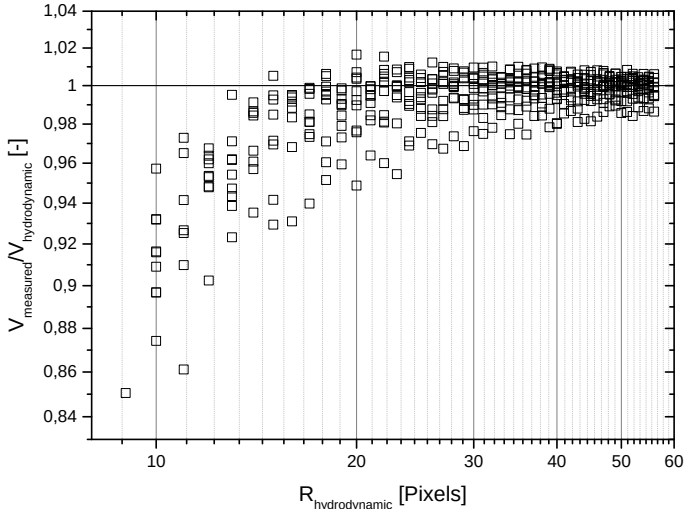

Figure A.5.: Solid volume fraction Φ for spheres with different radii $R_{hydrodynamic}$.

A.3. Curriculum Vitae and List of Publications

Personal data

Name:	Frank Fleck
Date and place of birth:	15.02.1983 in Haldensleben , Germany
E-mail:	frank.fleck83@gmail.com

Work experience

Since 07/2014	Department applied material physics Continental Reifen Deutschland GmbH Hannover
09/2010-06/2014	Scientific Co-Worker Deutsches Institut für Kautschuktechlogie (DIK) Hannover

Scientific Education

09/2010-06/2014	PhD Student DIK Hannover
04/2010	Diploma in Physics Otto-von-Guericke University Magdeburg Grade: 2,1
10/2003-04/2010	Studies of physics Otto-von-Guericke University Magdeburg

Publications

- M Viktorova, R Hentschke, **F Fleck**, C Prange, HA Karimi-Varzaneh; Mesoscopic Model for the Simulation of Dynamic Mechanical Properties of Filled Elastomers: Model Construction and Parameterization; ACS Applied Polymer Materials 2 (12), 5521-5532, 2020
- R Everaers, HA Karimi-Varzaneh, **F Fleck**, N Hojdis, C Svaneborg; Kremer–Grest Models for Commodity Polymer Melts: Linking Theory, Experiment, and Simulation at the Kuhn Scale; Macromolecules 53 (6), 1901-1916, 2020
- H Syed, P Vouagner, **F Fleck**, J Lacayo-Pineda; Nonlinearity in the Mechanical Response of Rubber as Investigated by High-Frequency DMA; Polymers 11 (4), 581, 2019
- IH Syed, D Klat, A Braer, **F Fleck**, J Lacayo-Pineda; Characterizing the influence of reinforcing resin on the structure and the mechanical response of filled isoprene rubber; Soft Materials 16 (4), 275-288, 2018
- C Svaneborg, HA Karimi-Varzaneh, N Hojdis, **F Fleck**, R Everaers; Multiscale approach to equilibrating model polymer melts; Physical Review E 94 (3), 032502, 2016

- **F Fleck**, M Möwes, M Klüppel; Influence of ionic liquid on the polymer-filler coupling of carbon black filled elastomers; Kautsch. Gummi Kunstst 4, 49-52, 2016
- M Klüppel, MM Möwes, A Lang, J Plagge, M Wunde, **F Fleck**, CW Karl; Characterization and application of graphene nanoplatelets in elastomers; Designing of Elastomer Nanocomposites: From Theory to Applications, 319-360; 2016
- V Kumar, T Hanel, **F Fleck**, M Möwes, T Dilman, U Giese, M Klüppel; Graphene filled nitrile butadiene rubber nanocomposites; KGK-KAUTSCHUK GUMMI KUNSTSTOFFE 68 (6), 69-79, 2015
- **F Fleck**, V Froltsov, M Klüppel; Polymer-filler interphase dynamics and reinforcement of elastomer nanocomposites; Soft Materials 12 (sup1), S121-S134; 2014
- M Möwes, **F Fleck**, M Klüppel; Effect of filler surface activity and morphology on mechanical and dielectric properties of NBR/Graphene nanocomposites; Rubber Chemistry and Technology 87 (1), 70-85; 2014
- O Götze, SE Krüger, **F Fleck**, J Schulenburg, J Richter; Ground-state phase diagram of the spin-1 2 square-lattice J 1-J 2 model with plaquette structure; Physical Review B 85 (22), 224424; 2012

A. Appendix

Bibliography

[1] ALGER, M.: *Polymer Science Dictionary*. Springer Netherlands, 1996 https://books.google.ca/books?id=OSAaRwBXGuEC. – ISBN 9780412608704

[2] DE, SK ; WHITE, JR: *Rubber Technologist's Handbook Volume 1. UK: Rapra Technology Limited*. 2001

[3] WILLIAMS, Malcolm L. ; LANDEL, Robert F. ; FERRY, John D.: The Temperature Dependence of Relaxation Mechanisms in Amorphous Polymers and Other Glass-forming Liquids. In: *Journal of the American Chemical Society* 77 (1955), Nr. 14, 3701-3707. http://dx.doi.org/10.1021/ja01619a008. – DOI 10.1021/ja01619a008

[4] KEMPERMANN, Theo: *Handbuch für die Gummiindustrie*. Bayer AG, 1992

[5] RÖTHEMEYER, Fritz ; SOMMER, Franz: *Kautschuktechnologie: Werkstoffe-Verarbeitung-Produkte*. Carl Hanser Verlag GmbH Co KG, 2013

[6] DE GENNES, P. G.: Reptation of a Polymer Chain in the Presence of Fixed Obstacles. In: *jcp* 55 (1971), Juli, Nr. 2, S. 572–579. http://dx.doi.org/10.1063/1.1675789. – DOI 10.1063/1.1675789

[7] DE GENNES, Pierre-Gilles: Entangled polymers. In: *Physics Today* 36 (1983), Juni, Nr. 6, S. 33–47. http://dx.doi.org/10.1063/1.2915700. – DOI 10.1063/1.2915700

[8] EDWARDS, S F.: The statistical mechanics of polymerized material. In: *Proceedings of the Physical Society* 92 (1967), Nr. 1, 9. http://stacks.iop.org/0370-1328/92/i=1/a=303

[9] GAYLORD, RichardJ.: The constant volume tube model of rubber elasticity. In: *Polymer Bulletin* 8 (1982), Nr. 7-8, 325-329. http://dx.doi.org/10.1007/BF00264921. – DOI 10.1007/BF00264921. – ISSN 0170–0839

[10] HEINRICH, G. ; STRAUBE, E.: On the strength and deformation dependence of the tube-like topological constraints of polymer networks, melts and concentrated solutions. II. Polymer melts and concentrated solutions. In: *Acta Polymerica* 35 (1984), Nr. 2, 115–119. http://dx.doi.org/10.1002/actp.1984.010350201. – DOI 10.1002/actp.1984.010350201. – ISSN 1521–4044

[11] HEINRICH, G. ; STRAUBE, E. ; HELMIS, G.: Rubber elasticity of polymer networks: Theories. In: *Advances in Polymer Science* 85 (1988), S. 33. http://dx.doi.org/10.1007/BFb0024048. – DOI 10.1007/BFb0024048. – ISSN 0065–3195

[12] EDWARDS, S F. ; VILGIS, T A.: The tube model theory of rubber elasticity. In: *Reports on Progress in Physics* 51 (1988), Nr. 2, 243. http://stacks.iop.org/0034-4885/51/i=2/a=003

[13] HEINRICH, G. ; VILGIS, T. A.: Contribution of entanglements to the mechanical properties of carbon black-filled polymer networks. In: *Macromolecules* 26 (1993), Nr. 5, 1109-1119. http://dx.doi.org/10.1021/ma00057a035. – DOI 10.1021/ma00057a035

[14] MCCOY, Benjamin J. ; ROLSTON, Dennis E.: Effect of Combined Adsorption and Absorption in Migration of Soil Contaminants. Version: 1993. http://dx.doi.org/http://dx.doi.org/10.1016/S0167-2991(08)63544-2. In: SUZUKI, Motoyuki (Hrsg.): *Fundamentals of Adsorption Proceedings of the Fourth International Conference on Fundamentals of Adsorption* Bd. 80. Elsevier, 1993. – DOI http://dx.doi.org/10.1016/S0167–2991(08)63544–2. – ISSN 0167–2991, 429 - 436

[15] STRAUBE, E ; URBAN, V ; PYCKHOUT-HINTZEN, W ; RICHTER, D ; GLINKA, CJ: Small-angle neutron scattering investigation of topological constraints and tube deformation in networks. In: *Physical review letters* 74 (1995), Nr. 22, S. 4464

[16] HEINRICH, G. ; KALISKE, M.: Theoretical and numerical formulation of a molecular based constitutive tube-model of rubber elasticity. In: *Computational and Theoretical Polymer Science* 7 (1997), Nr. 3–4, 227 - 241. http://dx.doi.org/http://dx.doi.org/10.1016/S1089-3156(98)00010-5. – DOI http://dx.doi.org/10.1016/S1089–3156(98)00010–5. – ISSN 1089–3156

[17] KALISKE, M ; HEINRICH, G: An extended tube-model for rubber elasticity: statistical-mechanical theory and finite element implementation. In: *Rubber Chemistry and Technology* 72 (1999), Nr. 4, S. 602–632

[18] KALISKE, M. ; HEINRICH, G.: An Extended Tube-Model for Rubber Elasticity: Statistical-Mechanical Theory and Finite Element Implementation. In: *Rubber Chemistry and Technology* 72 (1999), Nr. 4, 602-632. http://dx.doi.org/10.5254/1.3538822. – DOI 10.5254/1.3538822

[19] KLÜPPEL, Manfred ; SCHRAMM, Joachim: A generalized tube model of rubber elasticity and stress softening of filler reinforced elastomer systems. In: *Macromolecular theory and simulations* 9 (2000), Nr. 9, S. 742–754

[20] MERGELL, Boris ; EVERAERS, Ralf: Tube models for rubber-elastic systems. In: *Macromolecules* 34 (2001), Nr. 16, S. 5675–5686

[21] MCLEISH, T. C. B.: Tube theory of entangled polymer dynamics. In: *Adv. Phys* (2002), S. 1379–1527

[22] LIKHTMAN, Alexei E. ; MCLEISH, Tom C. B.: Quantitative Theory for Linear Dynamics of Linear Entangled Polymers. In: *Macromolecules* 35 (2002), Nr. 16, 6332-6343. http://dx.doi.org/10.1021/ma0200219. – DOI 10.1021/ma0200219

[23] GRAESSLEY, William W.: Entangled linear, branched and network polymer systems—

molecular theories. In: *Synthesis and Degradation Rheology and Extrusion*. Springer, 1982, S. 67–117

[24] DOI, M. ; EDWARDS, S.F.: *The Theory of Polymer Dynamics*. Clarendon Press, 1988 (Comparative Pathobiology - Studies in the Postmodern Theory of Education). https://books.google.de/books?id=dMzGyWs3GKcC. – ISBN 9780198520337

[25] LAKES, Roderic S.: *Viscoelastic solids*. Bd. 9. CRC press, 1998

[26] AUHL, Dietmar ; RAMIREZ, Jorge ; LIKHTMAN, Alexei E. ; CHAMBON, Pierre ; FERNYHOUGH, Christine: Linear and nonlinear shear flow behavior of monodisperse polyisoprene melts with a large range of molecular weights. In: *Journal of Rheology* 52 (2008), Nr. 3, 801-835. http://dx.doi.org/10.1122/1.2890780. – DOI 10.1122/1.2890780

[27] LOAN, L.D.: Crosslinking efficiencies of dicumyl peroxide in unsaturated synthetic rubbers. In: *Journal of Applied Polymer Science* 7 (1963), Nr. 6, 2259-2268. http://dx.doi.org/10.1002/app.1963.070070624. – DOI 10.1002/app.1963.070070624. – cited By 37

[28] HOFMANN, Werner: *Vulcanization and vulcanizing agents*. Maclaren London, 1967

[29] AKIBA, M. ; HASHIM, A.S.: Vulcanization and crosslinking in elastomers. In: *Progress in Polymer Science* 22 (1997), Nr. 3, 475 - 521. http://dx.doi.org/https://doi.org/10.1016/S0079-6700(96)00015-9. – DOI https://doi.org/10.1016/S0079–6700(96)00015–9. – ISSN 0079–6700

[30] BUECHE, F: Tensile strength of rubbers. In: *Journal of Polymer Science* 24 (1957), Nr. 106, S. 189–200

[31] BUECHE, F ; DUDEK, TJ: Tensile strength of amorphous gum rubbers. In: *Rubber Chemistry and Technology* 36 (1963), Nr. 1, S. 1–10

[32] PAYNE, A.R.: The Dynamic Properties of Carbon Black Loaded Natural Rubber Vulcanizates. Part II. In: *Journal of Applied Polymer Science* 6 (1962), S. 368. http://dx.doi.org/10.1002/app.1962.070062115. – DOI 10.1002/app.1962.070062115

[33] HARWOOD, J.A.C. ; MULLINS, L. ; PAYNE, A.R.: Strees Softening in Natural Rubber Vulcanizates. Filler Loaded Rubbers. In: *Journal of Applied Polymer Science* 9 (1965), S. 3011. http://dx.doi.org/10.1002/app.1965.070090907. – DOI 10.1002/app.1965.070090907

[34] HARWOOD, JAC ; MULLINS, L ; PAYNE, AR: Stress softening in natural rubber vulcanizates. Part II. Stress softening effects in pure gum and filler loaded rubbers. In: *Journal of Applied Polymer Science* 9 (1965), Nr. 9, S. 3011–3021

[35] HARWOOD, J.A.C. ; PAYNE, A.R.: Stress softening in natural rubber vulcanizates. Part III. Carbon black-filled vulcanizates. In: *Journal of Applied Polymer Science* 10 (1966), S. 315. http://dx.doi.org/10.1002/app.1966.070100212. – DOI 10.1002/app.1966.070100212. – ISSN 0021–8995

[36] LORENZ, H ; FRITZSCHE, J ; DAS, A ; STÖCKELHUBER, KW ; JURK, R ; HEINRICH, G ; KLÜPPEL, M: Advanced elastomer nano-composites based on CNT-hybrid filler systems. In: *Composites Science and Technology* 69 (2009), Nr. 13, S. 2135–2143

[37] KLÜPPEL, M ; MÖWES, MM ; LANG, A ; PLAGGE, J ; WUNDE, M ; FLECK, F ; KARL, CW: Characterization and Application of Graphene Nanoplatelets in Elastomers. (2016)

[38] In: YUDASAKA, Masako ; IIJIMA, Sumio ; CRESPI, Vincent H.: *Single-Wall Carbon Nanohorns and Nanocones*. Berlin, Heidelberg : Springer Berlin Heidelberg, 2008. – ISBN 978–3–540–72865–8, 605–629

[39] EINSTEIN, Albert: Eine neue bestimmung der moleküldimensionen. In: *Annalen der Physik* 324 (1906), Nr. 2, S. 289–306

[40] SMALLWOOD, Hugh M.: Limiting Law of the Reinforcement of Rubber. In: *Journal of Applied Physics* 15 (1944), Nr. 11, 758-766. http://dx.doi.org/http://dx.doi.org/10.1063/1.1707385. – DOI http://dx.doi.org/10.1063/1.1707385

[41] KLUPPEL, M u. a.: Structure and properties of fractal filler networks in rubber. In: *Kautschuk Gummi Kunststoffe* 50 (1997), Nr. 4, S. 282–291

[42] HEINRICH, G. ; KLÜPPEL, M.: Recent Advances in the Theory of Filler Networking in Elastomers. In: *Advances in Polymer Science* 160 (2002), S. 1. http://dx.doi.org/10.1007/3-540-45362-81. – DOI 10.1007/3–540–45362–81

[43] NIEDERMEIER, W. ; FROEHLICH, J. ; LUGINSLAND, H.D.: Reinforcement mechanism in the rubber matrix by active fillers. In: *Kautschuk Gummi Kunststoffe* 55 (2002), S. 356

[44] KLÜPPEL, Manfred: The role of disorder in filler reinforcement of elastomers on various length scales. In: *Filler-Reinforced Elastomers/Sanning Force Microscopy*. Springer, 2003, S. 1–86

[45] DONNET, JB ; BANSAL, RC ; WANG, MJ: Carbon Black, revised and expanded. In: *Science and Technology, New York* (1993), S. 62–64

[46] SCHRÖDER, A: *Charakterisierung verschiedener Rußtypen durch systematische statische Gasadsorption*, Ph. D. thesis, University of Hannover, Diss., 2000

[47] SCHRÖDER, A ; KLÜPPEL, M ; SCHUSTER, RH ; HEIDBERG, J: Surface energy distribution of carbon black measured by static gas adsorption. In: *Carbon* 40 (2002), Nr. 2, S. 207–210

[48] RUDZINSKI, W. ; EVERETT, D. H.: *Adsorption of Gases on Heterogeneous Surfaces*. Elsevier Science, 1991. – ISBN 9780080984360

[49] BRUNAUER, Stephen ; EMMETT, P. H. ; TELLER, Edward: Adsorption of Gases in Multimolecular Layers. In: *Journal of the American Chemical Society* 60 (1938), Nr. 2, 309-319. http://dx.doi.org/10.1021/ja01269a023. – DOI 10.1021/ja01269a023

[50] PFEIFER, P ; OBERT, M ; COLE, MW: Fractal BET and FHH theories of adsorption:

a comparative study. In: *Proceedings of the Royal Society of London A: Mathematical, Physical and Engineering Sciences* Bd. 423 The Royal Society, 1989, S. 169–188

[51] MANDELBROT, Benoit B.: *Fractals*. Wiley Online Library, 1977

[52] MANDELBROT, Benoit B.: *The fractal geometry of nature*. Bd. 173. Macmillan, 1983

[53] HERD, Charles R. ; MCDONALD, Gerard C. ; SMITH, Randolph E. ; HESS, William M.: The Use of Skeletonization for the Shape Classification of Carbon-Black Aggregates. In: *Rubber Chemistry and Technology* 66 (1993), Nr. 4, 491-509. http://dx.doi.org/10.5254/1.3538323. – DOI 10.5254/1.3538323

[54] In: BUNDE, Armin ; HAVLIN, Shlomo: *Percolation I*. Berlin, Heidelberg : Springer Berlin Heidelberg, 1991. – ISBN 978–3–642–51435–7, 51–96

[55] In: HAVLIN, Shlomo ; BUNDE, Armin: *Percolation II*. Berlin, Heidelberg : Springer Berlin Heidelberg, 1991. – ISBN 978–3–642–51435–7, 97–150

[56] KRAUS, Gerard: Structure–concentration equivalence in carbon black reinforcement of elastomers. III. Application to tensile strength. In: *Journal of Applied Polymer Science* 15 (1971), Nr. 7, S. 1679–1685

[57] LUCH, D ; YEH, GSY: Morphology of strain-induced crystallization of natural rubber. I. Electron microscopy on uncrosslinked thin film. In: *Journal of Applied Physics* 43 (1972), Nr. 11, S. 4326–4338

[58] POOMPRADUB, Sirilux ; TOSAKA, Masatoshi ; KOHJIYA, Shinzo ; IKEDA, Yuko ; TOKI, Shigeyuki ; SICS, Igors ; HSIAO, Benjamin S.: Mechanism of strain-induced crystallization in filled and unfilled natural rubber vulcanizates. In: *Journal of applied physics* 97 (2005), Nr. 10, S. 103529

[59] PLAGGE, J ; KLÜPPEL, M: Determining strain-induced crystallization of natural rubber composites by combined thermography and stress-strain measurements. In: *Polymer Testing* 66 (2018), S. 87–93

[60] KRAUS, Gerard: Reinforcement of Elastomers by Carbon Black. In: *Rubber Chemistry and Technology* 51 (1978), Nr. 2, 297-321. http://dx.doi.org/10.5254/1.3545836. – DOI 10.5254/1.3545836

[61] MAIER, P.G. ; GÖRITZ, D.: Molecular Interpretation on the Payne Effect. In: *Kautschuk Gummi Kunststoffe* 49 (1996), S. 18

[62] LION, A.: A constitutive model for carbon black filled rubber: Experimental investigations and mathematical representation. In: *Continuum Mechanics and Thermodynamics* 8 (1996), S. 153. http://dx.doi.org/10.1007/BF01181853. – DOI 10.1007/BF01181853. – ISSN 0935–1175

[63] BÖHM, Johannes: *Der Payneeffekt: Interpretation und Anwendung in einem neuen Materialgesetz für Elastomere*, Diss., 2001

[64] FRÖHLICH, J. ; NIEDERMEIER, W. ; LUGINSLAND, H.D.: The effect of filler-filler and filler-elastomer interaction on rubber reinforcement. In: *Composites Part A: Applied*

Science and Manufacturing 36 (2005), S. 449. http://dx.doi.org/10.1016/j.compositesa.2004.10.004. – DOI 10.1016/j.compositesa.2004.10.004

[65] HENTSCHKE, Reinhard ; HAGER, Jonathan ; HOJDIS, Nils W.: Molecular modeling approach to the prediction of mechanical properties of silica-reinforced rubbers. In: *Journal of Applied Polymer Science* 131 (2014), Nr. 18, n/a–n/a. http://dx.doi.org/10.1002/app.40806. – DOI 10.1002/app.40806. – ISSN 1097–4628

[66] MULLINS, L: Effect of stretching on the properties of rubber. In: *Rubber Chemistry and Technology* 21 (1948), Nr. 2, S. 281–300

[67] DANNENBERG, EM ; BRENNAN, JJ: Strain energy as a criterion for stress softening in carbon-black-filled vulcanizates. In: *Rubber Chemistry and Technology* 39 (1966), Nr. 3, S. 597–608

[68] DIANI, Julie ; FAYOLLE, Bruno ; GILORMINI, Pierre: A review on the Mullins effect. In: *European Polymer Journal* 45 (2009), Nr. 3, S. 601–612

[69] KLÜPPEL, M. ; HEINRICH, J.: Fractal structures in carbon black reinforced rubbers. In: *Rubber Chemistry and Technology* 68 (1995), S. 623

[70] KLUPPEL, M ; MEIER, J: Modeling of soft matter viscoelasticity for FE-applications. In: *CONSTITUTIVE MODELS FOR RUBBER* 2 (2001), S. 11–20

[71] LUO, Huijun ; KLÜPPEL, Manfred ; SCHNEIDER, Horst: Study of filled SBR elastomers using NMR and mechanical measurements. In: *Macromolecules* 37 (2004), Nr. 21, S. 8000–8009

[72] KLUPPEL, M ; MEIER, J ; DAMGEN, M: Modeling of stress softening and filler induced hysteresis of elastomer materials. In: *CONSTITUTIVE MODELS FOR RUBBER-PROCEEDINGS-* Bd. 4 Balkema, 2005, S. 171

[73] LORENZ, H ; MEIER, J ; KLÜPPEL, M: Micromechanics of internal friction of filler reinforced elastomers. In: *Elastomere Friction*. Springer, 2010, S. 27–52

[74] KREMER, Friedrich ; SCHÖNHALS, Andreas: *Broadband dielectric spectroscopy*. Springer Science & Business Media, 2002

[75] BOESE, Diethelm ; KREMER, Friedrich: Molecular dynamics in bulk cis-polyisoprene as studied by dielectric spectroscopy. In: *Macromolecules* 23 (1990), Nr. 3, S. 829–835

[76] MEIER, Johann G. ; MANI, Joseph W. ; KLÜPPEL, Manfred: Analysis of carbon black networking in elastomers by dielectric spectroscopy. In: *Physical Review B* 75 (2007), Nr. 5, S. 054202

[77] MEIER, Johann G. ; KLÜPPEL, Manfred: Carbon black networking in elastomers monitored by dynamic mechanical and dielectric spectroscopy. In: *Macromolecular materials and engineering* 293 (2008), Nr. 1, S. 12–38

[78] FRITZSCHE, J ; KLÜPPEL, M: Structural dynamics and interfacial properties of filler-reinforced elastomers. In: *Journal of Physics: Condensed Matter* 23 (2010), dec, Nr. 3,

035104. http://dx.doi.org/10.1088/0953-8984/23/3/035104. – DOI 10.1088/0953–8984/23/3/035104

[79] STEINHAUSER, Dagmar ; MÖWES, Markus ; KLÜPPEL, Manfred: Carbon black networking in elastomers monitored by simultaneous rheological and dielectric investigations. In: *Journal of Physics: Condensed Matter* 28 (2016), Nr. 49, S. 495103

[80] KREYENSCHULTE, Hermann ; RICHTER, Sven ; GÖTZE, Thomas ; FISCHER, Dieter ; STEINHAUSER, Dagmar ; KLÜPPEL, Manfred ; HEINRICH, Gert: Interaction of 1-allyl-3-methyl-imidazolium chloride and carbon black and its influence on carbon black filled rubbers. In: *Carbon* 50 (2012), Nr. 10, S. 3649–3658

[81] KUHN, Werner: Beziehungen zwischen Molekülgröße, statistischer Molekülgestalt und elastischen Eigenschaften hochpolymerer Stoffe. In: *Colloid & Polymer Science* 76 (1936), Nr. 3, S. 258–271

[82] JAMES, Hubert M. ; GUTH, Eugene: Theory of the Elastic Properties of Rubber. In: *The Journal of Chemical Physics* 11 (1943), Nr. 10, 455-481. http://dx.doi.org/http://dx.doi.org/10.1063/1.1723785. – DOI http://dx.doi.org/10.1063/1.1723785

[83] JAMES, Hubert M. ; GUTH, Eugene: Theory of the Elasticity of Rubber. In: *Journal of Applied Physics* 15 (1944), Nr. 4, 294-303. http://dx.doi.org/http://dx.doi.org/10.1063/1.1707432. – DOI http://dx.doi.org/10.1063/1.1707432

[84] MOONEY, M.: A Theory of Large Elastic Deformation. In: *Journal of Applied Physics* 11 (1940), Nr. 9, 582-592. http://dx.doi.org/http://dx.doi.org/10.1063/1.1712836. – DOI http://dx.doi.org/10.1063/1.1712836

[85] RIVLIN, R. S.: Torsion of a Rubber Cylinder. In: *Journal of Applied Physics* 18 (1947), Nr. 5, 444-449. http://dx.doi.org/http://dx.doi.org/10.1063/1.1697674. – DOI http://dx.doi.org/10.1063/1.1697674

[86] GENT, A. N.: A New Constitutive Relation for Rubber. In: *Rubber Chemistry and Technology* 69 (1996), Nr. 1, 59-61. http://dx.doi.org/10.5254/1.3538357. – DOI 10.5254/1.3538357

[87] YEOH, O. H.: Some Forms of the Strain Energy Function for Rubber. In: *Rubber Chemistry and Technology* 66 (1993), Nr. 5, 754-771. http://dx.doi.org/10.5254/1.3538343. – DOI 10.5254/1.3538343

[88] MARCKMANN, G. ; VERRON, E.: Comparison of Hyperelastic Models for Rubber-Like Materials. In: *Rubber Chemistry and Technology* 79 (2006), Nr. 5, 835-858. http://dx.doi.org/10.5254/1.3547969. – DOI 10.5254/1.3547969

[89] HEINRICH, G ; STRAUBE, E ; HELMIS, G: Rubber elasticity of polymer networks: theories. In: *Polymer Physics*. Springer, 1988, S. 33–87

[90] RUBINSTEIN, Michael ; PANYUKOV, Sergei: Elasticity of polymer networks. In: *Macromolecules* 35 (2002), Nr. 17, S. 6670–6686

[91] KÄSTNER, S: Theorie der Polymernetzwerke mit behinderter Fluktuation. In: *Colloid and Polymer Science* 259 (1981), Nr. 5, S. 499–507

[92] KLÜPPEL, M: Finite chain extensibility and topological constraints in swollen networks. In: *Macromolecules* 27 (1994), Nr. 24, S. 7179–7184

[93] VILGIS, Thomas A. ; HEINRICH, Gert ; KLÜPPEL, Manfred: *Reinforcement of polymer nano-composites: theory, experiments and applications*. Cambridge University Press, 2009

[94] SVANEBORG, Carsten ; GREST, Gary S. ; EVERAERS, Ralf: Strain-dependent localization, microscopic deformations, and macroscopic normal tensions in model polymer networks. In: *Physical review letters* 93 (2004), Nr. 25, S. 257801

[95] FREUNDLICH, Herbert: *Kapillarchemie: Eine Darstellung der Chemie der Kolloide und verwandter Gebiete*. Akad. Verl.Ges., Leipzig, 1909

[96] LANGMUIR, Irving: The adsorption of gases on plane surfaces of glass, mica and platinum. In: *Journal of the American Chemical society* 40 (1918), Nr. 9, S. 1361–1403

[97] LANGMUIR, Irving: The Vapor Pressure of Metallic Tungsten. In: *Phys. Rev.* 2 (1913), Nov, 329-342. http://dx.doi.org/10.1103/PhysRev.2.329. – DOI 10.1103/PhysRev.2.329

[98] HALL, C.E.: Dark Field Electron Microscopy: II. Studies of colloidal carbon. In: *Journal of Applied Physics* 19 (1948), Nr. 3, S. 271–277. http://dx.doi.org/http://dx.doi.org/10.1063/1.1715057. – DOI http://dx.doi.org/10.1063/1.1715057

[99] DONNET, Jean-Baptiste ; BANSAL, Roop C. ; WANG, Meng-Jiao: *Carbon black: Science and Technology*. Dekker, New York, 1993. – ISBN 082478975X

[100] FOWLER, Ralph H. ; GUGGENHEIM, Edward A.: *Statistical thermodynamics: a version of statistical mechanics for students of physics and chemistry*. University Press, 1952

[101] ADAMSON, AW ; LING, Irene ; DATTA, SK: Advances in Chemistry. In: *Am. Chemical Soc. Publication Xo* 33 (1961), S. 51

[102] ADAMSON, Arthur W. ; LING, Irene ; DORMANT, Leon ; OREM, Michael: Physical adsorption on heterogeneous surfaces. In: *Journal of Colloid and Interface Science* 21 (1966), Nr. 4, S. 445–457

[103] DORMANT, Leon M. ; ADAMSON, Arthur W.: Application of the BET equation to heterogeneous surfaces. In: *Journal of Colloid and Interface Science* 38 (1972), Nr. 1, S. 285–289

[104] SCHRÖDER, Andreas ; KLÜPPEL, Manfred ; SCHUSTER, Robert H.: Characterisation of Surface Activity of Carbon Black and its Relation to Polymer-Filler Interaction. In: *Macromolecular Materials and Engineering* 292 (2007), Nr. 8, S. 885–916

[105] NIEDERMEIER, W ; RAAB, H ; STIERSTORFER, J ; KREITMEIER, Stefan ; GÖRITZ, Dietmar: The microstructure of carbon black investigated by atomic force microscopy. In: *Kautschuk Gummi Kunststoffe* (1994), Nr. 47, S. 799–805

[106] WEI, Xu ; ZERDA, TW ; YANG, H ; GERSPACHER, M: Surface fractal dimension of graphitized carbon black particles. In: *Carbon* 2 (1996), Nr. 34, S. 165–171

[107] RIEKER, Thomas P. ; MISONO, Shinji ; EHRBURGER-DOLLE, Françoise: Small-angle X-ray scattering from carbon blacks: Crossover between the fractal and Porod regimes. In: *Langmuir* 15 (1999), Nr. 4, S. 914–917

[108] SCHRÖDER, A ; KLÜPPEL, M ; SCHUSTER, RH: Oberflächenaktivität von Furnacerussen. 1. Bestimmung der Oberflächenrauheit mittels statischer Gasadsorption, Monolagenbereich. In: *Kautschuk und Gummi, Kunststoffe* 52 (1999), Nr. 12, S. 814–822

[109] PFEIFER, P ; COLE, MW: Fractals in surface science: scattering and thermodynamics of adsorbed films. II. In: *New journal of chemistry* 14 (1990), Nr. 3, S. 221–232

[110] LIDE, DR: *Handbook of Chemistry and Physics CRC Press, Boca Raton Ann Arbor London Tokyo (1995), 75*

[111] OKEL, Timothy A. ; WADDELL, Walter H.: Silica Properties/Rubber Performance Correlation. Carbon Black-Filled Rubber Compounds. In: *Rubber Chemistry and Technology* 67 (1994), Nr. 2, 217-236. http://dx.doi.org/10.5254/1.3557523. – DOI 10.5254/1.3557523

[112] WEITZ, D. A. ; HUANG, J. S. ; LIN, M. Y. ; SUNG, J.: Limits of the Fractal Dimension for Irreversible Kinetic Aggregation of Gold Colloids. In: *Phys. Rev. Lett.* 54 (1985), Apr, 1416–1419. http://dx.doi.org/10.1103/PhysRevLett.54.1416. – DOI 10.1103/PhysRevLett.54.1416

[113] GERSPACHER, M ; O'FARRELL, CP: Advanced carbon black characterization and reinforcement modeling. In: *Kautschuk und Gummi, Kunststoffe* 45 (1992), Nr. 2, S. 97–102

[114] LE MEHAUTE, Alain ; GERSPACHER, Michel ; TRICOT, Claude: Fractal geometry. In: *Carbon Black: Science and Technology* (1993), S. 245

[115] FLEGLER, Stanley L. ; HECKMAN, John W. ; KLOMPARENS, Karen L.: *Elektronenmikroskopie: Grundlagen, Methoden, Anwendungen, Heidelberg, Berlin*. Oxford, 1995

[116] ERNI, Rolf ; ROSSELL, Marta D. ; KISIELOWSKI, Christian ; DAHMEN, Ulrich: Atomic-resolution imaging with a sub-50-pm electron probe. In: *Physical Review Letters* 102 (2009), Nr. 9, S. 096101

[117] MEAKIN, Paul ; DONN, Bertram ; MULHOLLAND, George W.: Collisions between point masses and fractal aggregates. In: *Langmuir* 5 (1989), Nr. 2, 510-518. http://dx.doi.org/10.1021/la00086a038. – DOI 10.1021/la00086a038

[118] ALEMÁN, JV ; CHADWICK, Alan V. ; HE, J ; HESS, M ; HORIE, K ; JONES, Richard G. ; KRATOCHVÍL, P ; MEISEL, I ; MITA, I ; MOAD, G u. a.: Definitions of terms relating to the structure and processing of sols, gels, networks, and inorganic-organic hybrid materials (IUPAC Recommendations 2007). In: *Pure and Applied Chemistry* 79 (2007), Nr. 10, S. 1801–1829

[119] BÖHM, Georg G. ; NGUYEN, My N.: Flocculation of carbon black in filled rubber compounds. I. Flocculation occurring in unvulcanized compounds during annealing at

elevated temperatures. In: *Journal of applied polymer science* 55 (1995), Nr. 7, S. 1041–1050

[120] RUDHARDT, Daniel ; BECHINGER, Clemens ; LEIDERER, Paul: Direct measurement of depletion potentials in mixtures of colloids and nonionic polymers. In: *Physical review letters* 81 (1998), Nr. 6, S. 1330

[121] GÖTZELMANN, B ; EVANS, R ; DIETRICH, S: Depletion forces in fluids. In: *Physical Review E* 57 (1998), Nr. 6, S. 6785

[122] ASAKURA, Sho ; OOSAWA, Fumio: Interaction between particles suspended in solutions of macromolecules. In: *Journal of polymer science* 33 (1958), Nr. 126, S. 183–192

[123] KAUFMAN, Stanley ; SLICHTER, WP ; DAVIS, DD: Nuclear magnetic resonance study of rubber–carbon black interactions. In: *Journal of Polymer Science Part A-2: Polymer Physics* 9 (1971), Nr. 5, S. 829–839

[124] STOCKELHUBER, KW ; SVISTKOV, AS ; PELEVIN, AG ; HEINRICH, G: Impact of filler surface modification on large scale mechanics of styrene butadiene/silica rubber composites. In: *Macromolecules* 44 (2011), Nr. 11, S. 4366–4381

[125] HOFMANN, M. ; HERRMANN, A. ; OK, S. ; FRANZ, C. ; KRUK, D. ; SAALWÄCHTER, K. ; STEINHART, M. ; RÖSSLER, E. A.: Polymer Dynamics of Polybutadiene in Nanoscopic Confinement As Revealed by Field Cycling 1H NMR. In: *Macromolecules* 44 (2011), Nr. 11, 4017-4021. http://dx.doi.org/10.1021/ma2002504. – DOI 10.1021/ma2002504

[126] HUBER, Gregor: *Universelle Eigenschaften gefüllter Elastomere*, Diss., 1997

[127] HUBER, Gregor ; VILGIS, Thomas A.: On the mechanism of hydrodynamic reinforcement in elastic composites. In: *Macromolecules* 35 (2002), Nr. 24, S. 9204–9210

[128] LAKE, GJ ; THOMAS, AG: The strength of highly elastic materials. In: *Proceedings of the Royal Society of London A: Mathematical, Physical and Engineering Sciences* Bd. 300 The Royal Society, 1967, S. 108–119

[129] PONNAMMA, Deepalekshmi ; SADASIVUNI, Kishor K. ; STRANKOWSKI, Michael ; GUO, Qipeng ; THOMAS, Sabu: Synergistic effect of multi walled carbon nanotubes and reduced graphene oxides in natural rubber for sensing application. In: *Soft Matter* 9 (2013), Nr. 43, S. 10343–10353

[130] HARISHKUMAR, Chougule ; GIESE, Ulrich ; SCHUSTER, Robert: Multifunctional and specific interactions of CNTs in NBR and HNBR. In: *World Journal of Engineering* 11 (2014), Nr. 1, S. 29–36

[131] MÖWES, Markus M. ; FLECK, Frank ; KLÜPPEL, Manfred: EFFECT OF FILLER SURFACE ACTIVITY AND MORPHOLOGY ON MECHANICAL AND DIELECTRIC PROPERTIES OF NBR/GRAPHENE NANOCOMPOSITES. In: *Rubber Chemistry and Technology* 87 (2014), Nr. 1, S. 70–85

[132] KUMAR, Vineet ; HANEL, Thomas ; FLECK, Frank ; MOEWES, Markus ; DILMAN, Tatiana ; GIESE, Ulrich ; KLUEPPEL, Manfred: Graphene filled Nitrile Butadiene Rubber

Nanocomposites. In: *KGK-KAUTSCHUK GUMMI KUNSTSTOFFE* 68 (2015), Nr. 6, S. 69–79

[133] In: KLÜPPEL, M. ; MÖWES, M. M. ; LANG, A. ; PLAGGE, J. ; WUNDE, M. ; FLECK, F. ; KARL, C. W.: *Characterization and Application of Graphene Nanoplatelets in Elastomers*. Cham : Springer International Publishing, 2017. – ISBN 978–3–319–47696–4, 319–360

[134] MONDAL, Titash ; BHOWMICK, Anil K. ; GHOSAL, Ranjan ; MUKHOPADHYAY, Rabindra: Graphene-Based Elastomer Nanocomposites: Functionalization Techniques, Morphology, and Physical Properties. (2016)

[135] FLECK, F. ; FROLTSOV, V. ; KLÜPPEL, M.: Polymer-Filler Interphase Dynamics and Reinforcement of Elastomer Nanocomposites. In: *Soft Materials* 12 (2014), nov, Nr. sup1, S121–S134. http://dx.doi.org/10.1080/1539445x.2014.957836. – DOI 10.1080/1539445x.2014.957836

[136] FLECK, F ; MOEWES, MM ; KLUEPPEL, M: Influence of Ionic Liquid on the Polymer-Filler Coupling of Carbon Black filled Elastomers. In: *KGK-KAUTSCHUK GUMMI KUNSTSTOFFE* 69 (2016), Nr. 4, S. 49–52

[137] SHORE, Albert F. ; SHORE, Charles P.: *Apparatus for measuring the hardness of materials*. Juli 8 1930. – US Patent 1,770,045

[138] BROWN, Roger: *Handbook of polymer testing: physical methods*. CRC press, 1999

[139] ZERDA, TW ; XU, W ; ZERDA, A ; ZHAO, Y ; VON DREELE, RB: High pressure Raman and neutron scattering study on structure of carbon black particles. In: *Carbon* 38 (2000), Nr. 3, S. 355–361

[140] ROSS, Sydney ; OLIVIER, James P.: *On physical adsorption*. Halsted Press, 1964

[141] LIPPENS, BC ; LINSEN, BG ; DE BOER, JH: Studies on pore systems in catalysts I. The adsorption of nitrogen; apparatus and calculation. In: *Journal of Catalysis* 3 (1964), Nr. 1, S. 32–37

[142] KASUYA, Daisuke ; YUDASAKA, Masako ; TAKAHASHI, Kunimitsu ; KOKAI, Fumio ; IIJIMA, Sumio: Selective Production of Single-Wall Carbon Nanohorn Aggregates and Their Formation Mechanism. In: *The Journal of Physical Chemistry B* 106 (2002), Nr. 19, 4947-4951. http://dx.doi.org/10.1021/jp020387n. – DOI 10.1021/jp020387n

[143] SYED, Imran H. ; STRATMANN, Patrick ; HEMPEL, Günter ; KLÜPPEL, Manfred ; SAALWÄCHTER, Kay: Entanglements, Defects, and Inhomogeneities in Nitrile Butadiene Rubbers: Macroscopic versus Microscopic Properties. In: *Macromolecules* 49 (2016), Nr. 23, 9004-9016. http://dx.doi.org/10.1021/acs.macromol.6b01802. – DOI 10.1021/acs.macromol.6b01802

[144] MARK, James E. ; MARK, James E. (Hrsg.): *Physical Properties of Polymers Handbook*. Springer, New York, NY, 2007 https://www.ebook.de/

de/product/5399386/james_e_mark_physical_properties_of_polymers_handbook.html. – ISBN 978–0–387–31235–4